AERODYNAMIC DESIGN AND PERFORMANCE ANALYSES OF GRID FIN
IN SUPERSONIC FLOW USING DESIGN OF EXPERIMENTS AND
COMPUTATIONAL FLUID DYNAMICS

A THESIS SUBMITTED TO
THE GRADUATE SCHOOL OF NATURAL AND APPLIED SCIENCES
OF
MIDDLE EAST TECHNICAL UNIVERSITY

BY

ERDEM DİNÇER

IN PARTIAL FULFILLMENT OF THE REQUIREMENTS
FOR
THE DEGREE OF MASTER OF SCIENCE
IN
AEROSPACE ENGINEERING

FEBRUARY 2022

Approval of the thesis:

AERODYNAMIC DESIGN AND PERFORMANCE ANALYSES OF GRID FIN IN SUPERSONIC FLOW USING DESIGN OF EXPERIMENTS AND COMPUTATIONAL FLUID DYNAMICS

submitted by **ERDEM DİNÇER** in partial fulfillment of the requirements for the degree of **Master of Science** in **Aerospace Engineering, Middle East Technical University** by,

Prof. Dr. Halil Kalıpçılar
Dean, Graduate School of **Natural and Applied Sciences**   _____

Prof. Dr. Serkan Özgen
Head of the Department, **Aerospace Engineering**   _____

Assoc. Prof. Dr. Nilay Sezer Uzol
Supervisor, **Aerospace Engineering, METU**   _____

Examining Committee Members:

Prof. Dr. Yusuf Özyörük
Aerospace Engineering Department, METU   _____

Assoc. Prof. Dr. Nilay Sezer Uzol
Aerospace Engineering Department, METU   _____

Prof. Dr. Dilek Funda Kurtuluş
Aerospace Engineering Department, METU   _____

Asst. Prof. Dr. Özge Başkan Perçin
Aerospace Engineering Department, METU   _____

Assoc. Prof. Dr. Munir Elfarra
Aerospace Engineering Department, Ankara Yıldırım Beyazıt University   _____

Date: 11.02.2022

I hereby declare that all information in this document has been obtained and presented in accordance with academic rules and ethical conduct. I also declare that, as required by these rules and conduct, I have fully cited and referenced all material and results that are not original to this work.

Name Last name : Erdem Dinçer

Signature :

ABSTRACT

AERODYNAMIC DESIGN AND PERFORMANCE ANALYSES OF GRID FIN IN SUPERSONIC FLOW USING DESIGN OF EXPERIMENTS AND COMPUTATIONAL FLUID DYNAMICS

Dinçer, Erdem
Master of Science, Aerospace Engineering
Supervisor: Assoc. Prof. Dr. Nilay Sezer Uzol

February 2022, 111 pages

Control surfaces are key components of missile aerodynamic performance that can create the necessary forces and moments to make maneuvers. Grid fins are unconventional control surfaces used for aerodynamic control of missiles. In this thesis, parametric design of grid fin is performed in terms of aerodynamic performance using Design of Experiments and Computational Fluid Dynamics. The 3-D, steady-state, compressible, viscous flow CFD simulations are performed for the complex grid fin geometries in supersonic conditions, using polyhedral unstructured grids. Design of Experiments method is used to reduce the number of computationally expensive and time-consuming CFD analyses. First, a validation study is performed for the CFD simulations using MICOM grid fin test case. Then, the aerodynamic performances of different grid fin designs are investigated using design parameters as chord, span, width, gap between members, web thickness, and frame thickness. Grid fin geometries are investigated at Mach number of 2.5 for different angles of attack between 0° and 15° and for roll angles of 0° and 45° at sea level standard atmospheric conditions. In parameter screening results, it is shown

that the normal force, side force, and roll moment coefficients do not affected by the frame and web thickness parameters. Response surfaces are validated and can be used for optimization studies of grid fin. High chord-to-gap ratio decreases the aerodynamic performance which is caused by the separation in higher angles of attack values. Also, the change in the roll angle influences the flow behavior which affects the aerodynamic performance of grid fins.

Keywords: Grid Fin, Computational Fluid Dynamics, Design of Experiment, Response Surface, Missile Aerodynamics

ÖZ

DENEY TASARIMI VE HESAPLAMALI AKIŞKANLAR DİNAMİĞİ KULLANILARAK SÜPERSONİK AKIŞTA IZGARA KANATÇIK AERODİNAMİK TASARIMI VE PERFORMANS ANALİZLERİ

Dinçer, Erdem
Yüksek Lisans, Havacılık ve Uzay Mühendisliği
Tez Yöneticisi: Assoc. Prof. Dr. Nilay Sezer Uzol

Şubat 2022, 111 sayfa

Kontrol yüzeyleri, manevra yapabilmek için gerekli kuvvet ve moment yaratabilen füze aerodinamik performansının temel bileşenleridir. Izgara kanatçıklar, füzelerin aerodinamik kontrolü için kullanılan geleneksel olmayan kontrol yüzeyleridir. Bu tezde, ızgara kanatçıklarının parametrik tasarımı, Deney Tasarımı ve Hesaplamalı Akışkanlar Dinamiği kullanılarak aerodinamik performans açısından incelenmiştir. 3-boyutlu, daimi, sıkıştırılabilir, viskoz akış HAD simülasyonları, karmaşık geometrisi olan ızgara kanatçıkları için ses-üstü koşullarda, çokyüzlü yapısal olmayan ağlar kullanılarak yapılmıştır. Hesaplama açısından pahalı ve zaman alıcı HAD analizleri sayısını azaltmak için Deney Tasarımı yöntemi kullanılmıştır. İlk olarak, mevcut MICOM ızgara kanatçık test durumu ile HAD doğrulama çalışmaları yapılmıştır. Daha sonra, veter, kanat açıklığı, kanat genişliği, elemanlar arasındaki boşluk, iç ağ elemanlarının kalınlığı ve çerçeve kalınlığı gibi tasarım parametreleri kullanılarak farklı ızgara kanatçık tasarımlarının aerodinamik performansı incelenmiştir. Izgara kanatçık geometrileri, 2,5 Mach sayısında deniz seviyesinde standart atmosfer koşullarında 0° ile 15° arasındaki farklı hücum açıları ve 0° ve 45° yuvarlanma açıları için incelenmiştir. Parametre tarama sonuçlarında, normal kuvvet, yanal kuvvet, yalpalama momenti katsayılarının çerçeve ve iç ağ

elemanlarının kalınlığı parametrelerinden etkilenmediği gösterilmiştir. Yanıt yüzeyleri doğrulanmıştır ve ızgara kanatçıklarının en iyileme çalışmaları için kullanılabilir. Yüksek veter-elemanlar arası boşluk oranı aerodinamik performansı düşürmektedir bu durum yüksek hücum açılarında akış ayrılmasından kaynaklanmaktadır. Ayrıca, yuvarlanma açısındaki değişiklik ızgara kanatların aerodinamik performansını etkileyen akış davranışını da değiştirmektedir.

Anahtar Kelimeler: Izgara Kanatçık, Hesaplamalı Akışkanlar Dinamiği, Deney Tasarımı, Tepki Yüzeyi, Füze Aerodinamiği

To my family

ACKNOWLEDGMENTS

TABLE OF CONTENTS

LIST OF TABLES

LIST OF FIGURES

FIGURES

LIST OF ABBREVIATIONS

ABBREVIATIONS

ARF	Aeroballistics Research Facility
BB	Box-Behnken
BC	Boundary Condition
BoI	Body of Influence
CCD	Central Composite Design
CFD	Computational Fluid Dynamics
CFL	Courant-Friedrichs-Lewy
CoV	Coefficient of Variance
CV	Cross-Validation
DERA	Defence Evaluation and Research Agency
DLR	German Aerospace Center
DNS	Direct Numerical Simulation
DOE	Design of Experiments
DREV	Defence Research Establishment Valcartier
FAS	Full Approximation Storage
FMG	Full Multi Grid
LES	Large Eddy Simulation
LHS	Latin Hypercube Sampling
LU-SGS	Lower-Upper Symmetric Gaus-Seidel
NRMSE	Normalized Root Mean Square Error
PRESS	Predicted Residual Sum of Squares
PSE	Lenth Pseudo Standard Error
RANS	Reynolds-Averaged Navier-Stokes
RBF	Radial Basis Function
RMSE	Root Mean Square Error
RSM	Response Surface Methododgy
SOU	Second Order Upwind
SST	Shear Stress Transport
TCAAM	Tail Controlled Air-to-Air Missile

LIST OF SYMBOLS

SYMBOLS

e	Energy
E	Total Energy
ε	Turbulent Dissipation Rate
f	Body Force
k	Turbulent Kinetic Energy
I	Unit Tensor
$\vec{n}$	Normal of the Surface
p	Pressure
$\dot{q}$	Heat Transfer Rate
ρ	Density
R	Universal Gas Constant
μ	Dynamic Viscosity
μ_0	Reference Dynamic Viscosity
T	Static Temperature
T_0	Reference Temperature
τ_{ij}	Stress Tensor
ω	Specific Dissipation Rate
Ω	Small Portion of the Control Volume
u	Velocity Component in x-direction
v	Velocity Component in y-direction
w	Velocity Component in z-direction
$y+$	Dimensionless Wall Distance
∇	Gradient Operator
φ	Solution Variable
$\vec{r}$	Displacement Vector
l_{ref}	Reference Length
S_{ref}	Reference Area
$h(x)$	Radial Basis Function
w_i	Linear Combination Coefficients
α	Angle of Attack
ϕ	Roll Angle
C_A	Axial Force Coefficient
C_N	Normal Force Coefficient
C_Y	Side Force Coefficient
C_l	Roll Moment Coefficient
C_m	Pitch Moment Coefficient
C_n	Yaw Moment Coefficient
C_{HM}	Hinge Moment Coefficient
C_{BM}	Bending Moment Coefficient

CHAPTER 1

INTRODUCTION

Designing any aerial vehicle requires several design iterations to achieve a design solution which meets the requirements. In each iteration, the vehicle is resized to improve performance. From missile aerodynamics point of view, control surfaces are vital components in missile design process. These devices can be deflected back and forth to generate forces and moments to make the missile pitch, yaw and roll maneuvers and eventually change the attitude of the missile.

In this thesis, a design study for a grid fin control surface using response surface methodology is performed. The methodology applied in this thesis includes the investigation of grid fin parameters and their effects on aerodynamic performance. Although some parameters are expected to have no influence in the grid fin design, complex aerodynamic flow field makes the interference effects between parameters significant. Due to the nature of this multi-parameter design problem, a design of experiment (DOE) approach is used into the design methodology.

1.1   Background

There are several types of control surfaces which are classified by their placement (canard, wing, tail) (See Figure 1.1), packaging arrangement (folded, wraparound, switchblade), deflection (all movable, flap control) and orientation (interdigitated, inline) (See Figure 1.2) [1]. Grid fin is classified as unconventional and all movable control surface. Grid fin, also known as lattice fin, consists of small intersecting planar surfaces supported by an outer frame. Unlike conventional fins, grid fins are mounted perpendicular to the flow and the incoming air passes through the grid fin.
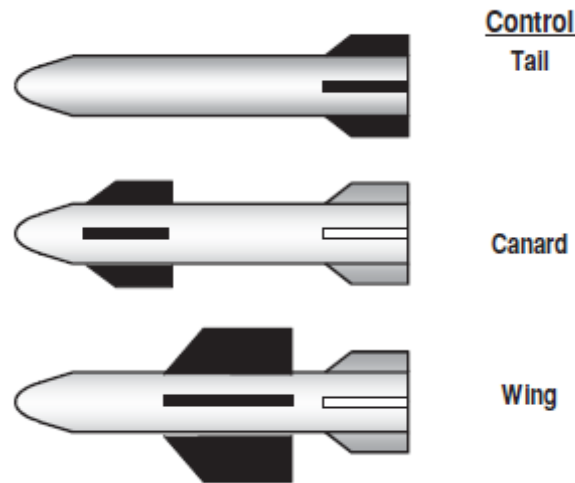
Figure 1.1. Aerodynamic Control Alternatives Classified by Placement [1]
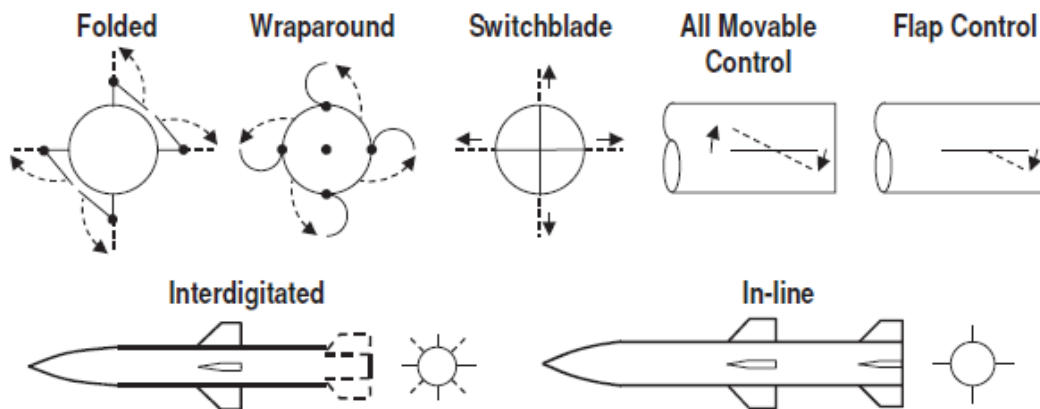
Figure 1.2. Classification of Aerodynamic Control Surfaces [1]

In the 1950s, research and development studies on grid fins are first started by Sergey Belotserkovsky and his team. Since then, these control devices have been a part of missile industry and an intensive research topic all over the world. At the beginning, grid fins were used as air brake system by Soviets in Soyuz launch escape spacecraft. The most known applications where grid fins used as control devices are USA-based "Massive Ordinance Air Blast (MOAB)" bomb (See Figure 1.3) and Russian-made "Vympel R-77" air-to-air missile (See Figure 1.4). Recently, grid fins have been started to be used on Space-X Falcon 9 reusable launch vehicle (See Figure 1.5) as maneuvering surfaces at final reentry stage [2].

Figure 1.3. Massive Ordinance Air Blast (MOAB) [3]

Figure 1.4. R-77 (AA-12 Adder as NATO Reporting Name) Air-to-Air Missile [4]

Figure 1.5. SpaceX Falcon9 Reusable Launch Vehicle Equipped with Grid Fins [5]

In high-speed agile missiles, such as air to air missiles, the control surfaces are exposed to enormous forces and moments within its flight envelope, which creates a challenge in structural design of aerodynamic control surfaces. Therefore, lower hinge moment production is always favorable while designing such missiles. Moreover, to design a highly maneuverable missile, aerodynamic control surfaces must work effectively in its flight regime. Also, due to the requirement of carriage constraints, control surfaces should be packed efficiently. Luckily, grid fin is a good choice for all these design requirements. Due to much smaller chord length compared to the regular fins, variation in the center of pressure becomes smaller, hence, grid fins produce very small hinge moments. Additionally, grid fins have superior lifting and stall characteristics which increases the control capability of a missile. Grid fins can endure high aerodynamics forces acting on itself because the grid like internal structure provides remarkably high strength-to-weight ratio. Finally, grid fins can be folded over the missile body and efficiently packaged. The main drawbacks of grid fins are high drag force and complex flow field [6]. Because of different flight conditions with different control settings, complexity in the flow behavior becomes inevitable. Even in high supersonic speeds where grid fins are the most favorable, oblique shocks reflected from the grid fins disturb the flow in the downstream. The detailed information about grid fin aerodynamics is explained in the following section. Another disadvantage is complexity of the grid fin geometry. Compared to conventional planar fins, grid fins have more shape parameters which makes it hard to design, optimize, and produce such devices.

1.2   Grid Fin Aerodynamics

Grid fin aerodynamics is difficult to understand and very complex. The behavior of grid fin highly depends on the flow conditions. In transonic speeds, the flow chocking phenomenon occurs and grid fin acts as a single blunt body forming a detached bow shock in front of itself. In this case, grid fin does not allow most of the incoming air to pass through and a huge performance loss encountered. This

phenomenon may occur in low supersonic flows depending on the effective angle of attack of the flow encountering the grid fin. It can be observed that the interferences with missile body, fairings and even the outer frame may also cause the partial or full chocking. In low subsonic flows, shocks generated at the leading edges of the grid fin reflect and interact with each other inside the grid cells. Oblique shocks disrupt downstream flow in the high supersonic region. These flow regimes are illustrated in Figure 1.6. The flow in the downstream a decaying shock diamond pattern is created by grid fins. The abrupt changes caused by reflected shock waves in the downstream make the investigation of grid fins challenging. As an example, the shock diamonds emanating from an exhaust of a Pratt & Whitney J58 jet engine is shown in Figure 1.7. The shock structure can be adjusted using different profiles in the web cross section profile or changing the chord or the gap between the web members. The phenomena in grid fin aerodynamics are not limited to shock wave interactions. Especially in transonic or low supersonic flows, boundary layer is also changing the flow behavior. The shocks generated and reflected inside the grid cells highly interact with the boundary layer that propagates on the grid fin surfaces.
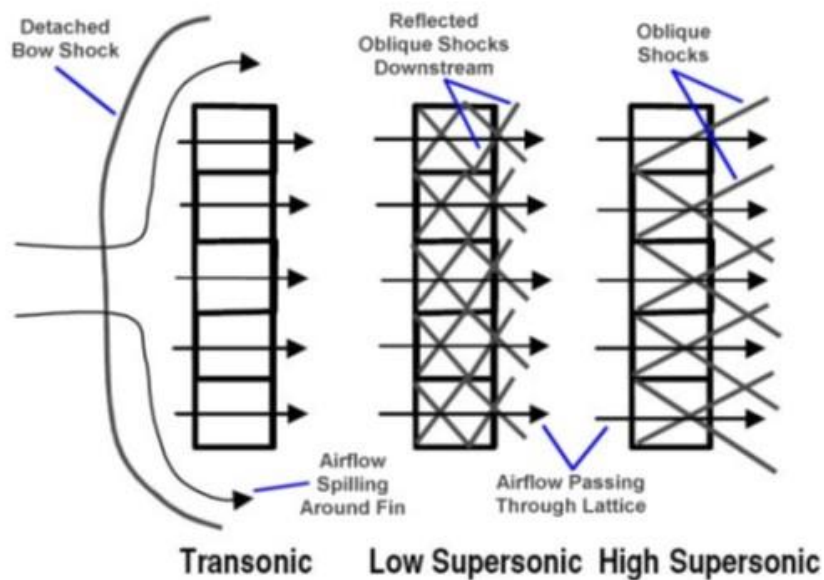
Figure 1.6. Behavior of Grid Fin in Different Flow Regimes
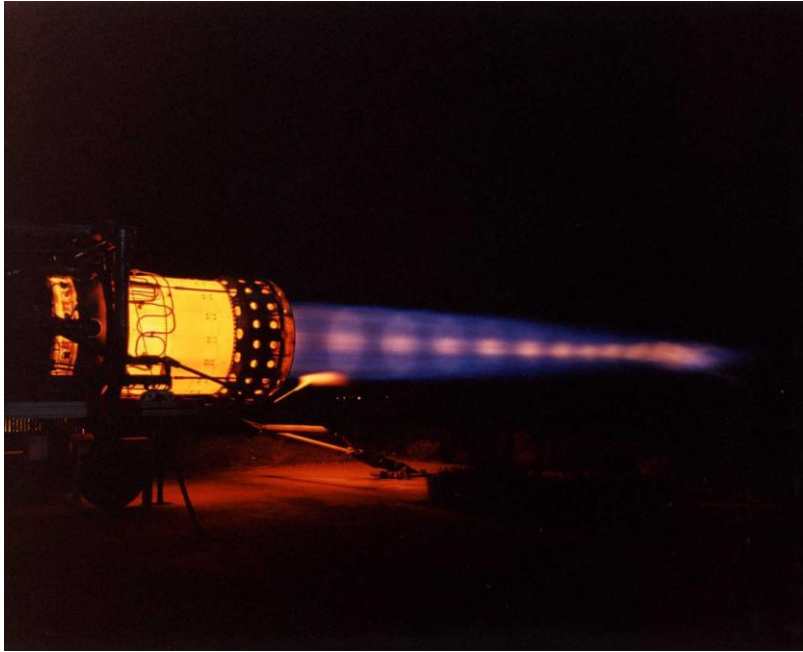
Figure 1.7. Shock Diamonds at the Exhaust of a Pratt & Whitney J58 Jet Engine

In 2013, Ravindra et al. [28] analyzed 2D and 3D grid fin configurations and investigated flow field characteristics of grid fin. In 2D part of the study, 7 different Mach numbers ranging from transonic speeds to supersonic speeds were analyzed and 5 distinct flow regimes were identified. According to this study, the flow field characteristics can be summarized as follows:

1.2.1 Single Plate Regime

In single plate regime, different plates are undisturbed by the presence of other plates, and the waves generated by individual plates are unaffected by the waves generated by other plates. Waves on individual plates include a shock on the windward side, a corresponding expansion on the leeward side, a detached bow shock due to the plate's bluntness, which usually coalesces with the windward shock, a recompression shock at the trailing edge on the leeward side, and a corresponding expansion on the windward side. It's critical to note that these waves interact with one another, as well as the shear layer that emerges from the plates' trailing edges downstream.

1.2.2 Periodic Plate Regime

In the periodic plate regime, the flow regime of the intermediate plates (excluding the top and bottom plates) corresponds to that of periodic plates. In the case of plates of zero thickness, the expansion fan emanating from the leading edge of any given plate contacts with the bottom surface of the plate immediately above it.

1.2.3 Separated Flow Regime

When the incidence is increased further, the end of the periodic flow regime is recognized by the sudden development of a separation bubble occupying the whole upper surface of the bottom most plate, which does not receive a pressure relaxation at the trailing edge due to a pending expansion wave (unlike other plates). With this occurrence, the separated flow regime develops. Within a few degrees of increase in incidence, this bubble grows, covering the upper surface of all the plates above with a massive separation bubble. An apparent stall in the lift curve indicates this. Surprisingly, a drop in drag follows, showing that wave drag is being minimized.

Inviscid and viscous cases are compared by Ravindra et al. to further understand this phenomenon,. As previously indicated, the flow encounters a complex non-linear wave interaction close to the trailing edge of the plates in order to achieve the required pressure adjustment. In the inviscid case, oblique shock wave interactions are insufficient for conducting the required pressure adjustment at the trailing edge around the incidence indicating the start of the separated flow regime, resulting in a lambda shock in the flow. This reveals itself as a shock-induced separation in viscous flows, resulting in a separated flow regime. In transient solutions, a lambda shock occurs whereas the steady solution corresponds to a separated flow. Another essential and intriguing property of the separated flow regime is that when the incidence is increased more, some of the stalled plates un-stall. On both the lift and drag curves, this manifests as a bucket.

1.2.4   Cusped Shock Regime

Cusped shocks arise ahead of the leading edge of the plates as the incidence is increased beyond the separated flow regime. The region of substantial activity is confined to the upper surface of the individual plates until this regime begins. This is relocated to the plates' bottom surface, where a typical shock advancing towards the leading edge eventually leads to the creation of the cusped shock.

1.2.5   Single Body Regime

As the incidence rises, the flow becomes dominated by a single bow shock, as if the entire series of plates were a single body. Only at lower Mach numbers, this regime is important.

1.3   Literature Survey

Research and development studies have been conducted since grid fins were first introduced. While reviewing the literature, the studies are categorized in terms of objectives of studies, flow regimes and methods used. This approach makes the review process easier. There are also exceptional studies found in the literature which cannot be dropped into any defined categories. These studies are also covered in this section. In literature review process for CFD studies, a systematic review paper written by Sharma and Kumar [7] is a very informative and helpful source. From aerodynamics perspective, grid fin related studies are classified as follows:

- Comparison with planar fins

- Prediction methods

- CFD validation and flow field Investigation

- Investigation of grid fin shape parameters

In order to show the advantages and disadvantages of grid fins, grid fins are compared with conventional planar fins. These studies are valuable to introduce grid fin concept and reveal the properties of grid fins in different flow regimes. In 1993, Washington and Miller performed an experimental study with "Micom Grid Fin" at Mach numbers ranging from 0.5 to 3.5 covering subsonic to supersonic flow regimes and angle of attack values ranging between -15 to +15 degrees. This study showed that grid fin creates very small hinge moments, similar root bending moments and normal forces, 3 to 4 times higher drag values compared to planar fin. It is also stated that grid fin stall did not occur for fin angles of attack up to 30 degrees [8]. In 2001, Fournier conducted wind tunnel experiments with Tail Controlled Air-to-Air Missile (TCAAM) model. Similarly, this study was performed at Mach numbers ranging from 0.5 to 3.0 and angles of attack up to 15 degrees. This study showed that grid fin configurations increase axial force, reduce normal force and static stability. The experimental results presented in this study are also validated with actual free flight data [9]. These two experimental studies have been widely used test cases for CFD validation purposes. Later, DeSpirito et al. compared grid fin and planar fin tail configurations for a canard-controlled missile in supersonic region using viscous CFD calculations. This study showed that grid tail fins improved the roll effectiveness of the canards at low supersonic speed. Grid fins reduced the uneven pressure distribution produced by the interaction with canard trailing vortices on itself resulting in lower roll moment production [10]. In 2010, Munavar performed a comparison study using viscous CFD calculations and results indicated similar conclusions made by Washington [11].

In the literature, there are several studies focusing on predicting aerodynamic forces and moments produced by the grid fin using theoretical methodologies. These prediction methods are designed based on flow regimes. Although these methods have centered around mostly vortex lattice formulation in subsonic flow, the studies divided into two as shock expansion theory and doublet modelling in supersonic flow to predict aerodynamic forces. Burkhalter is the pioneer in predictive methods for grid fin aerodynamics. Burkhalter and Frank proved that the vortex lattice theory has

been proven to be adequate for the basic linear range of load and moment coefficient predictions in subsonic flows. Also, they included carryover loads as well as the upwash effects from the body in this study [12]. Later the study was extended to nonlinear aerodynamic prediction by Burkhalter et al. [13]. In 1996, Burkhalter introduced a prediction method used for grid fins at supersonic flows using a modified version of Evvard's theory [14]. Whereas shock-expansion theory is only valid for the two-dimensional flows, Evvard's theory is applicable to three-dimensional thin wings in supersonic flow [15]. In 2005 Theerthamalai et al. established a shock-expansion based method to predict axial and normal forces and pitching moments at subsonic flows and validated with available experimental data [16]. Later, this study was extended to bring out the effect of roll orientation on normal force, pitching moment and induced out-of-plane force [6]. In 2007, Theerthamalai compared experimental data and results predicted with vortex lattice theory and validated this method in subsonic flow as well[17]. In this study, an approach similar to the one used in the study performed by Burkhalter and Frank was adopted. In 2015, Ledlow et al. combined the vortex lattice theory for subsonic flows, empirical relations for transonic flow and the shock expansion theory for supersonic flow aiming to integrate the grid fin aerodynamics to a missile system preliminary design code [18]. In this work, the goal was to maximize the target strike area of a missile using both planar fins and grid fins. With this perspective, this study can also be considered as a comparison with planar fins. It was found that when grid fins used for aerodynamic control surfaces, the missile is able to strike a larger target area with a higher degree of accuracy compared to equivalent planar fins. Also, it is worth to mention an extraordinary prediction method for transonic flows established by Dikbaş in 2015 in his master thesis [19], different than the methods explained herein previously. The method is named as "Unit Grid Fin" since it is based on CFD solutions of cut out pieces of grid fins in the web and frame intersection regions. With this method, grid fin aerodynamic forces and moments can be predicted easily. However, since this method only solve the grid fin regions, an interference correction

should be applied. Later in 2018, this method was validated for all Mach regimes from subsonic to supersonic [20].

Computational fluid dynamics is a powerful tool to understand flow physics. However, since grid fins are a new concept, CFD should be validated to decide whether it is applicable to grid fins or not. Since most of these studies included a flow field investigation, both these topics are reviewed in a combined fashion. In 1998, first reported CFD calculations on grid fins were performed by Sun and Khalid under the Defence Research Establishment Valcartier (DREV), Canada [21]. In this study, both viscous and inviscid solutions were obtained. The authors drew a conclusion that both viscous and inviscid CFD calculations can be used while studying the attached supersonic flows around missiles with grid fins. Also, the comparisons between planar fins and grid fins were made and flow-field investigations were compared with pitot pressure contours. In 2000, DeSpirito et al. validated grid fin viscous CFD calculations with wind tunnel data provided by The Defence Evaluation and Research Agency (DERA) at Mach number of 2.5 [22]. Pressure, turbulent viscosity, and Mach number contours were shown at angle of attack of 10° and 20° in this study. In 2001, DeSpirito and Sahu [23] compared viscous CFD results at Mach numbers of 2.0 and 3.0 with experimental data provided by DREV. Pressure contours were also presented at angle of attack of 10°. In 2005, Mingshen et al. [24] showed that in subsonic and supersonic region Lower-Upper Symmetric Gauss-Seidel (LU-SGS) algorithm, which is an improved version of the Gauss-Seidel algorithm, along with multiblock structure grid can solve full Navier-Stokes equations on "Micom Grid Fin" and validated this algorithm for grid fin flows. One year later, this study was extended by changing from multiblock structure grid to hybrid structure-unstructured grids [25]. In 2006, from German Aerospace Center (DLR) Reynier et al. introduced "Actuator Disk", which is a remarkable approach in CFD analysis of grid fins. In this approach, the lattice wings were replaced by an actuator disk. Therefore, by using artificial boundary conditions on actuator disk boundaries, the grid fins were taken into account. In this study, grid fin aerodynamics were calculated using semi-empirical methods and missile body were

analyzed with DLR Tau unstructured solver. The computational time dropped by about 85 percent when actuator disk approach was applied. The results of this study validated actuator disk approach and actuator disk concept can be used for design and analysis of supersonic missiles with grid fins [26]. Next year, Hughson et al. [27] validated Loci/CHEM flow solver from transonic to supersonic Mach regimes using experimental data acquired by Aeroballistics Research Facility (ARF). This study also includes heavy flow field investigations of a missile with grid fins. Moreover, flow field shadowgraph comparisons were presented. At subsonic flow, a bow shock system was detected at the exit of the grid fin cells, at transonic flows, a standoff shock formed in front of grid fin. Above Mach number of 2.0, the grid fin cells obtained the form of a supersonic nozzle having a sonic Mach disk inside. In 2013, Ravindra et al. [28] analyzed 2D and 3D grid fin configurations and investigated flow field characteristics of grid fin. 3D analyses were included comparison with conventional planar fins. This remarkable study is investigated in detail at the previous section.

Since this thesis is relevant to the last topic, studies investigated the grid fin shape parameters will be explained here in detail. The studies mentioned here will be used to determine which parameters to be taken into consideration in the scope of this thesis.

In 1993, Washington et al. performed experimental studies to investigate the effects of grid fin curvature and sweep in folding direction on aerodynamic performance of a grid fin [29]. This study covers Mach numbers and angles of attack ranging between 0.5 to 3.5 and -10 to 20 degrees, respectively. Up to 75 degrees the grid fins were folded in both backward and forward directions to investigate the effect of folding the grid fins on the missile body. The curved grid fin geometry and the sweep angle in folding direction are illustrated in Figure 1.8 and Figure 1.9. It is found that the effect of curvature of grid fin on fin performance is small. This implies that grid fins can be utilized in terms of efficient packaging without loss of performance. The study also showed that the fin drag values are as higher as 5 times of zero folding sweep angle case and maximum fin drag occurred at 45 degrees back/forward folding

sweep angle. It can be inferred that grid fins can be used as effective drag brake devices. When grid fins were folded in both directions, normal force production decreases down to 30 to 50 percent.
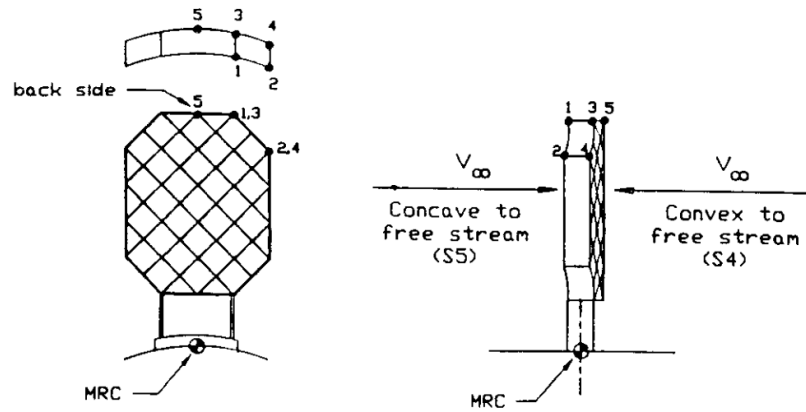
Figure 1.8. Definition of Grid Fin Curvature [29]
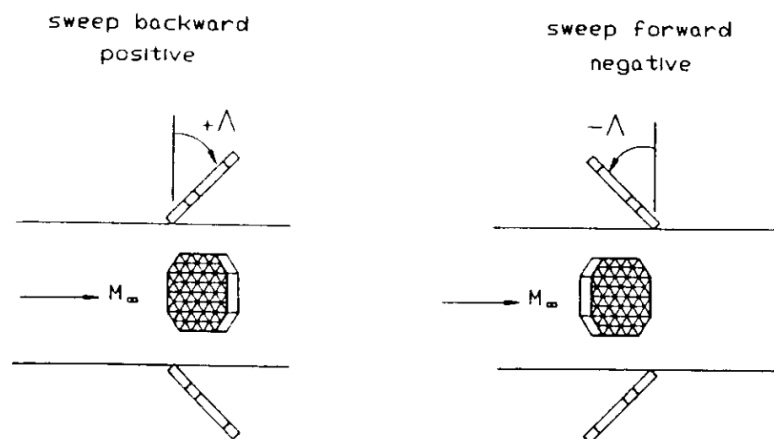
Figure 1.9. Definition of Grid Fin Folding Angle [29]

Miller and Washington [30] conducted a series of experiments to reduce drag forces of "Micom Grid Fin" in 1994. In total, six different grid fin configurations were tested to investigate web thickness and outer frame cross-section shape. The frame cross-sections are shown in Figure 1.10 along with the grid fin dimensions. This study includes Mach numbers ranging between 0.5 to 2.5 and angle of attack up to 20 degrees and fin deflections of 0, 10 and 20 degrees. The results of this study revealed that at subsonic Mach numbers frame shape changes normal force

characteristics, whereas, at supersonic Mach numbers web thickness has the greatest effect on normal force characteristics. Root bending moment and chordwise center of pressure location remained unaffected with variations in these parameters. Frame cross-section shape and web thickness highly affects drag characteristics; thus, these parameters were found as critical design parameters.

FIN #	A1	A2	A3	A4	B1	B2	B3	B4	C	D
F1	.060 TO .040	.040	.030	.020	.384	.384	.384	.384	90.0	.008
F2	.060 TO .040	.040	.030	.020	.266 TO .309	.309	.330	.352	25.0	.008
F3	.060 TO .040	.040	.030	.020	.024 TO .155	.155	.220	.286	17.0	.008
F4	.060 TO .040	.040	.030	.020	.005	.005	.005	.005	VARIES	.008
F5	.060 TO .040	.040	.030	.020	.266 TO .309	.309	.330	.352	25.0	.012
F6	.060 TO .025	.025	.019	.013	.266 TO .341	.341	.354	.367	25.0	.008

ALL DIMENSIONS IN INCHES
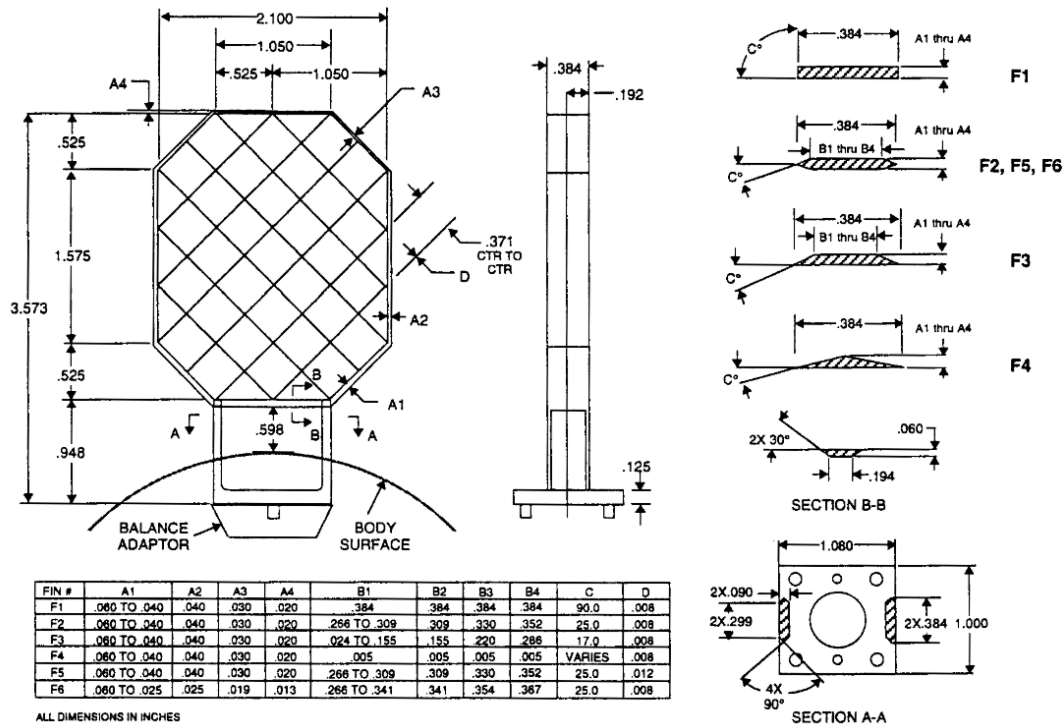
Figure 1.10. MICOM Grid Fin Dimensions and Six Different Outer Frame Cross-Section Shapes and Dimensions [30]

Another study [31], based on 3-D Euler calculations, addressed the issue of the grid fin size, in terms of both the panel thickness and frontal shape in supersonic flows. Thr frontal shape is the ramp fairing installed upstream of the grid fin base where it is attached to a missile body. It is found that the fairing installed at the base of the grid fin can reduce the blockage and other interferences resulting in some improvement in aerodynamic performance of the grid fin. This study showed that increasing the grid fin panel thickness changes shock structure at the leading edge and results in a degradation in aerodynamic performance.

14

Hiroshima and Tatsumi [32] showed that the effect of grid patterns on aerodynamic performance is small as long as having the same grid cell area and web thickness in subsonic and supersonic flow with an experimental study in 1994. Test conditions include angles of attack from -5 to 30 degrees, fin deflection of 0 and 10 degrees and roll angle from 0 to 180 degrees with 15 degrees intervals. The tested grid patterns were square, triangle and hexagonal and shown in Figure 1.11.
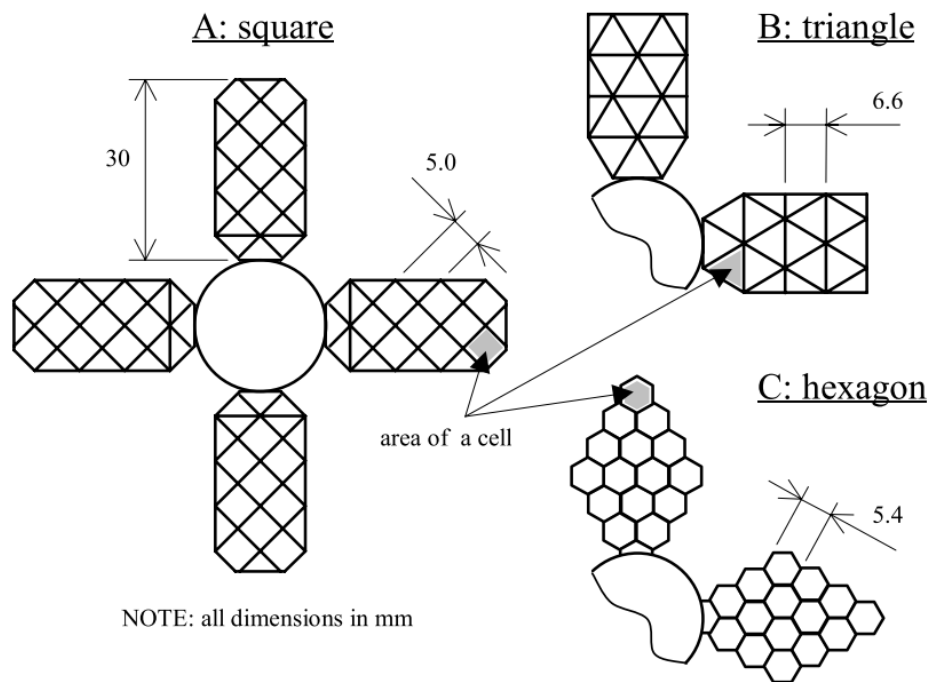
Figure 1.11. Grid Fin Configurations Having Different Cell Patterns [32]

In 2005, Wu et al. [33] investigated the effect of frame and web thicknesses as well as their shapes using Euler calculations at Mach number of 2.5. The results showed that grid fin frame shape and thickness have the greatest effect on aerodynamic performance, especially on the drag force.

In the grid fin design process, the number of parameters is tremendous and new concepts emerged from imagination, there is almost no limit. To reduce the drag force of grid fins, locally swept grid fins were tried by Schülein and Guyot [34]. The study includes both numerical simulations and wind tunnel measurements at Mach numbers from 2 to 6 and angles of attacks varied from 0 to 10 degrees for unswept

and locally swept grid fins and planar fins. Grid fin configurations and web member intersection types which are used in this study are shown in Figure 1.12 and Figure 1.13. Results showed that using locally swept lattice wings increse zero-lift drag up to 38 percent and lift-to-drag ratio up to 20 percent when compared with conventional grid fins. The lowest zero-lift wave drag produced by the peak-type locally swept grid fins whereas valley-type locally swept lattice wings had better lift-to-drag performance. It is also found that the effect of locally swept edges increases with Mach number, sweep angle, thickness and bluntness of web leading edges, and decreases with the incidence angle and bigger tooth-sizes.
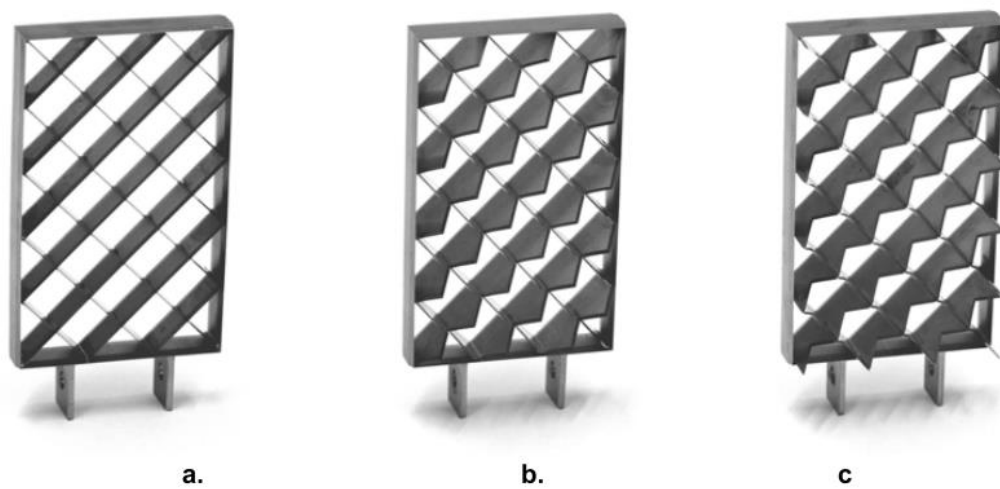
Figure 1.12. Grid Fin Configurations of Unswept (a), Locally Swept (b,c) [34]
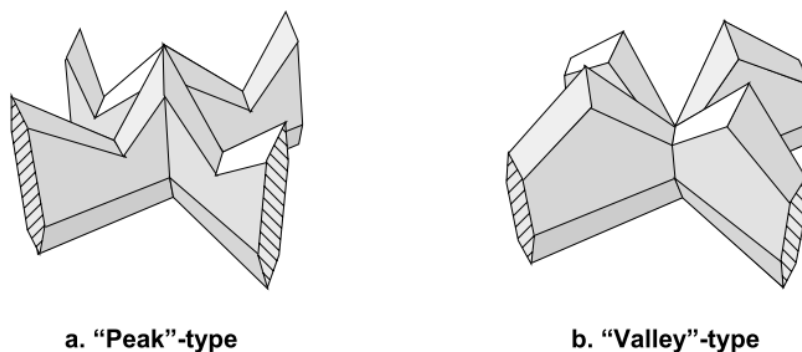
Figure 1.13. Intersection Types Between Locally Swept Web Members [34]

Another grid fin shape parameter, that has been very popular in the last decade, is sweep angle in grid fin configurations. It is used mostly for drag reduction of grid fin configurations. The sweep angle investigated here is not locally swept as previously described but a global sweep angle has been employed as it can be seen in Figure 1.14. In 2009, Zeng et al. [35] investigated swept back grid fins in transonic and supersonic flow regimes and 12 percent drag reduction was achieved using 3-D viscous CFD calculations of grid fin configurations without a missile body. Later that study was extended using a sharp leading edge in swept-back grid fins and 30 percent drag reduction was accomplished [36]. In these studies, swept-back grid fins appeared to be able to reduce flow chocking at transonic and supersonic speeds. In 2012, these studies were followed by another studies [37],[38] including ogive-cylindrical body supporting grid fins, non-zero angle of attack values and experimental measurements. The results indicated that using swept-back sharp leading edge grid fins is remained beneficial at non-zero angle of attack values. In 2018, Faza et al. [39] investigated the sweep angle effects, including both forward and back sweep, at Mach number of 1.5 and up to 15 degrees angle of attack using 3-D viscous CFD calculations without a missile body. It is found that the drag, lift and pitching moment coefficients highly rely on both angles of attack and sweep angle. Since configurations had different sweep angles, these configurations reached its highest aerodynamic efficiency at different angles of attack values.

<div align="center">(a)   (b)</div>
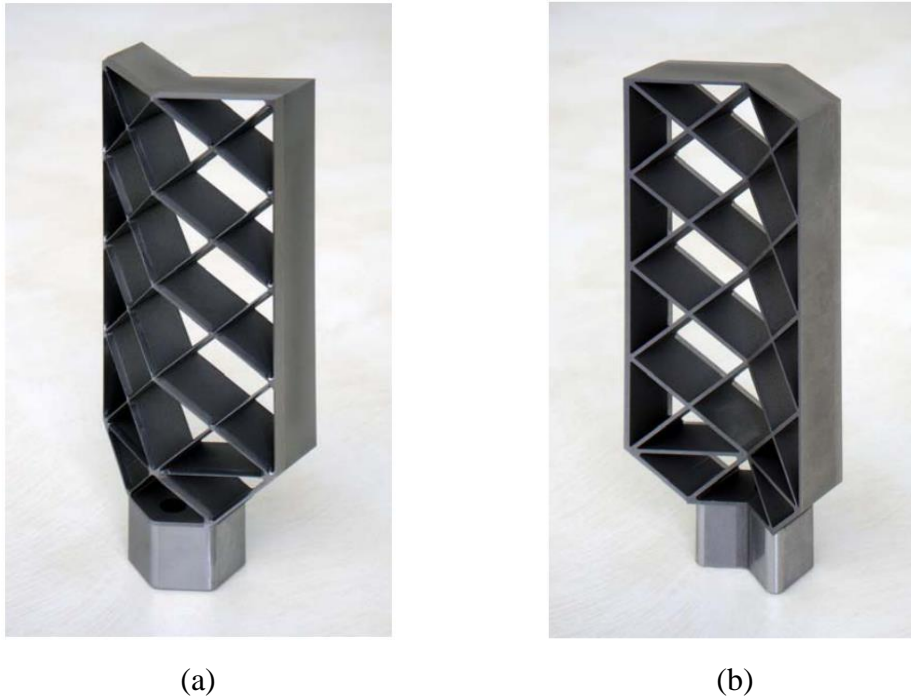
Figure 1.14. Swept-back (a) and swept-forward (b) grid fin configurations [36]

There are also remarkable studies which do not fall into any categories mentioned previously. Yang and Zhang [40] optimized grid fin web and frame shape and thickness together with the missile body where grid fins attached using a method called support vector regression. Another extraordinary study was performed by Despeyroux et al. which is focusing on static and dynamic performances of a grid fin-controlled missile using CFD [41]. In this study, the aerodynamic performance of the grid fin was compared with planar fin at transonic and supersonic flows. The study showed that in supersonic flow, similar behavior in pitch-damping derivative was observed for both the grid fin and the planar fin, however, in transonic flow grid fins provide a lower damping in pitch plane due to blockage effect. In 2018, Peng et al. [42] performed an optimization study on grid fins by changing chord, gap between web members, distance between the grid fin and the missile body surface and number of cells. Optimization was based on sequential approximation. When optimized grid fin shape was used, 2.07 percent lighter take off mass and 14.3 percent heavier payload mass capability achieved compared to the baseline configuration.

1.4   Aim of the Thesis

In this thesis study, grid fin aerodynamic performance in supersonic flow is investigated. The motivation of the study arises from the numerous parameters of the grid fins that still need to be investigated closely. This study aims to contribute to the existing literature by performing a parametric design, investigating flow behavior in supersonic flow and establishing a design methodology for grid fin using Design of Experiments and Response Surface Methodology coupled with Computational Fluid Dynamic analyses.

1.5   Outline of the Thesis

This thesis consists of 5 chapters. In chapter 1, the grid fin is introduced regarding aerodynamic performance. Historical background and missile aerodynamic design background of grid fins are provided. Literature review related to thesis topic is presented. Grid fin aerodynamics is explained in this chapter.

In chapter 2, CFD methodology applied in this thesis is explained. The governing equations, solver algorithms and meshing procedures applied for CFD analyses are presented. The CFD method is validated, and results are discussed in this chapter. Mesh convergence and turbulence model studies are presented in this chapter as well.

In chapter 3, the design methodology which is carried out for this thesis is presented. This chapter includes the grid fin geometry parametrization, parameter selection, DOE details, and the run matrix for CFD analyses.

In chapter 4, firstly, parameter screening results are presented, and the effects of grid fin parameters on aerodynamic coefficients are discussed. Later, response surfaces are generation and validation are presented. Lastly, flow field investigations are performed for the designs with aerodynamic performance degradation.

Finally in chapter 5, concluding remarks regarding the conducted studies and recommendations for future works are presented.

CHAPTER 2

CFD METHODOLOGY

Computational Fluid Dynamics (CFD) is a powerful and widely accepted tool to understand aerodynamics and flow physics. In this section, CFD methodology applied through this thesis is explained.

There are different types of numerical simulations. In turbulent flows, to achieve exact solution, in other words performing Direct Numerical Simulation (DNS), all relevant length scales should be resolved. However, even with modern, fast, and advanced computers, it requires a lot of time and computational source, therefore cost. Even Large Eddy Simulation (LES), in which only large eddies are solved and small eddies are modeled, is not suitable for industrial applications for now. Therefore, Reynolds-Averaged Navier-Stokes (RANS) equations are used in CFD solvers since it offers computationally less expensive solutions compared to LES and DNS. In this method, the solution variables are decomposed into time-averaged values and fluctuations around the mean value which creates additional turbulent stresses and heat flux quantities. Since these quantities are considered new unknowns, these turbulence related terms are tried to be solved by certain turbulence equations and models [43]. In this thesis, RANS method is used and the details of turbulence models are explained in Section 2.2.

2.1   Governing Equations

The governing equations in fluid dynamics are Navier-Stokes equations which are based on conservation of flow quantities which are mass, momentum, and energy [54]. These equations are listed below:

- Conservation of Mass:

$$\frac{\partial \rho}{\partial t} + \nabla \cdot \left(\rho \vec{V}\right) = 0 \tag{2.1}$$

- Conservation of Momentum:

$$\frac{\partial (\rho u)}{\partial t} + \nabla \cdot \left(\rho u \vec{V}\right) = -\frac{\partial p}{\partial x} + \frac{\partial \tau_{xx}}{\partial x} + \frac{\partial \tau_{yx}}{\partial y} + \frac{\partial \tau_{zx}}{\partial z} + \rho f_x \tag{2.2}$$

$$\frac{\partial (\rho v)}{\partial t} + \nabla \cdot \left(\rho v \vec{V}\right) = -\frac{\partial p}{\partial y} + \frac{\partial \tau_{xy}}{\partial x} + \frac{\partial \tau_{yy}}{\partial y} + \frac{\partial \tau_{zy}}{\partial z} + \rho f_y \tag{2.3}$$

$$\frac{\partial (\rho w)}{\partial t} + \nabla \cdot \left(\rho w \vec{V}\right) = -\frac{\partial p}{\partial z} + \frac{\partial \tau_{xz}}{\partial x} + \frac{\partial \tau_{yz}}{\partial y} + \frac{\partial \tau_{zz}}{\partial z} + \rho f_z \tag{2.4}$$

In equations given above, f is an external body force and τ_{ij} is the stress tensor. The stress tensor, τ_{ij}, is defined as follows:

$$\tau_{xx} = -\frac{2}{3}\mu \left(\frac{\partial u}{\partial x} + \frac{\partial v}{\partial y} + \frac{\partial w}{\partial z}\right) + 2\mu \frac{\partial u}{\partial x} \tag{2.5}$$

$$\tau_{yy} = -\frac{2}{3}\mu \left(\frac{\partial u}{\partial x} + \frac{\partial v}{\partial y} + \frac{\partial w}{\partial z}\right) + 2\mu \frac{\partial v}{\partial y} \tag{2.6}$$

$$\tau_{zz} = -\frac{2}{3}\mu \left(\frac{\partial u}{\partial x} + \frac{\partial v}{\partial y} + \frac{\partial w}{\partial z}\right) + 2\mu \frac{\partial w}{\partial z} \tag{2.7}$$

$$\tau_{xy} = \tau_{yx} = \mu \left(\frac{\partial u}{\partial y} + \frac{\partial v}{\partial x}\right) \tag{2.8}$$

$$\tau_{xz} = \tau_{zx} = \mu \left(\frac{\partial u}{\partial z} + \frac{\partial w}{\partial x}\right) \tag{2.9}$$

$$\tau_{yz} = \tau_{zy} = \mu \left(\frac{\partial v}{\partial z} + \frac{\partial w}{\partial y}\right) \tag{2.10}$$

In the stress tensor equations, μ is representing the molecular viscosity. When determining the viscosity of the fluid in the stress tensor, Sutherland's law is used in which the approximation depends only on temperature.

$$\mu = \mu_0 \left(\frac{T}{T_0}\right)^{3/2} \frac{T_0 + S}{T + S} \tag{2.11}$$

Where, μ_0 is $1.716x10^{-6}$, T_0 is $273.15\ K$ and S is $110.4\ K$.

- Conservation of Energy:

$$\frac{\partial}{\partial t}[\rho E] + \nabla \cdot [\rho E \vec{V}]$$

$$= \rho\dot{q} - \left[\frac{\partial}{\partial x}\left(k\frac{\partial T}{\partial x}\right) + \frac{\partial}{\partial y}\left(k\frac{\partial T}{\partial y}\right) + \frac{\partial}{\partial z}\left(k\frac{\partial T}{\partial z}\right)\right]$$

$$- \left[\frac{\partial(up)}{\partial x} + \frac{\partial(vp)}{\partial y} + \frac{\partial(wp)}{\partial z}\right]$$

$$+ \left[\frac{\partial(u\tau_{xx})}{\partial x} + \frac{\partial(u\tau_{yx})}{\partial y} + \frac{\partial(u\tau_{zx})}{\partial z} + \frac{\partial(v\tau_{xy})}{\partial x}\right.$$

$$+ \frac{\partial(v\tau_{yy})}{\partial y} + \frac{\partial(v\tau_{zy})}{\partial z} + \frac{\partial(w\tau_{xz})}{\partial x} + \frac{\partial(w\tau_{yz})}{\partial y}$$

$$\left. + \frac{\partial(w\tau_{zz})}{\partial z}\right] + \rho\vec{f} \cdot \vec{V} \tag{2.12}$$

where, $\dot{q}$ is the heat transfer rate and E is the total energy which is:

$$E = e + \frac{V^2}{2} \tag{2.13}$$

Until now, 5 equations for conservation laws are shown, since conservation of momentum is directional and this equation is written for three components. However, the system of solution has six conservative variables, hence, inclusion of the perfect gas assumption is required to match the number of unknowns with the number of equations. Thus, the equation of state is also used which is given in Equation (2.14).

$$p = \rho RT \tag{2.14}$$

2.2   CFD Analysis Overview

In this thesis steady-state density-based RANS solutions are used along with Roe flux-difference splitting scheme, 2nd order upwind discretization and a properly selected turbulence model. These methods and algorithms are explained in this chapter.

2.2.1   CFD Solver Details

The density based flow solver solves the governing equations in a coupled fashion simultaneously. Non-linear equations are solved iteratively until reaching a converged solution. The steps in this solution method are illustrated in Figure 2.1. The solver checks convergence levels with pre-defined frequency. If not converged, solver updates the primitive variables in next iteration and continue solving governing equations repeatatively until a specified convergence level or maximum number of iteration is achieved.
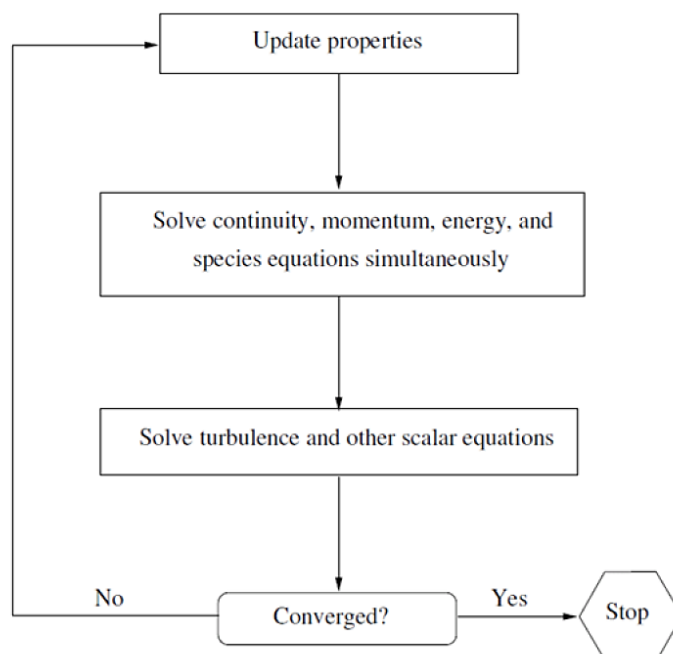
Figure 2.1. Density based solver algorithm [44]

2.2.2   Initialization Approach

For complex flow problems, flow convergence can be accelerated using a better initialization approach. To utilize the initialization process Full Multigrid (FMG) initialization approach is used in the thesis. In this approach, the initial solution is restricted all the way down to the coarsest level and Full Approximation Storage (FAS) is then applied until a given order of residual reduction is achieved or the maximum number of cycles is reached. This process will repeat until the finest level is reached. ANSYS Fluent's approach to forming the multigrid grid hierarchy for FAS is simply to coalesce groups of cells on the finer grid to form coarser grid cells. Coarse grid cells are created by agglomerating the cells surrounding a node, as shown in Figure 2.2. Through the FMG process, the Euler equations for inviscid flow are solved using first order discretization [44]. The FMG initialization process is illustrated in Figure 2.3.

Figure 2.2. Node Agglomeration to Form Coarse Grid Cells in FAS Algorithm [44]

Figure 2.3. Full Multigrid (FMG) Initialization Approach [44]

2.2.3   Spatial Discretization

In spatial discretization, second-order upwind scheme is applied. In this approach, quantities at cell faces are evaluated using multidimensional linear reconstruction. Hence, the face value is computed using the following expression:

$$\varphi_{f,SOU} = \varphi + \nabla\varphi \cdot \vec{r} \tag{2.15}$$

In this expression, φ is the cell-centered value, ∇φ is its gradient in the upstream cell and $\vec{r}$ is the displacement vector from the upstream cell centroid to the face centroid. In CFD analyses performed for this thesis, for gradient evaluations, Green-Gauss Node-Based method is applied. Basically, the arithmetic average of nodal values on the face is computed using the following expression where N_f is the number of nodes on the face:

$$\overline{\varphi}_f = \frac{1}{N_f}\sum_{n}^{N_f} \overline{\varphi}_n \tag{2.16}$$

2.2.4   Convective Fluxes

In the CFD analyses, Roe flux-difference splitting scheme is applied. By splitting flux vector in parts, upwind differencing the split fluxes in a manner consistent with corresponding eigenvalues, the fluxes computed on the left and right sides of the faces. A matrix dissipation term is then added to provide pressure-velocity coupling required for stability.

2.2.5   Turbulence Modelling

The need for turbulence models was explained earlier. In order to predict turbulent flows using RANS equations, apparent turbulent stress and heat flux quantities must be properly approximated. There are three most commonly used turbulence models exist in the literature. The details about these models are explained herein.

2.2.5.1   Spalart-Allmaras Turbulence Model

The Spalart-Allmaras model is a one equation model that was designed specifically for aerospace applications involving wall-bounded flows. The model is not reliable for general industrial flows. This model solves a modeled transport equation for the turbulent viscosity. In its original form, this model is effectively a low Reynolds number model, and it is sensitive for viscous boundary layer mesh. Even though Ansys Fluent has extended the Spalart-Allmaras model with a y+ insensitive wall treatment, it is noted that boundary layer should be resolved at least 10-15 cells.

2.2.5.2   Realizable k-ε Turbulence Model

The standard k-ε model is based on model transport equations for the turbulence kinetic energy (k) and its dissipation rate (ε). In this model, the flow is assumed fully turbulent, and effects of molecular viscosity is negligible. It differs from the standard k- ε model in two ways:

- •   Turbulent viscosity is formulated differently in the realizable k-ε model.

- •   The dissipation rate, ε, has been derived for the transport of the mean-square vorticity fluctuation.

2.2.5.3   SST k-ω Turbulence Model

The standard k-ω model is an empirical model based on model transport equations for the turbulence kinetic energy (k) and the specific dissipation rate (ω). The model has been modified over the years. Shear-Stress Transport (SST) model includes the following refinements to the standard k-ω turbulence model:

- The standard k- ω and the transformed k- ε model are both added together by a blending function which dictates this model to use the standard k-ω model in the near wall region and transformed k-ε model away from the surface.

- Different constants are used in this model.

- Transport of the turbulence shear stress is taken into consideration in the definition of the turbulent viscosity.

These refinements make the SST k-ω model more reliable and accurate for wide class of flows such as adverse pressure gradient flows, airfoils, and transonic shock waves.

2.3   Mesh Generation Overview

In any CFD analysis, solution domain must be divided into cells and faces to solve the fluid domain. Since meshing process directly affects the solution, cell elements should be generated fine enough to reduce the numerical errors. There are different types of mesh structures where each has both advantages and disadvantages. Through the thesis, polyhedral cell elements are used computational grid is prepared for CFD analysis. For grid fin simulations, the number of cell elements which is required to achieve a good mesh resolution is very high due to complex geometry of grid fins. Polyhedral mesh can be used to reduce the number of mesh elements and therefore the computational time without loss of accuracy [45].

In this thesis, Fluent Meshing package of ANSYS software is used for generating unstructured grids. Besides the certain drawbacks such as stair-stepping in the boundary layer zone, this package is capable of creating different types of mesh elements. It is flexible enough to allow the user to adjust scoped sizing of edges or faces. Additionally, the "body of influence" is supported in the software when smaller cells are needed in a predefined region.

The turbulence modeling approach driven y+ number is used to establish the first layer height, ensuring that the flow is resolved in the viscous sublayer imposed by the Law of the Wall [44]. In the CFD analysis performed in this thesis, 20 layers are applied to cover the total boundary layer thickness. The size functions for grid fin surfaces and volume meshes used in the validation case, which is presented in the following section, applied to all other cases.

2.4 CFD Validation Studies – MICOM Grid Fin Test Case

2.4.1 Model Details and Test Conditions

A validation test case study was carried out for MICOM Grid Fin model [30]. The model is a 52-inch-long, 5-inch diameter body-of-revolution with a 3.0 caliber tangent ogive nose faired into a 7.4 caliber afterbody. Four fins are mounted 2.0 caliber forward of the base. MICOM grid fin geometry is given in Figure 2.4. MICOM grid fin placement is shown in Figure 2.5(a). Fins are numbered starting from the top in the clockwise direction. All data presented in this section were obtained from fin numbered as 4. The sign convention for the experimental study is given in Figure 2.5(b).
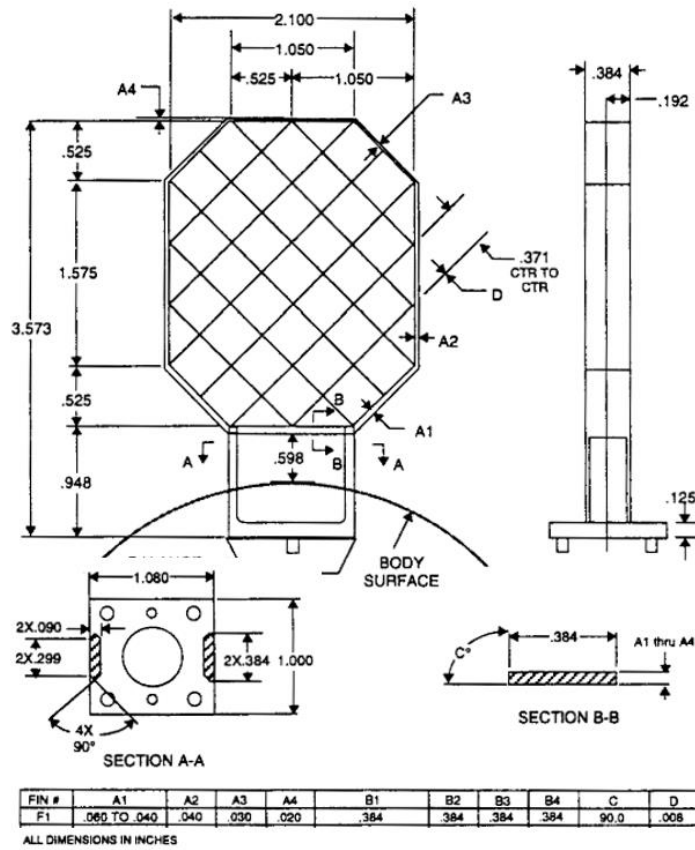
Figure 2.4. MICOM Grid Fin Dimensions [30]

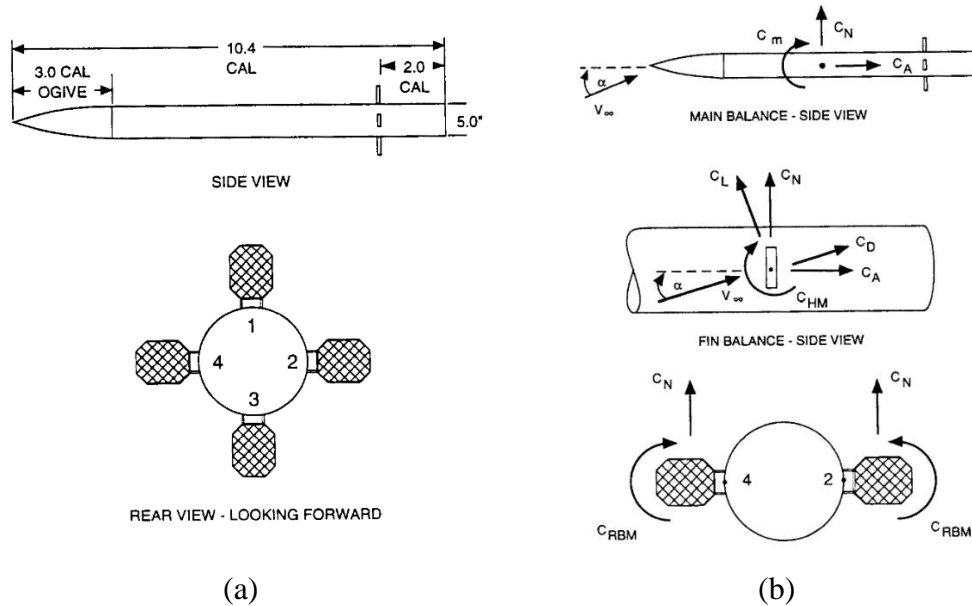(a)   (b)

Figure 2.5. MICOM Wind Tunnel Model Dimensions and Grid Fin Placement

Order (a) and Sign Convergence for Aerodynamic Coefficients (b) [30]

The experiments of MICOM grid fin were performed at the National Testing Service's (NTS) 4 x 4 foot Transonic/Supersonic Wind Tunnel located in Saugus, California. The test facility is a blowdown-to-atmosphere intermittent wind tunnel with a Mach number range of 0.2 to 5.0. In the pitch plane, data was collected at angles of attack ranging from -8 to +20 degrees. Deflection angles for the fins were set to 0, 10, or 20 degrees. The roll angles were set to 0 or 45 degrees. However, only the data collected for the pitch plane is presented in this study, hence, the deflection angle and roll angle are zero for the results shown in this section. Table 2.1 shows the tunnel operating conditions for each test Mach number.

Table 2.1 NTS 4 x 4 foot Transonic/Supersonic Wind Tunnel Operating Conditions

Mach Number	Dynamic Pressure (psf)	Static Pressure (psi)	Total Pressure (psi)	Static Temp. (deg. R)	Re/L x10^{-6} (per ft)
0.5	524	21.8	25.6	502	5.35
0.7	739	15.3	21.0	479	5.66
0.8	802	12.7	19.2	469	5.53
0.9	936	11.6	19.5	451	6.01
1.2	1295	9.0	21.7	415	6.93
1.8	1439	4.3	25.4	316	7.36
2.5	**1400**	**2.2**	**38.0**	**232**	**8.05**

2.4.2   CFD Analysis Details and Boundary Conditions

In the validation study, three-dimensional, steady-state, compressible viscous CFD calculations were performed using the commercial CFD software, ANSYS Fluent version 21R1. In these calculations, RANS equations are solved with k-ε realizable two equation turbulence model along with 2nd-order upwind spatial discretization scheme and Roe flux difference splitting scheme. The simulations were run with a maximum Courant-Friedrich-Lewy (CFL) number of 7 for this validation case.

Simulations were last about 6000 iterations. The residual history of a validation CFD analysis is shown in Figure 2.6. In the CFD validation analyses, maximum residual level of 10^{-3} has been reached.
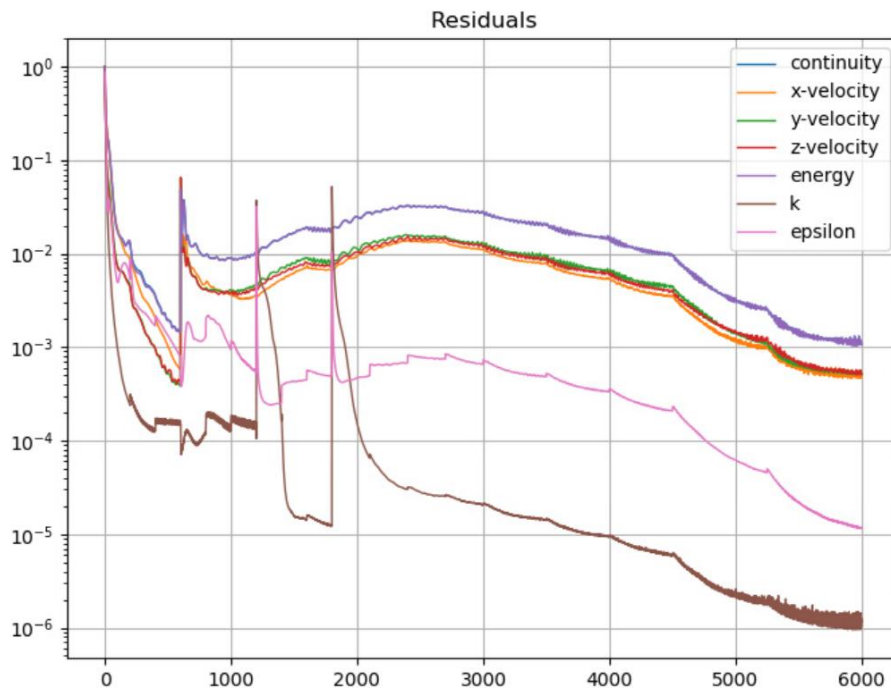
Figure 2.6. Residual History of a Validation CFD Analysis

The CAD model of MICOM grid fin experimental model is created using ANSYS SpaceClaim Design Modeler package. It is presented in Figure 2.7. It is surrounded by a cylindrical enclosure to represent far-field boundary and fluid domain. Dimensions of the enclosure are given in Figure 2.8. The flight conditions are shown at Table 2.2. These conditions are assigned to the enclosure faces to imitate the far-field boundary. No-slip wall boundary condition is applied to the solid surfaces of MICOM grid fin geometry.
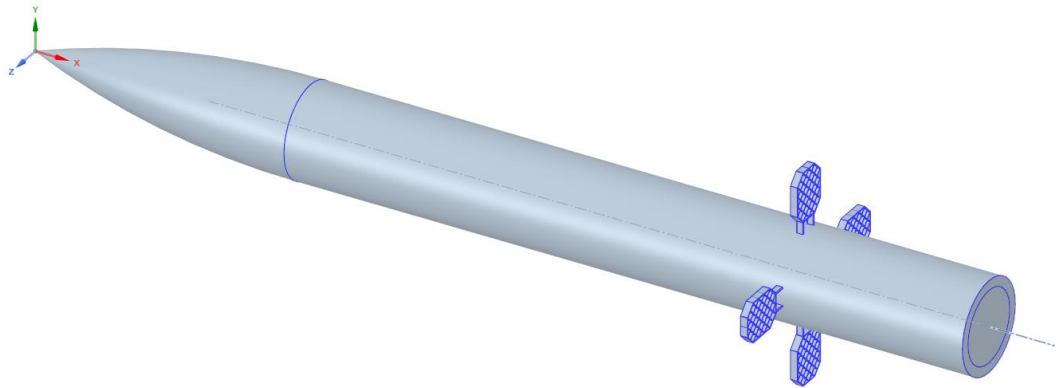
Figure 2.7. MICOM CAD Model

| (a) | (b) |
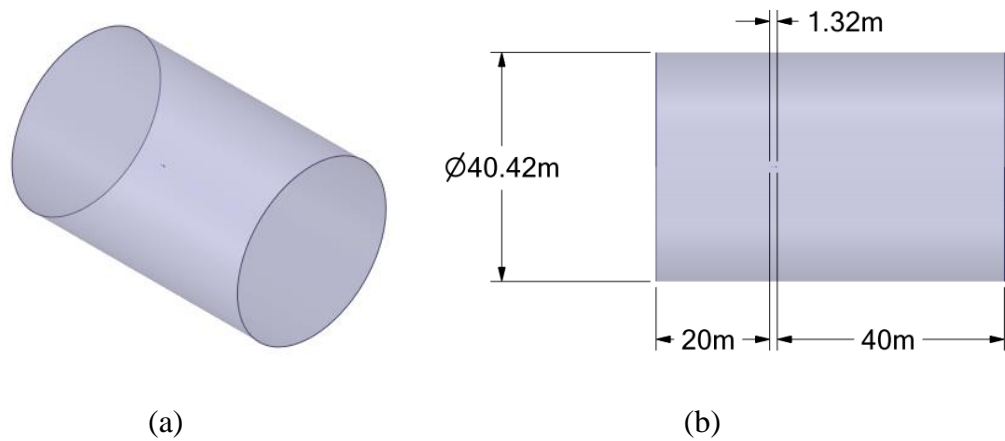
Figure 2.8. Enclosure Dimensions used in CFD Validation Analysis (a) Isometric and (b) Top Views

Table 2.2 Flow Conditions used for MICOM Grid Fin CFD Analyses

Free Stream Mach	2.5
Free Stream Static Pressure	15168.465 Pa
Free Stream Static Temperature	128.88 K
Angle of Attack	-3°, 0°, 3°, 5°, 7°, 10°, 12°, 15°
Roll Angle	0°
Deflection Angle	0°

In the meshing process, polyhedral mesh elements were generated as mentioned in the Section 2.3. In the near-wall region, 20-layers of viscous padding elements were created to obtain a well-captured boundary layer. Nearest cells to the walls, boundary layer mesh height is calculated to have y+ values around 1 and set to 0.003 with a 1.05 growth rate setting. In order to assess the viscous layer mesh quality in the selected mesh resolution, y+ values are plotted against the position in x direction and given in Figure 2.9. In this graph, all y+ values are plotted to ensure obtaining the maximum value of y+. Even though y+ values increases up to 2.5 in grid fin region, it is considered as sufficient in this study. 6.3 million polyhedral volume elements were created for CFD analyses. In Figure 2.10 and Figure 2.11, the boundary mesh for pressure far field and missile body surface are shown, respectively. To illustrate the volume mesh elements, a cut plane obtained from x-z plane is presented in Figure 2.12.
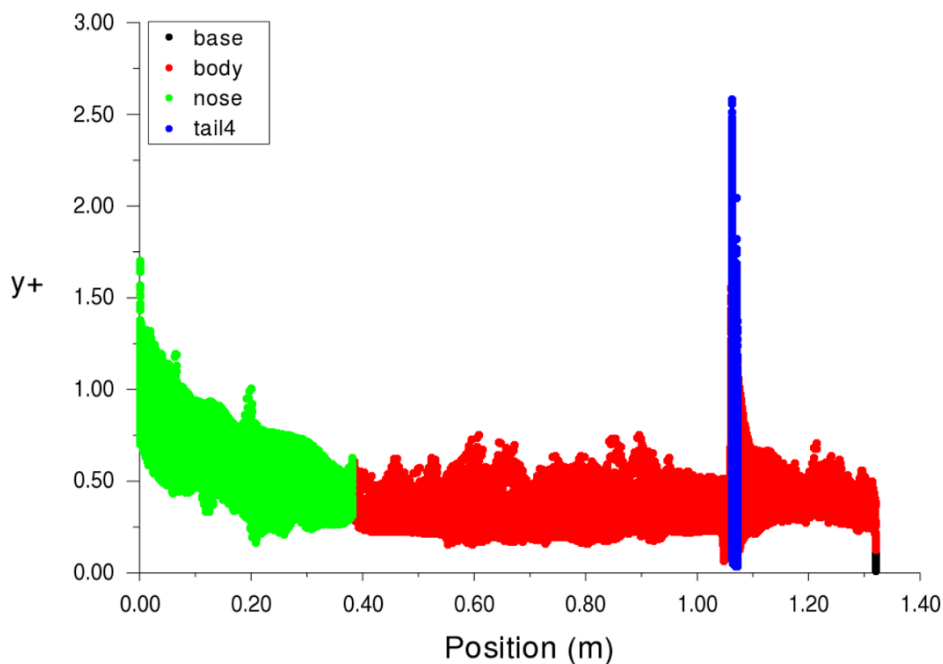
Figure 2.9. A sample MICOM CFD Analysis y+ Values with Finest Mesh Resolution
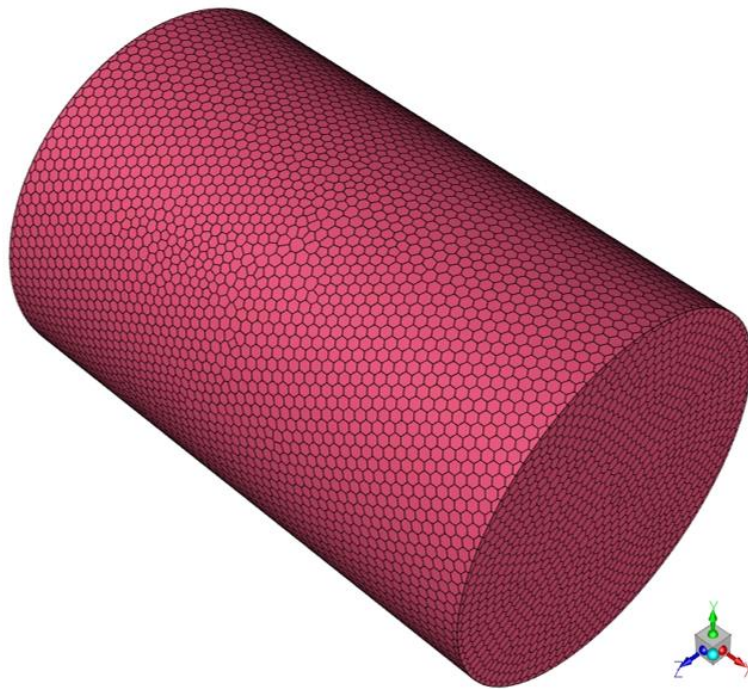
Figure 2.10. Pressure Far Field Boundary Mesh used in CFD Validation Analyses
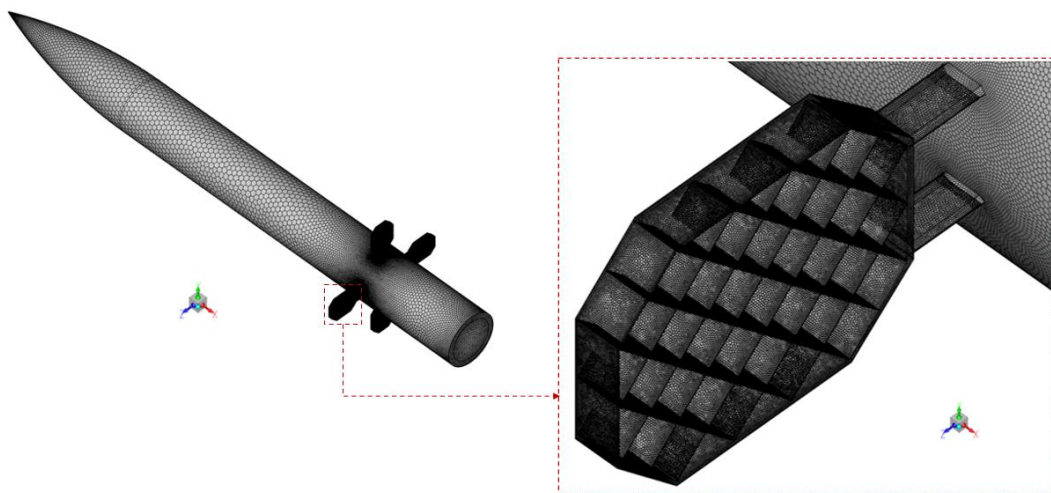
Figure 2.11. Missile Body Surface Mesh used in CFD Validation Analyses and A
Closer Look to One of The Grid Fin
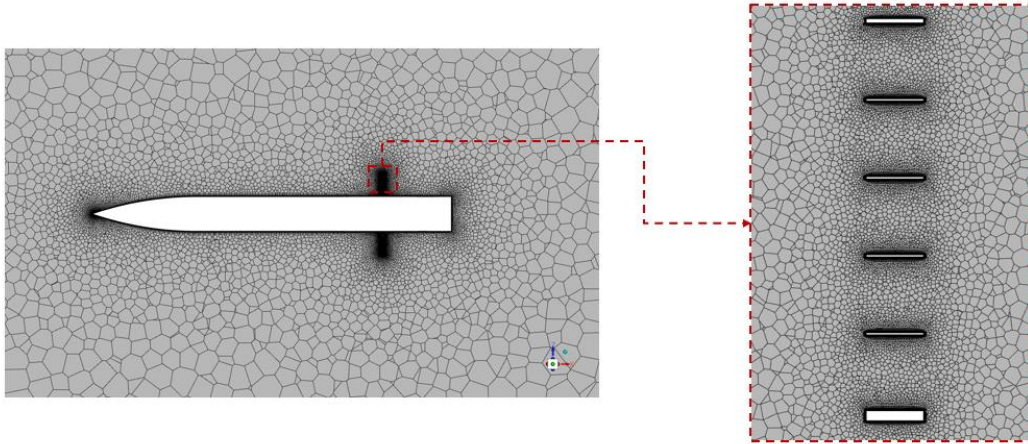
Figure 2.12. Volume Mesh Cut Plane (x-z) View around Missile Body and a Closer Look to One of the Grid Fin

2.4.3 Mesh Independence Study

In any CFD analysis, a mesh independence study must be performed to ensure that the created mesh is able to capture the flow details accurately. In order to perform a mesh independence, at least three significantly different sets of grids should be selected and run simulations. It is desirable that the grid refinement factor, in other words ratio of fine to coarse mesh, be greater than 1.3 [46]. For the mesh independence study, five different mesh resolutions are selected. Starting from very coarse grid, following finer grid is created considering the number of cells to be the previous grid resolution multiplied by roughly about 1.4. The mesh details are given in Table 2.3. Different mesh resolutions are shown in Figure 2.13 and Figure 2.14.

Table 2.3 Different Mesh Resolutions and Their Volume Element Counts

Mesh Name	Very Coarse	Coarse	Medium	Fine	Very Fine
Volume Element Count (x10^6)	4.3	6.6	9.0	12.7	18.6
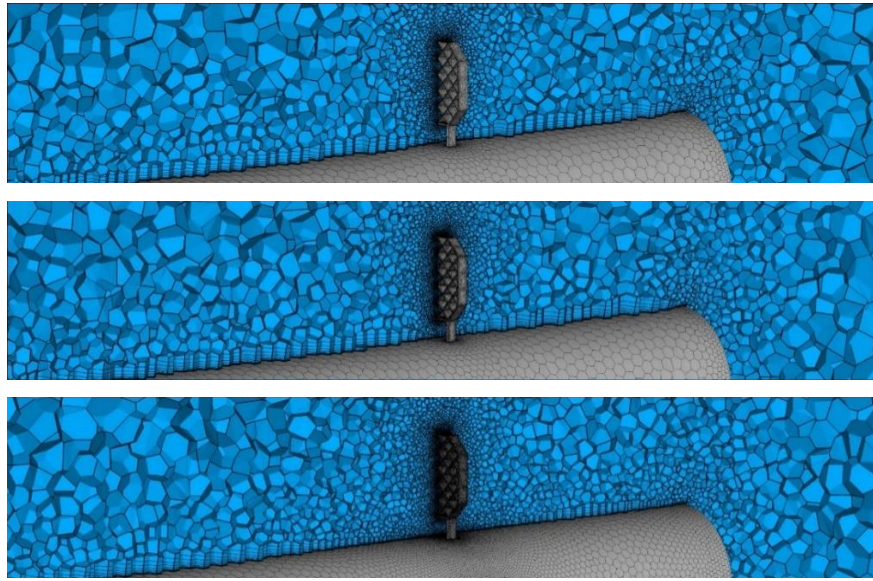
Figure 2.13. Isometric Views of Very Coarse (top), Medium (middle) and Very Fine (bottom) Mesh
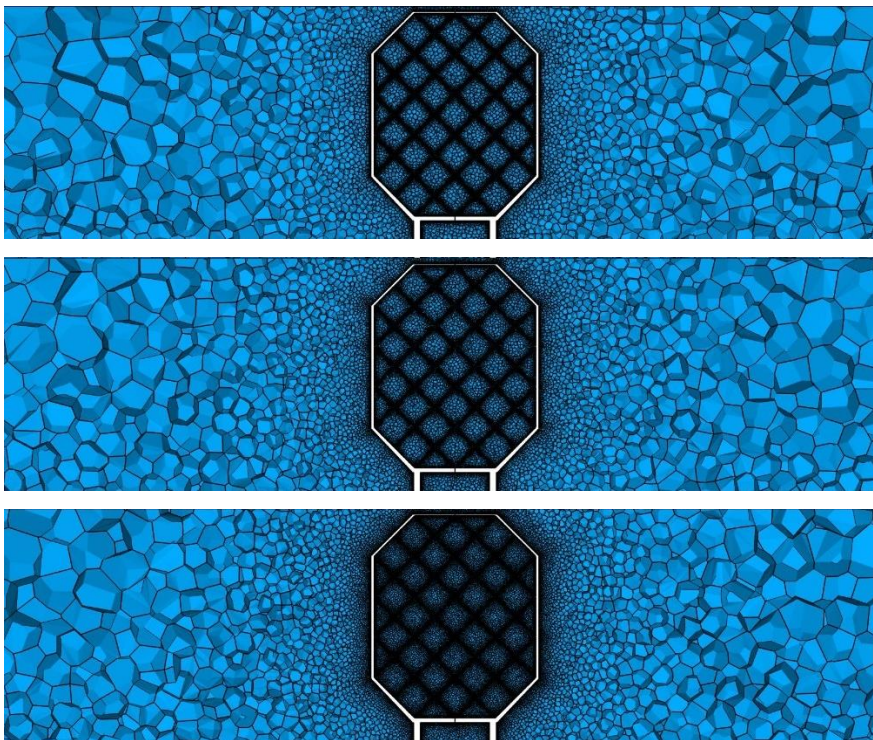
Figure 2.14. Front Views of Very Coarse (top), Medium (middle) and Very Fine (bottom) Mesh

Since the coefficients are very small, relative error calculation is not appropriate because dividing a value to very small number gives unreal error levels. Hence, the minimum and maximum values for each aerodynamic coefficient is used as denominator. Moreover, there are many angles of attack, therefore, for each angle of attack the changes in aerodynamic coefficients are calculated, and the absolute mean value is obtained using these values. The mean absolute change formula is defined as:

$$\bar{\Delta}_{mr} = \frac{100 * \sum_{i=1}^{n} \frac{\left|x_i{}^{fmr} - x_i{}^{mr}\right|}{\left|max(x_1{}^{fmr}, \ldots, x_n{}^{fmr})\right| + \left|min(x_1{}^{fmr}, \ldots, x_n{}^{fmr})\right|}}{n} \quad (2.17)$$

In this equation, "fmr" represents finest mesh resolution and "mr" shows the evaluated mesh resolution. Also, "i" is the index representing the angle of attack values. Hence "n" is the number of angle of attack values.

In the mesh independence study, firstly, each mesh resolution results are compared by the finest mesh resolution and average change in aerodynamic coefficients are plotted in Figure 2.15. The results showed that between fine and very fine mesh resolutions, the average change in aerodynamic coefficients except hinge moment coefficient is under 1 percent. Even though the hinge moment coefficient is very small, the change is about 1.5 percent, therefore, the finest mesh resolution (18.7 million volume elements) is used for further studies in the thesis. For further comparison of these mesh resolutions, the aerodynamic coefficients are plotted against the angle of attack, including the experimental results as well. These graphs are shown in Figure 2.16-Figure 2.19. In these graphs, the differences between mesh resolutions already so small, hence further refinement of mesh resolution seems to be unnecessary.
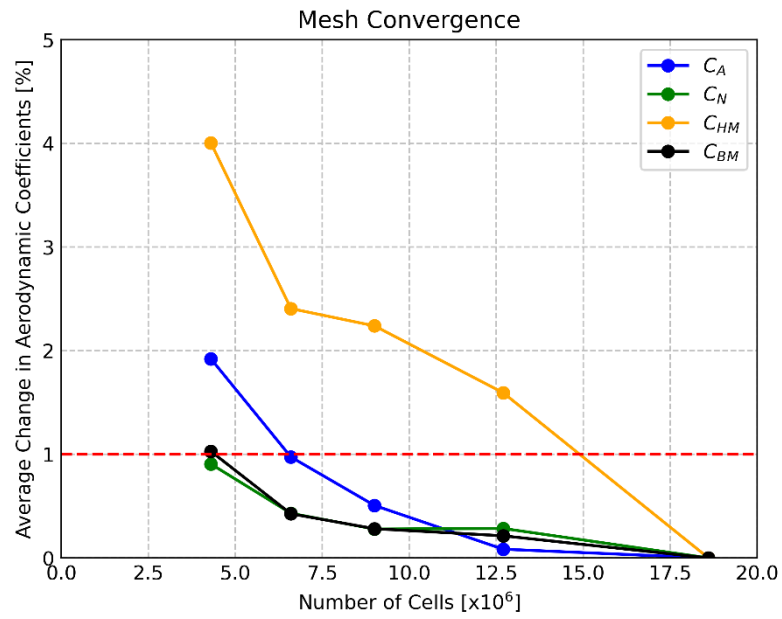
Figure 2.15. Average Change in Aerodynamic Coefficients with Respect to Number of Mesh Elements Compared to Finest Mesh Resolution
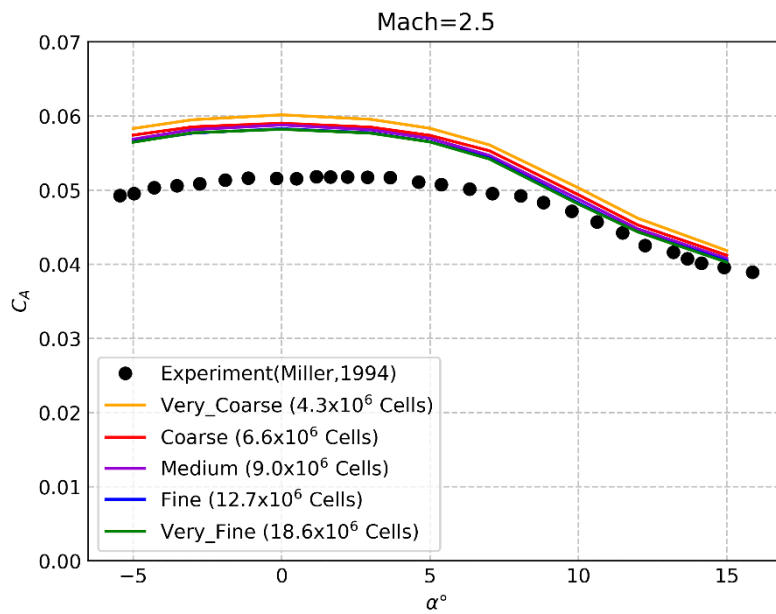
Figure 2.16. Mesh Resolution Comparison of Axial Force Coefficient (C_A)
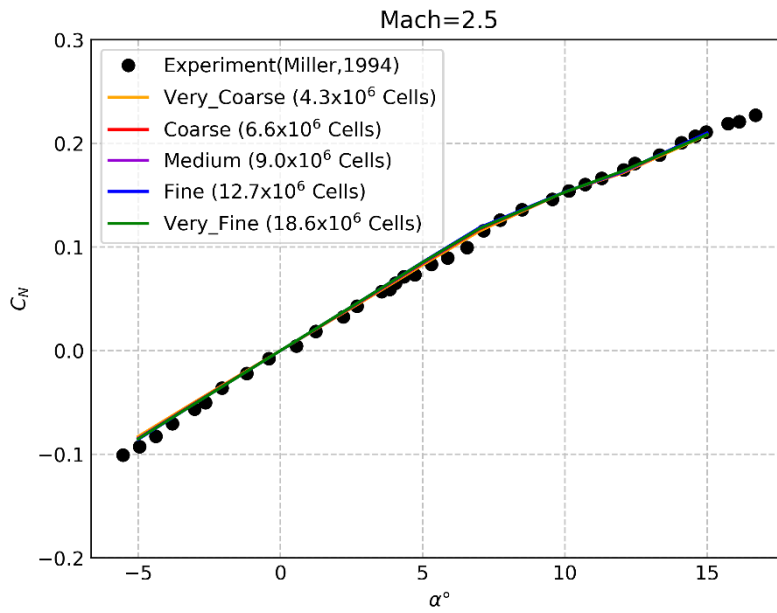
Figure 2.17. Mesh Resolution Comparison of Normal Force Coefficient (C_N)
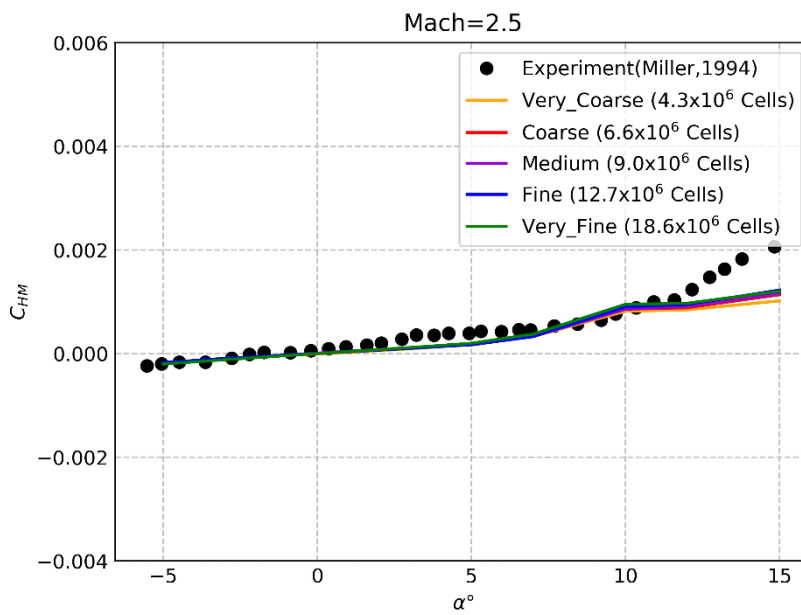
Figure 2.18. Mesh Resolution Comparison of Hinge Moment Coefficient (C_{HM}) about Hinge Line
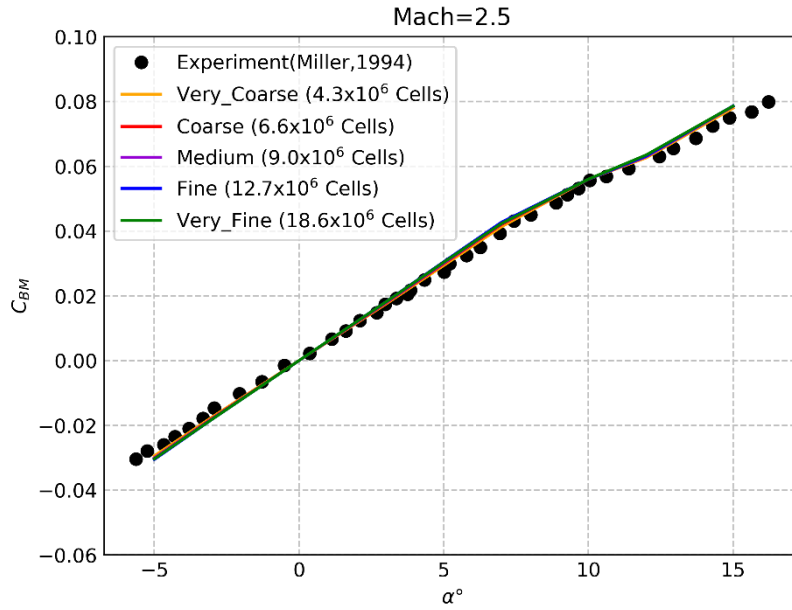
Figure 2.19. Mesh Resolution Comparison of Bending Moment Coefficient (C_{BM}) about the Fin Root

2.4.4 Turbulence Model Study

In this thesis study, three turbulence models, namely, Spallart-Almaras, k-ε Realizable and, k-ω SST, are used and most accurate one is selected for further CFD analysis. The details of these turbulence models are explained in Section 2.2.5. The comparisons of these turbulence model results are shown in Figure 2.20-Figure 2.23 for each aerodynamic coefficient separately.
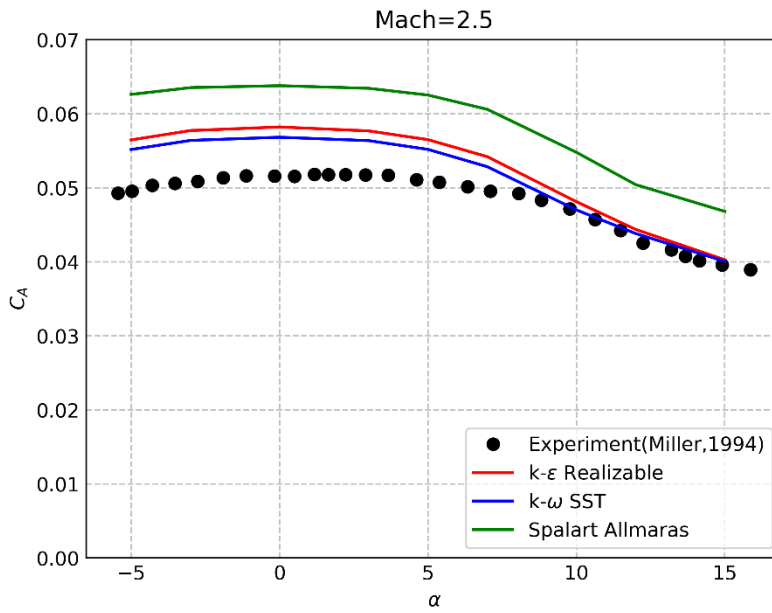
Figure 2.20. Turbulence Model Comparison of Axial Force Coefficient (C_A)
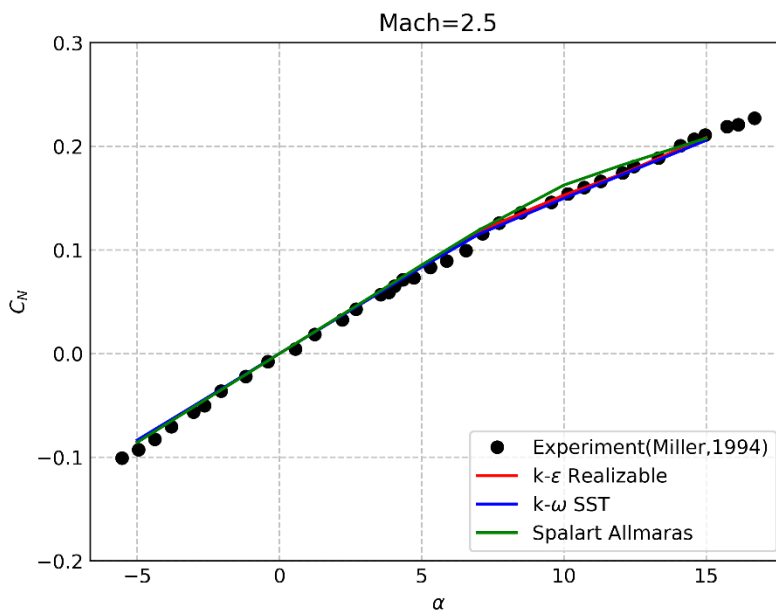
Figure 2.21. Turbulence Model Comparison of Normal Force Coefficient (C_N)
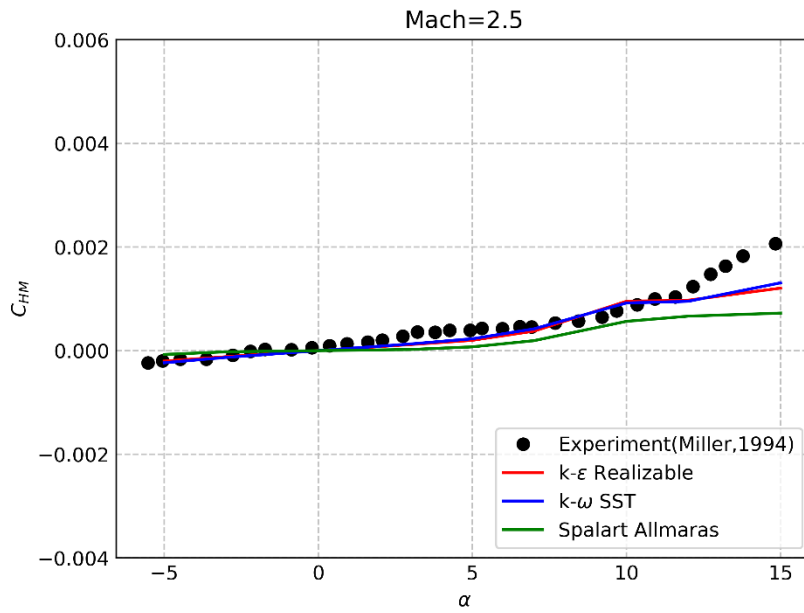
Figure 2.22. Turbulence Model Comparison of Hinge Moment Coefficient (C_{HM}) about Hinge Line
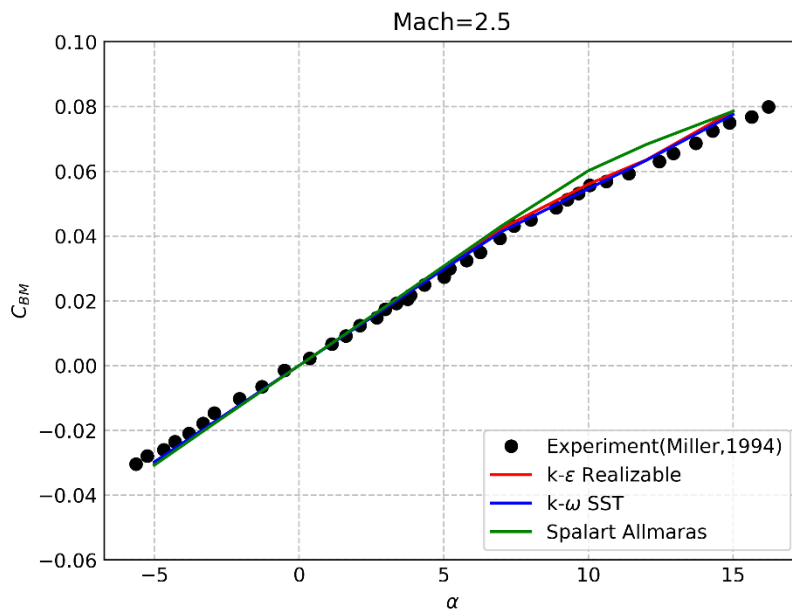
Figure 2.23. Turbulence Model Comparison of Bending Moment Coefficient (C_{BM}) about the Fin Root

As it can be seen from the results, k-ω SST turbulence model is more accurate for MICOM grid fin case. For further CFD analysis in thesis, k-ω SST turbulence model is used.

When the results compared with the available experimental data, good agreement is achieved although some discrepancies are observed in the axial force and hinge moment coefficients. The reasons behind this inconsistency may be resulted from:

• The numerical errors in the calculations discontinuity regions inside grid fin structure may lead to misplaced center of pressure, resulting in hinge moment errors.

• The fact that the hinge moment coefficient is very small in magnitude, hence a minor difference in the hinge line location can lead to huge differences in hinge moment calculations.

• Slight differences generating CAD geometry.

• Differences arise from modelling the CAD geometry free from tolerances which may exist in the wind tunnel model, since the uncertainity quantification in terms of both wind tunnel model production and aerodynamic force and moment measurements is not stated in the validation test case.

CHAPTER 3

DESIGN METHODOLOGY

In this chapter, the design parameter investigation methodology is explained. Different grid fin geometries are created and investigated with CFD analyses. The geometries are determined in the first place by the commercial data visualization and statistical analysis tool, JMP, and at the end, all results are investigated again in the same software for parameter screening. After all CFD analysis results are obtained, response surfaces corresponding for each aerodynamic coefficient are generated using a commercial software HEEDS. Finally for further investigation, flow fields of selected design are created and presented. Steps followed in the investigation process is shown in the Figure 3.1. The dashed lines are only followed once but others create a loop.
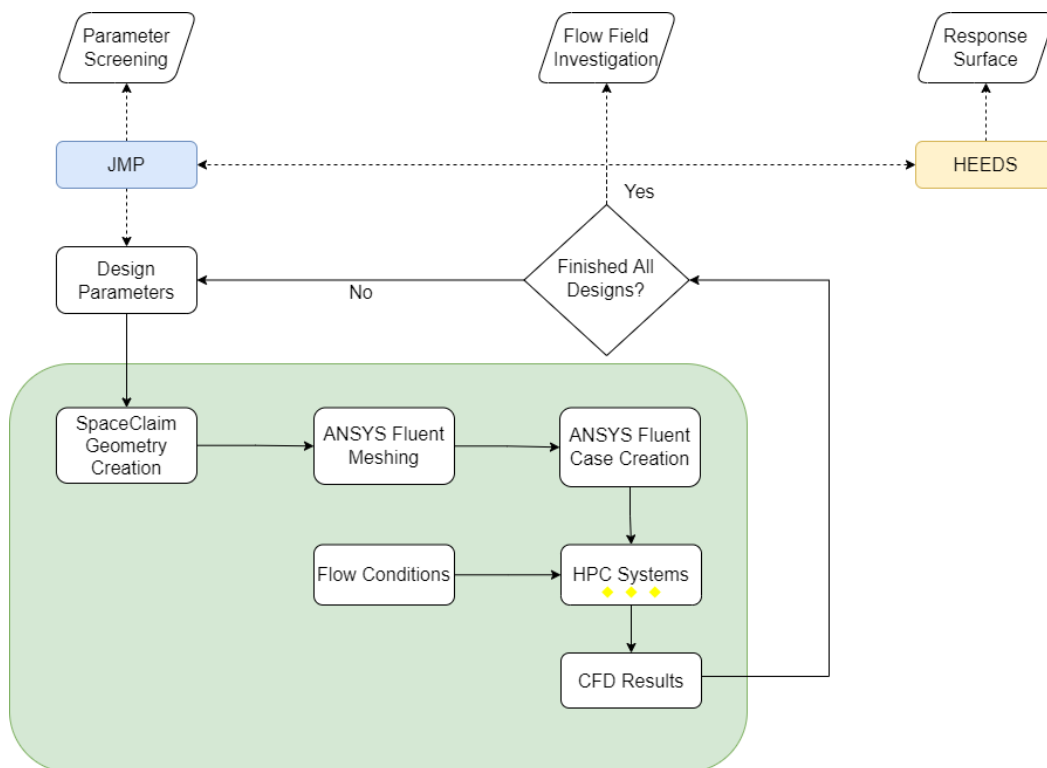
Figure 3.1. Design Methodology Flowchart

3.1   Geometry Parametrization

In order to create different grid fin geometries automatically, a geometry generation script is prepared. This script is a Python based ANSYS SpaceClaim Design Modeler script which is capable of generating the geometries according to the grid fin shape parameters. The grid fin shape parameters are defined in Table 3.1 and shown in Figure 3.1.

Table 3.1 Grid Fin Shape Parameter Definitions

Parameter	Definition
Chord (c)	The length of the grid fin in the incoming flow direction
Span (s)	The root-to-tip distance of grid fin
Width (w)	The side-to-side distance of grid fin
Gap (g)	Diagonal distance in the spanwise direction of a grid cell
k	The web profile fraction of chord to reach maximum thickness
Wedge Angle (γ)	Leading and trailing edge wedge angle
Cell Angle (θ)	The angle between adjacent surfaces of grid cell.
Frame Thickness (t_f)	Outer frame thickness
Web Thickness (t_w)	Inner web thickness
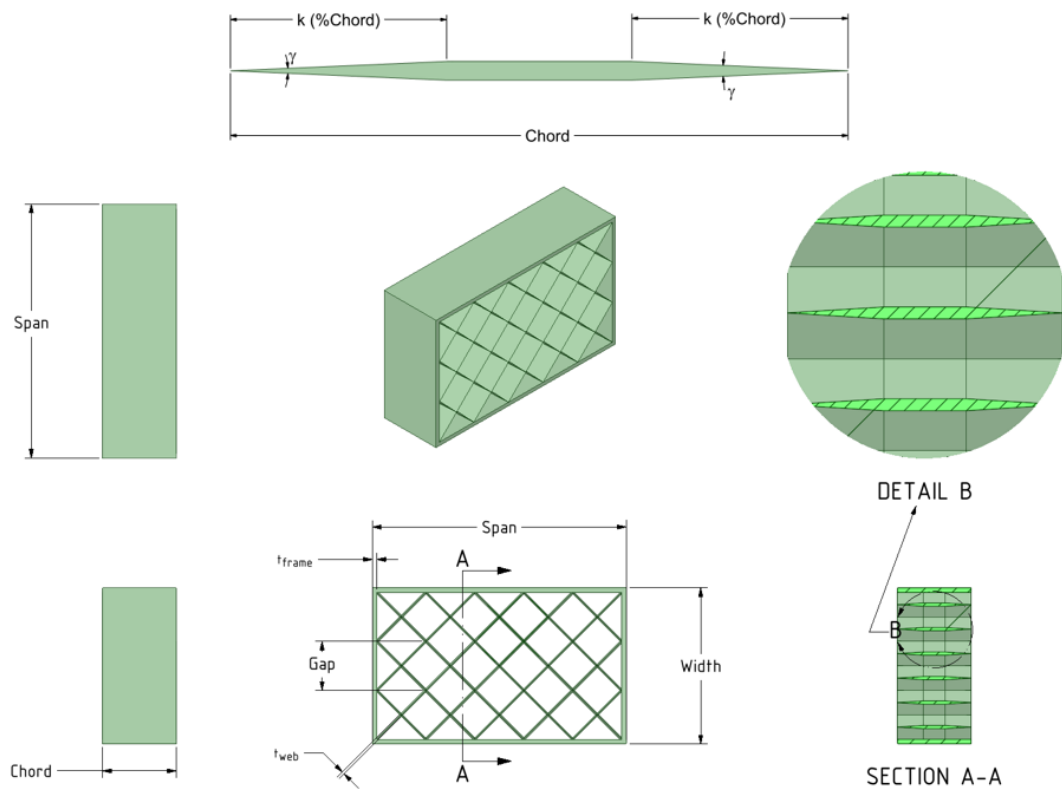
Figure 3.2. Illustration of Grid Fin Parameters
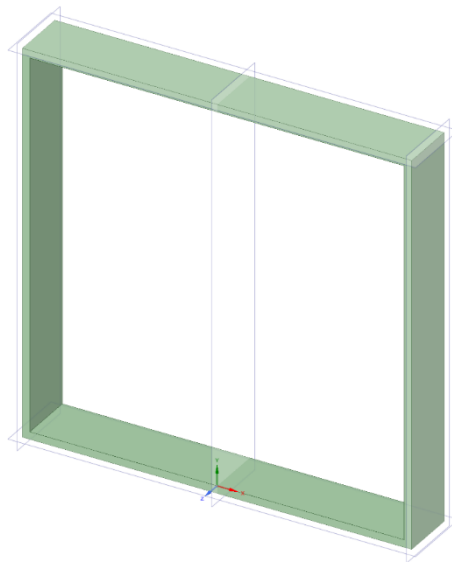
Figure 3.3. Outer Frame

In the grid fin geometry parametrization process applied here, first an outer frame is constructed. An outer frame is illustrated in Figure 3.3. The frame creation part in the script only depends on the chord, span, width, and frame thickness parameters. After the outer frame is created, the inner web structure creation process starts. This part is the most challenging part in the geometry creation process. The frame is cut in half in the symmetry plane in this case y-z plane. Then, a series of inclined surfaces are created as dictated by the cell angle, starting from origin and going to the frame boundary in the upward direction. This process is shown in Figure 3.4. Now, the inclined surfaces are created also in the reverse direction, starting from the uppermost location in the spanwise direction and goes all the way through the frame boundary. Thus, these surfaces intersect with the previously created inclined surfaces to create grid fin cells. Then, the obtained geometry is mirrored with the symmetry plane. The created half grid fin and mirrored geometry is presented in Figure 3.5. Later, the excess web parts left over from the web creation is cut off using the planes located to the outer frame surfaces. This process is shown in Figure 3.6. Finally, orientation adjustments are made, and the grid fin geometry creation process is finished.
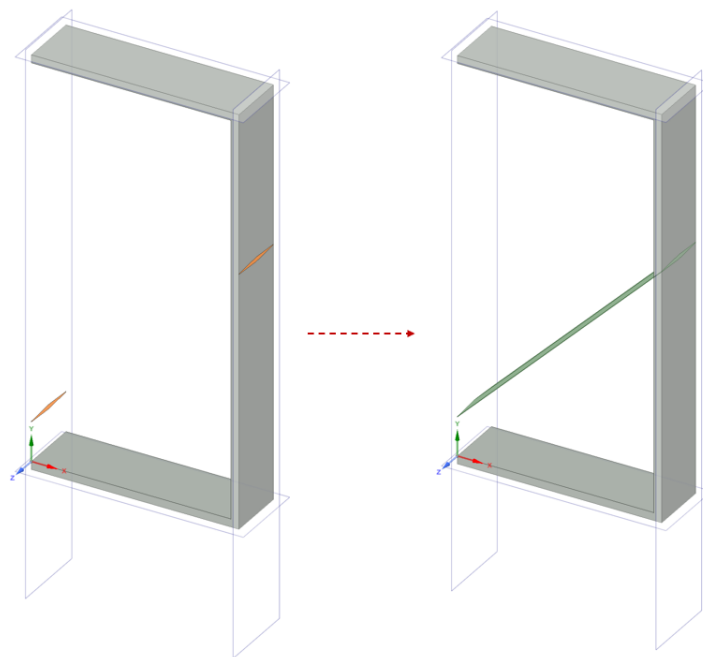
Figure 3.4. Inclined Surface Creation in The Upward Direction
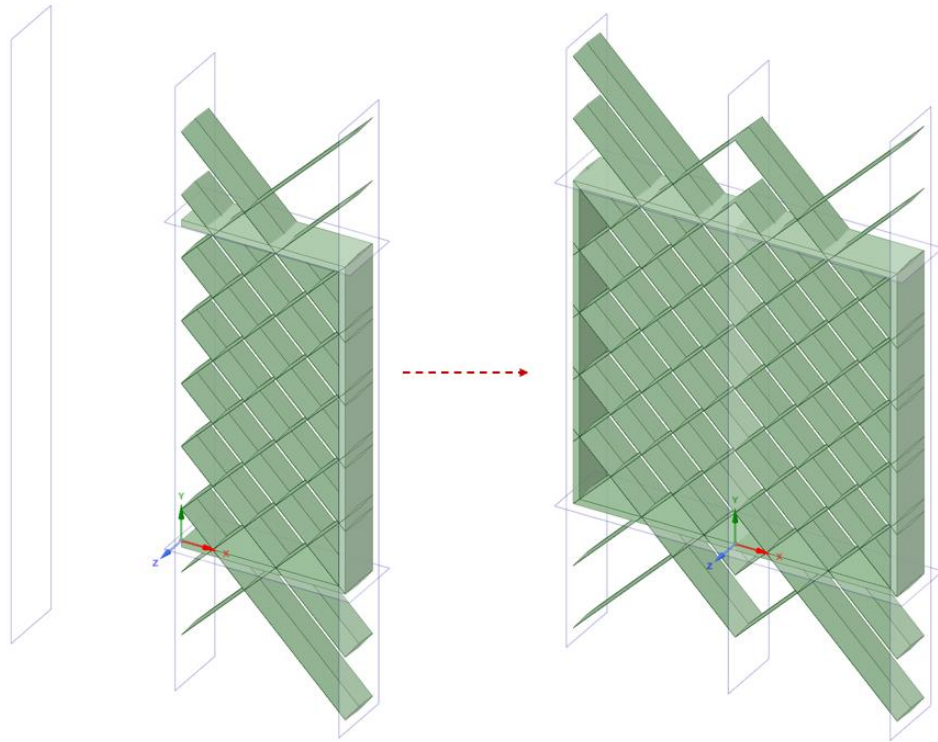
Figure 3.5. Half Portion of Grid Fin and Mirrored Geometry
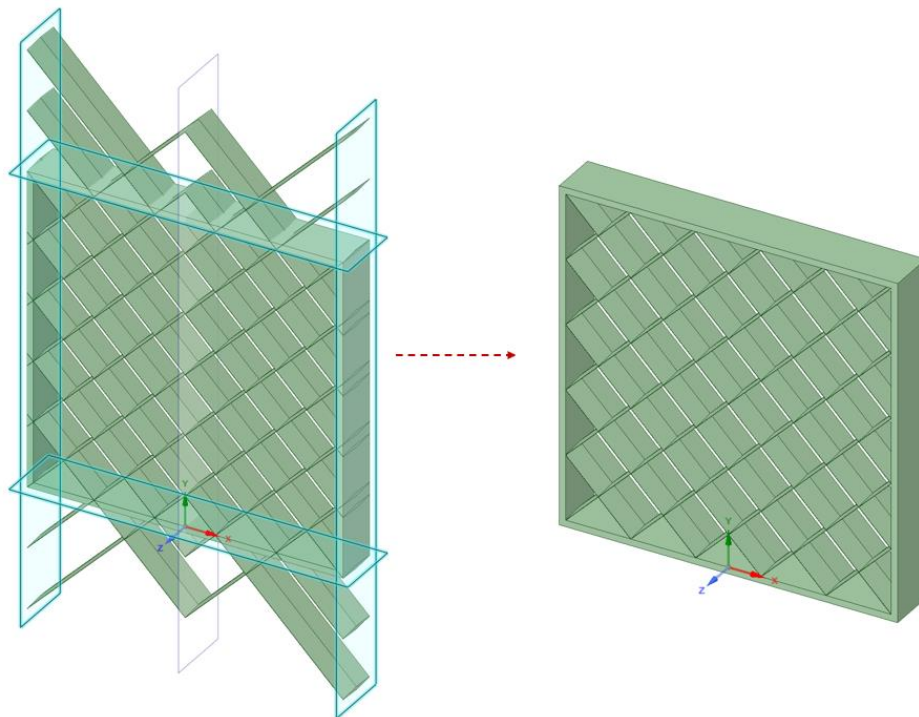
Figure 3.6. Excess Part Removal Process

Although the grid fin geometry is created, it is not ready for meshing process. The last part of the SpaceClaim script is dedicated to preparing the grid fin for mesh generation procedure with, "Body of Influence" and "Enclosure" creation steps. The "Body of Influence" (BoI) is the process applied when it is needed to have finer volume mesh resolution in a certain region. In the thesis, a BoI region is created in order to resolve the flow inside and near grid fin geometry better. The BoI details are presented in Figure 3.7. The radius of BoI is changing with span and width of grid fin. BoI center is located to the center of grid fin. To enclose the grid fin, diagonal distance from the grid fin center point is calculated and multiplied by a factor to ensure the BoI boundaries does not intersect with grid fin surfaces. The expression for the BoI radius is given in Equation (3.1).

$$r = 1.5 \sqrt{(0.5s)^2 + (0.5w)^2}$$
(3.1)
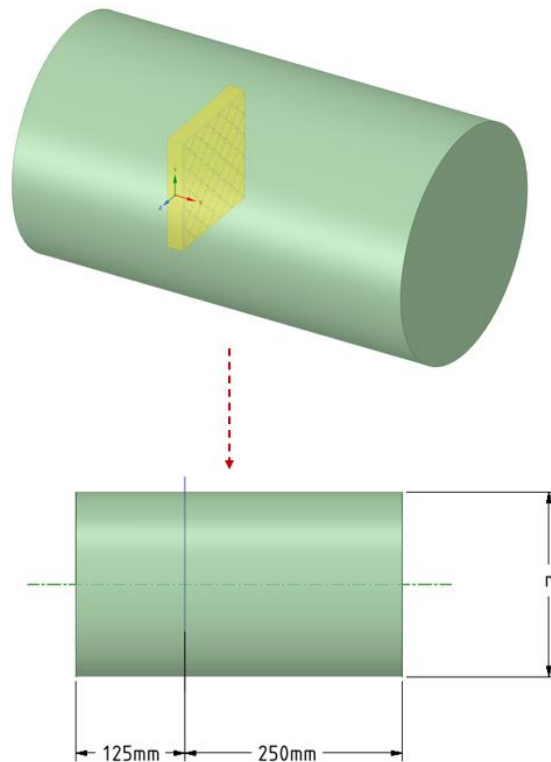
Figure 3.7. Body of Influence and its Dimensions

50

The enclosure preparation part of the script is similar with the BoI creation except the radius is constant. To represent pressure far field, dimensions of enclosure are adjusted as at least 8 times in the upstream, 16 times in the downstream and 8 times in the radial direction of the maximum grid fin span. The dimensions of the computational domain is shown in Figure 3.8.
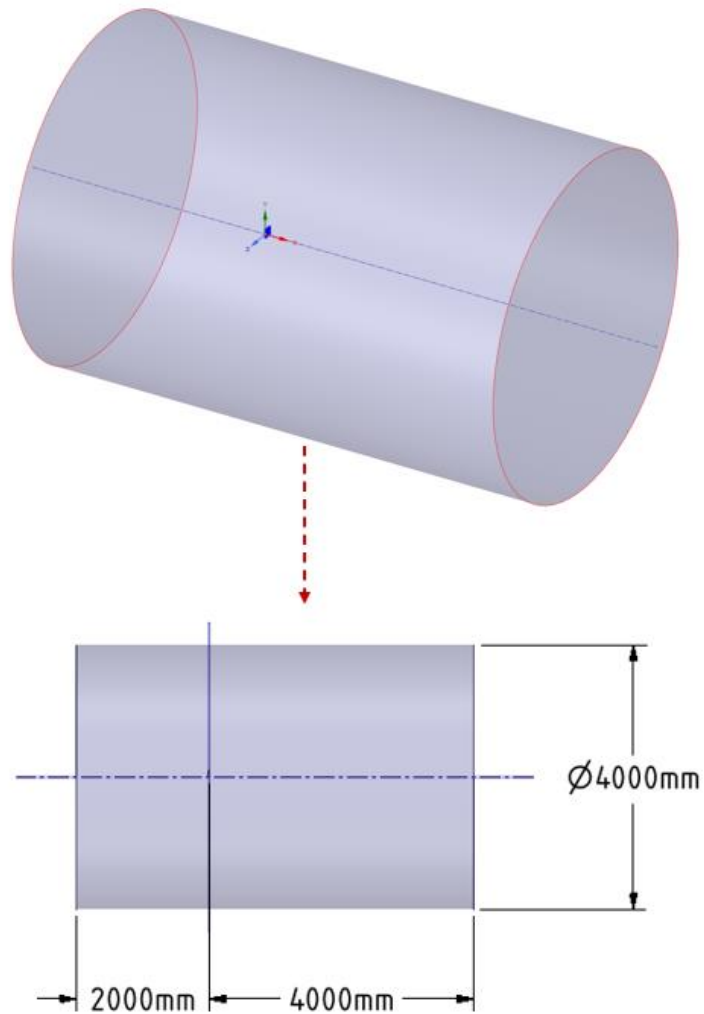
Figure 3.8. 3D Cylindrical Computational Domain and its Dimensions

3.1.1 Parameter Selection

The grid fin geometry script is capable of producing grid fins as the parameters dictated, however, some parameters have been excluded for the scope of this thesis. Included and excluded parameters and the reason for the exclusion is explained here. The chord, span, width, and gap are the main parameters; hence they are all included in this work. The chord, width, and span are defined as a ratio of gap value. Frame and web thickness parameters are also included since the axial force is important for the grid fin aerodynamic performance. However, frame thickness is included as the ratio of web thickness because the frame should be enduring to support the internal web structure efficiently. Therefore, the frame thickness is set to be at least as thick as the internal webs. The web thickness is again defined as a ratio of gap. The cell angle kept constant as 45° throughout this work since as explained in the Section 1.3, the cell pattern or in this case angle between adjacent web members does not affect the aerodynamic performance [32].

3.1.1.1 Preliminary Design Studies

Before the detailed design study, a preliminary design study and CFD analyses of grid fin are performed to investigate the effects of selected design parameters. Preliminary analyses of grid fin are performed for Mach number of 2.5 and angles of attack ranging from 0 to 15 degrees [53]. The results are presented in this section. In this part of the thesis, 7 designs are created for investigating the effects of gap, wedge angle, and leading and trailing edge wedge fraction parameters of grid fin. The effect of each parameter is explored holding the other two parameters constant in this study. A sample grid fin configuration is shown in Figure 3.9 and it includes a 100-mm cylindrical holder for attachment of grid fin. It should be noted that, chord, span and width parameters are the same for all configurations.
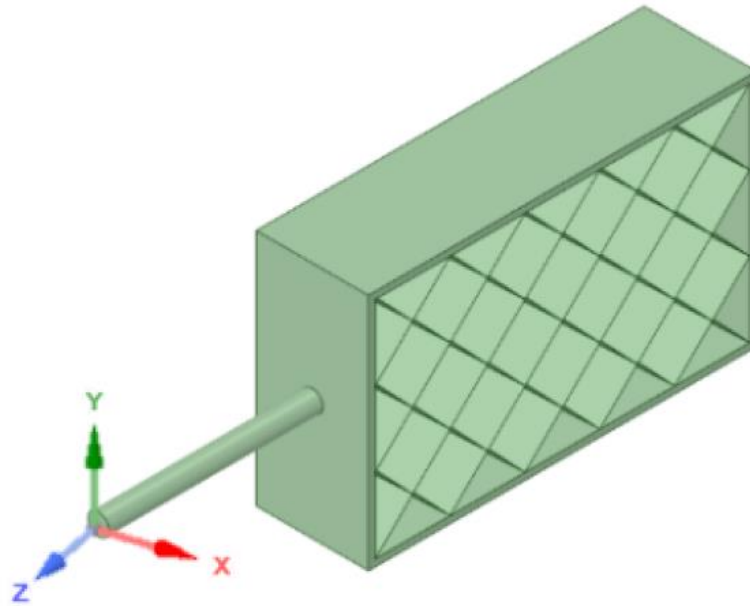
Figure 3.9. Sample Grid Fin Configuration in Preliminary Design Study

The results of this study showed that decreasing the gap value dramatically increases the axial force coefficient and decrease normal force coefficient. Mach contours at 10° angle of attack are presented for different designs in Figure 3.10. Web thickness, leading and trailing edge chord fractions (k) and wedge angle (γ) are the parameters that define web cross-section as explained earlier. In this study, k, and γ are investigated, however, since these two parameters directly alter the web thickness, the results of these explorations point out the importance of the web thickness parameter. Therefore, an airfoil selection procedure is applied to reduce the number of parameters. Moreover, holder is affecting the flow around the grid fin. The holder parameters may be included to design parameters, however, there are numerous design alternatives and even if it is modelled as simple cylinder, two parameters, length and diameter, comes into picture. Therefore, the holder is excluded in the next studies.
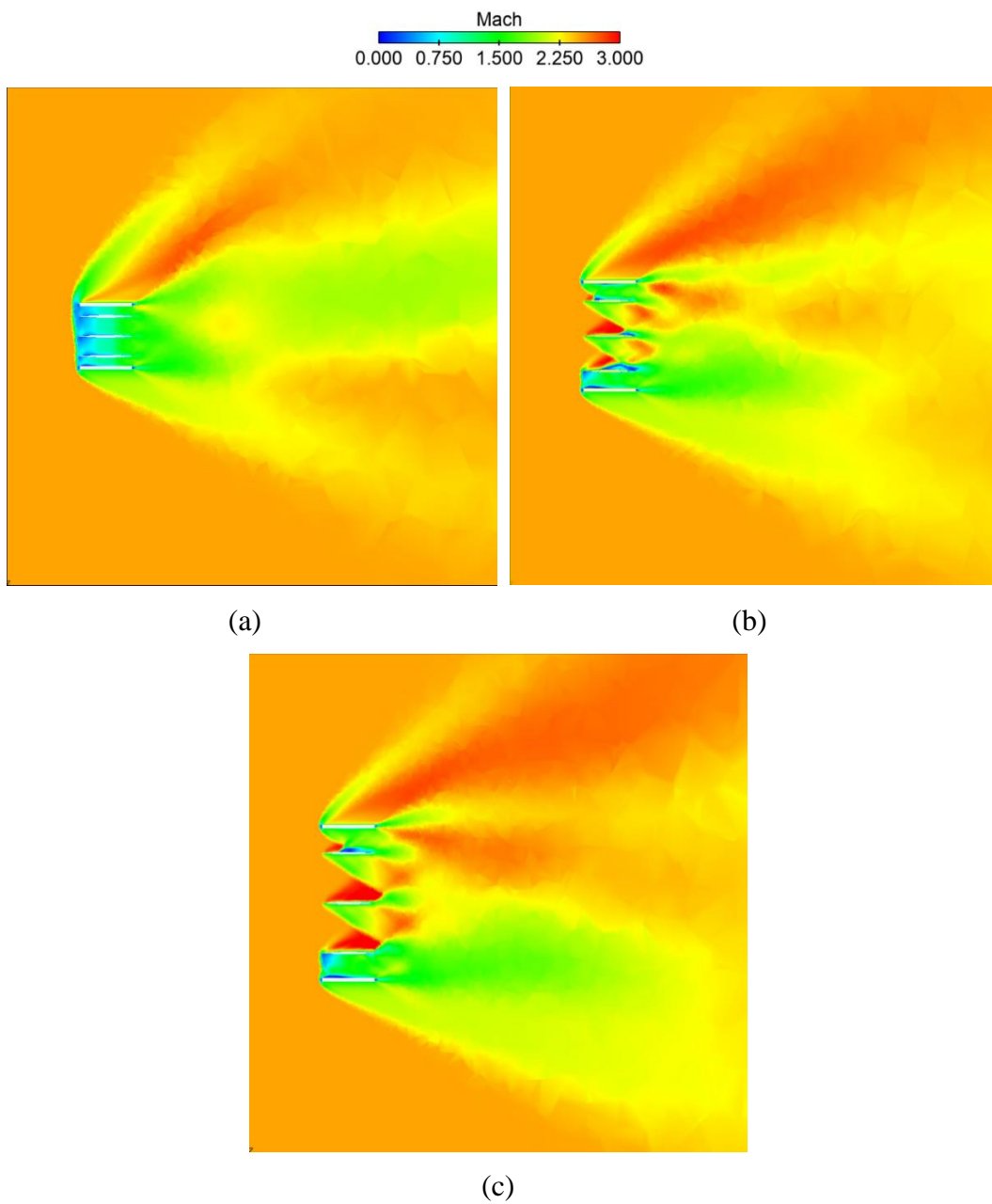
Figure 3.10. Cut-Plane Mach Contours of Designs Having Gap Values of (a) 20mm, (b) 35mm, (c) 50mm at 10° Angle of Attack

3.1.1.2   Airfoil Selection Study

For airfoil selection study, 2D viscous CFD analyses are performed to observe the flow behaviour at Mach number of 2.5 which is the operating Mach number used in this thesis. Three different airfoils are compared in this section, F1 is the standard square thin shaped airfoil, F2 is the diamond shape airfoil and F3 is a general hexagonal shape airfoil. The corresponding Mach contours, obtained from the CFD results at 15° angle of attack, are presented in Figure 3.11. As it can be seen from the Mach contours, shock and expansion wave formation is familiar in F2 and F3. However, due to bluntness of F1 airfoil, a bow shock is created in front of the airfoil.
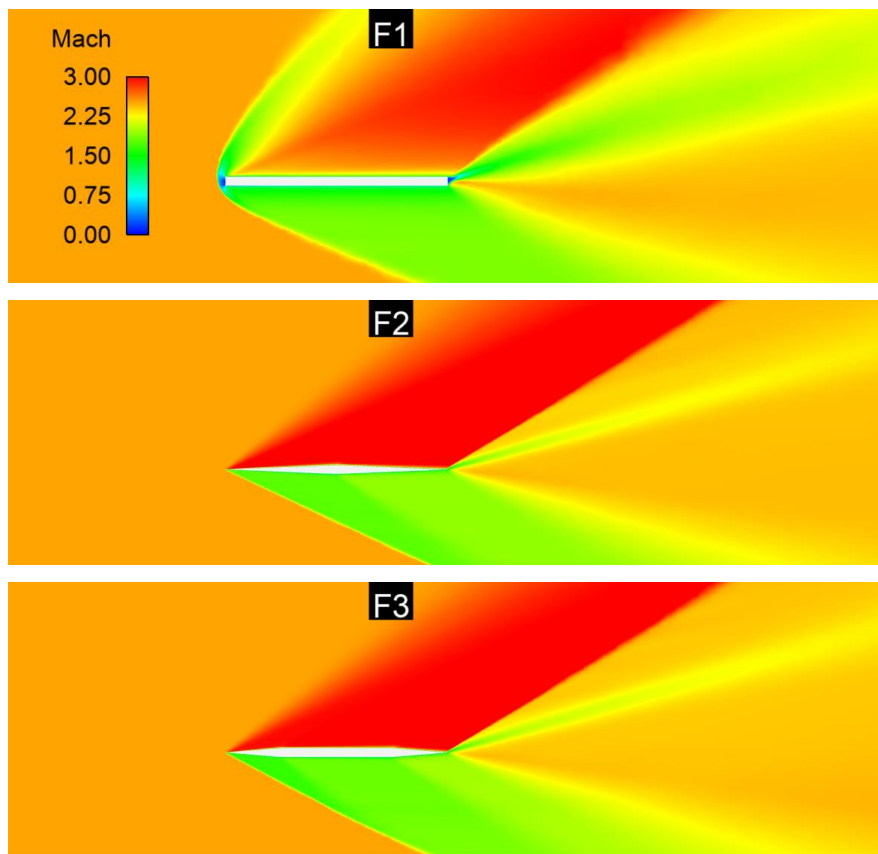
Figure 3.11. Mach Contours of Three Different Profiles at Angle of Attack of 15°

In order to measure the aerodynamic performances of these airfoil shapes, they are compared in terms of axial force, normal force and pitching moment coefficients. The aerodynamic coefficient of these airfoils are shown in Figure 3.12 - Figure 3.15. The results showed that the blunt squared airfoil F1 has the highest axial force coefficient value, 7 times of the others. Even though the F2 and F3 airfoils are similar in the order of magnitude, diamond shape airfoil F2 has the smallest axial force coefficient for all angle of attack values. When the normal force and bending moment coefficients are compared, F2 and F3 is slightly differs from F1. Also, when lift and drag values are compared, F2 and F3 shows much greater lifting characteristics than F1.
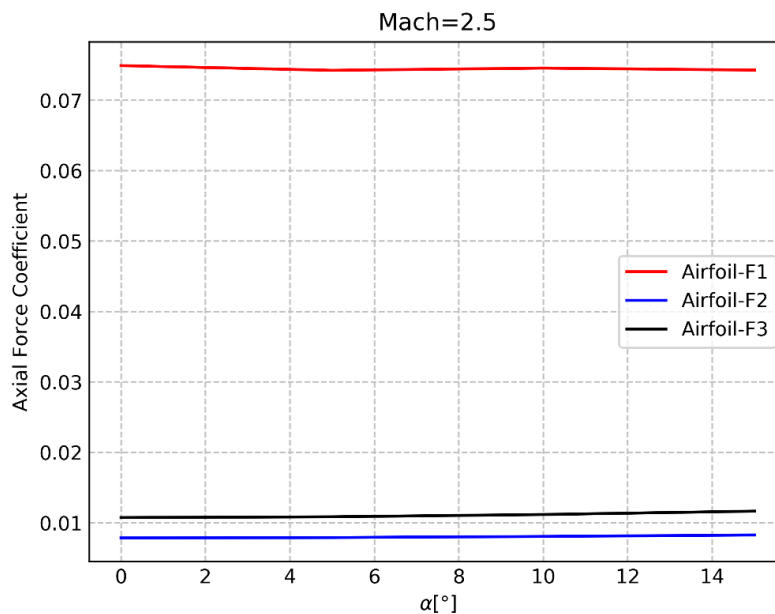
Figure 3.12. Axial Force Coefficient Comparison of Different Airfoils using 2D CFD Analyses
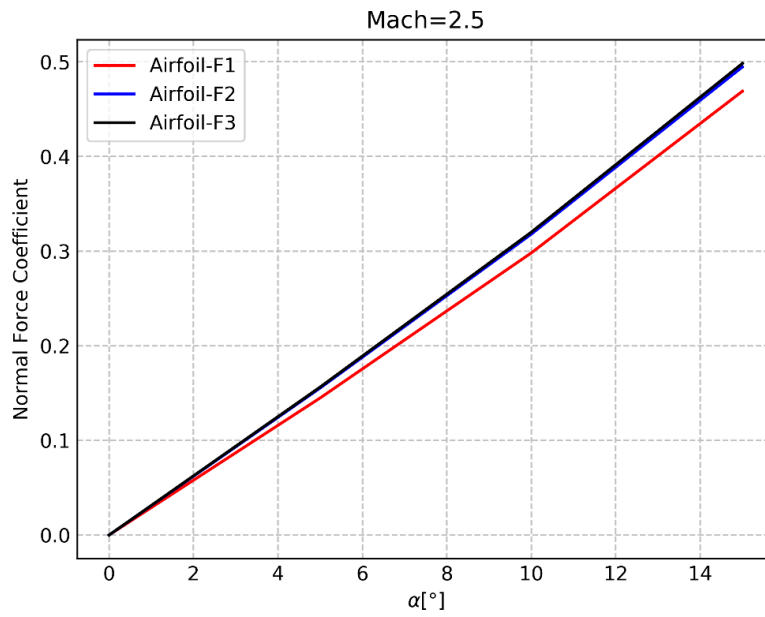
Figure 3.13. Normal Force Coefficient Comparison of Different Airfoils using 2D CFD Analyses
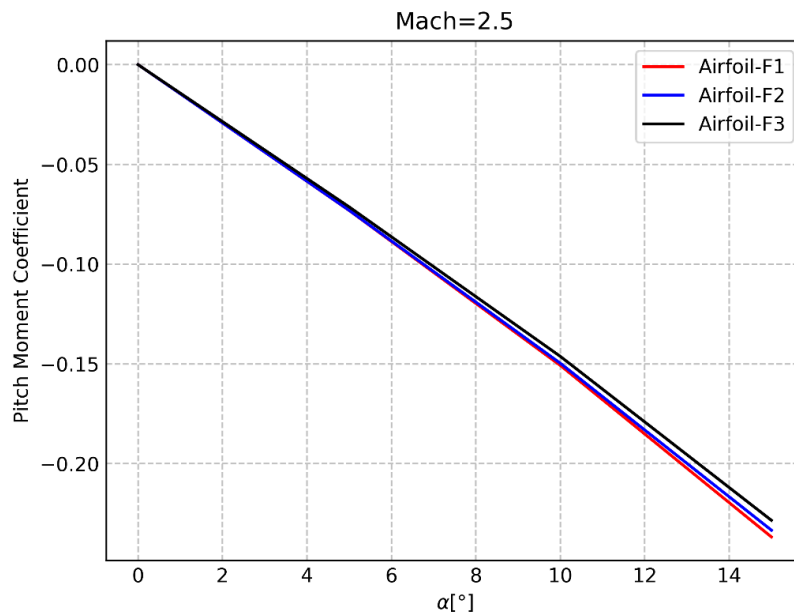
Figure 3.14. Pitching Moment Coefficient Comparison of Different Airfoils using 2D CFD Analyses
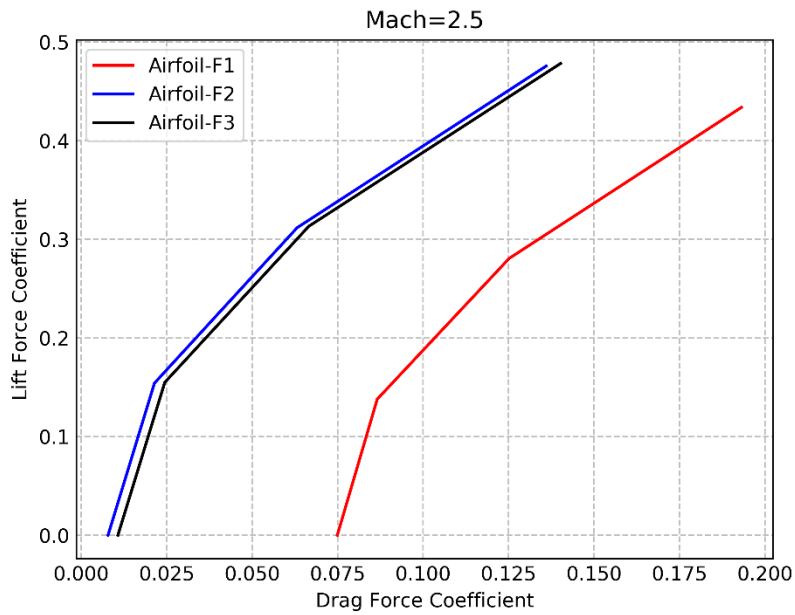
Figure 3.15. Lift Coefficient vs. Drag Coefficient Comparison of Different Airfoils using 2D CFD Analyses

In literature, when parameters of a supersonic general hexagonal airfoils investigated, it is found that the minimum drag is created for a diamond-like shape airfoil [48]. Similar results are obtained in this airfoil study, too. Hence the parameter k is set to 0.5 which creates diamond shape cross-section for internal web structures. Since the web thickness, k and γ are the co-dependent parameters, when any of the two parameters are set, the third parameter is determined automatically. Therefore, wedge angle, γ, is the parameter that can not be included in this case.

3.2 CFD Analysis Details of Grid Fins

The details of the CFD analyses performed for the different grid fin designs are described in this section. In this thesis, each design is run at angle of attack ranging from 0 to 15 degrees at Mach number of 2.5 with 0 and 45 degrees roll angles. There is no deflection angles applied because deflecting the grid fin can be replaced by additional angle of attack values because of the grid fin orientation. The sea level atmospheric conditions were used in CFD analysis.

Table 3.2 CFD Analysis Flow Conditions

Speed [Mach]	2.5
Altitude [m]	0 (Sea Level)
Angle of Attack [°]	0, 5, 10, 15
Roll Angle [°]	0, 45
Ambient Pressure [Pa] (ISA - Sea Level)	101325
Ambient Temperature [K] (ISA - Sea Level)	288.15

Solution domain is already shown in Figure 3.8. The flow conditions areassigned to pressure-far-field boundary which are given in Table 3.2. The grid fin surfaces are selected as adiabatic, no-slip wall. In the mesh generation process, scoped sizing applied to both grid fin and BOI boundaries. Scoped sizing is applied to the edges of grid fin to obtain a finer mesh resolution near the grid fin edges because shock formation in the flow mostly occurs about the discontinuties in the geometry. Also, in order to resolve grid fin better in CFD analyses, BOI refinement inside the grid fin cells is applied even though it increases the number of cell elements. BOI influence can be clearly seen in the cut-plane plots of a sample mesh which is shown in Figure 3.17. As stated in Section 2.3 and Section 2.4.2, 20 layers of viscous cell elements are applied here. In the near wall region, 0.003 mm first cell height is applied with growth setting of 1.05. The maximum y+ value is observed as 3.5 and but mostly it is around 1 and that shows the boundary layer is resolved adequately.

Since the grid fin geometries investigated in this thesis are differs from each other dimensionally, the number of volume mesh elements, i.e., grid cells, differs as well. The volume mesh counts in each design is shown in Figure 3.16.
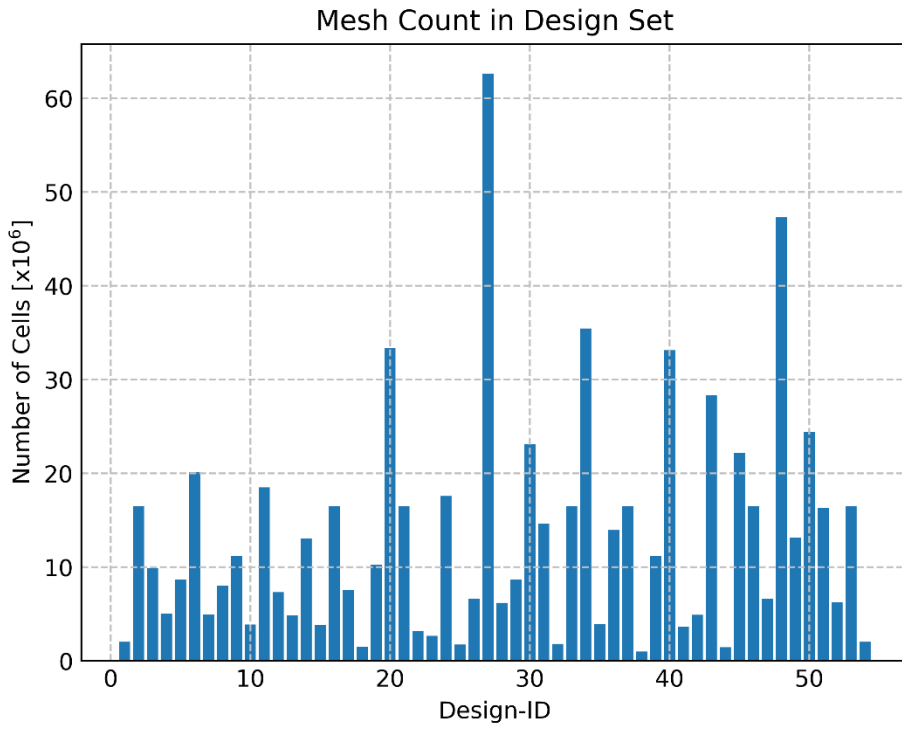
Figure 3.16. Number of Cell elements for Different Grid Fin Designs
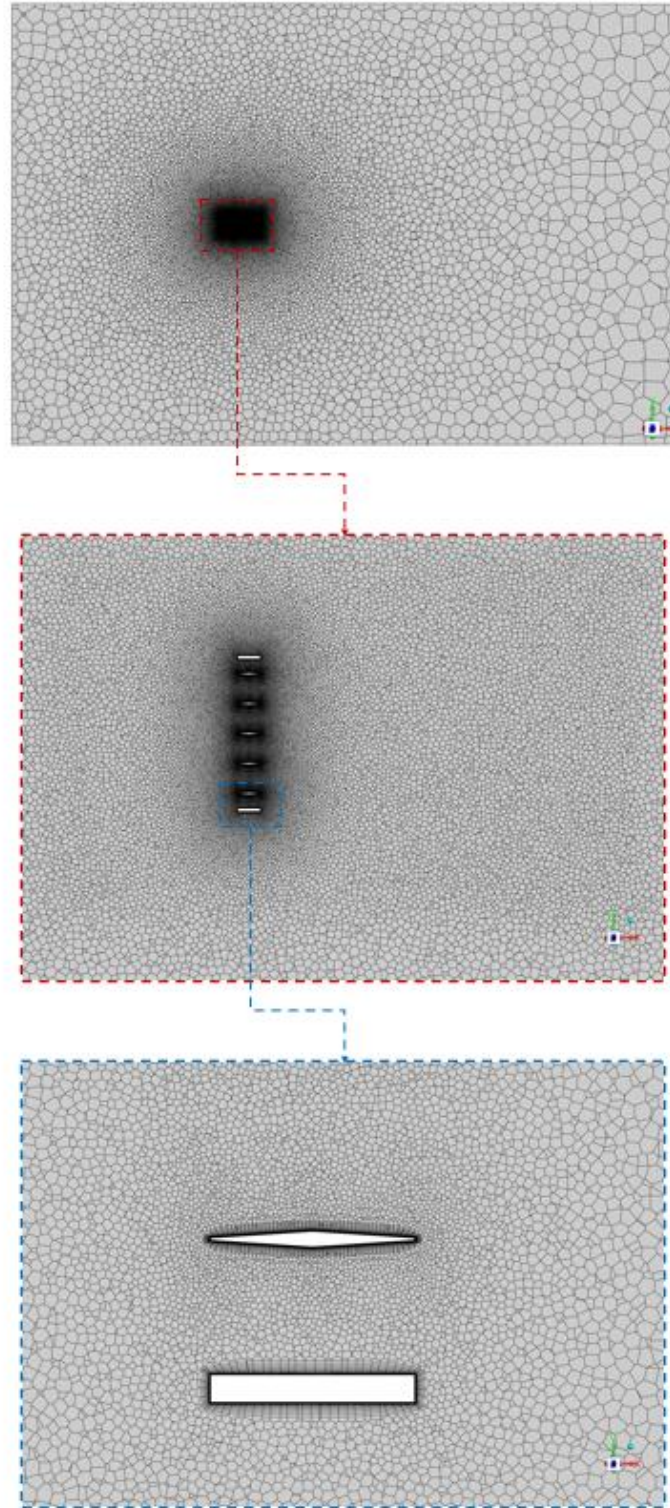
Figure 3.17. Sample Mesh Resolution of a Grid Fin in x-y Cut-Plot in the Spanwise
Middle Section

In CFD analyses, the aerodynamic coefficients are obtained using the sign convention defined in Figure 3.18. Parameters used to obtain the coefficients from the forces and moments are given in Table 3.3, where $l_{ref} = 0.127\ m$ and $S_{ref} = 0.01267$. The coefficients are obtained from dividing the integral forces and moments by corresponding parameters of reference dynamic pressure, reference length and area.
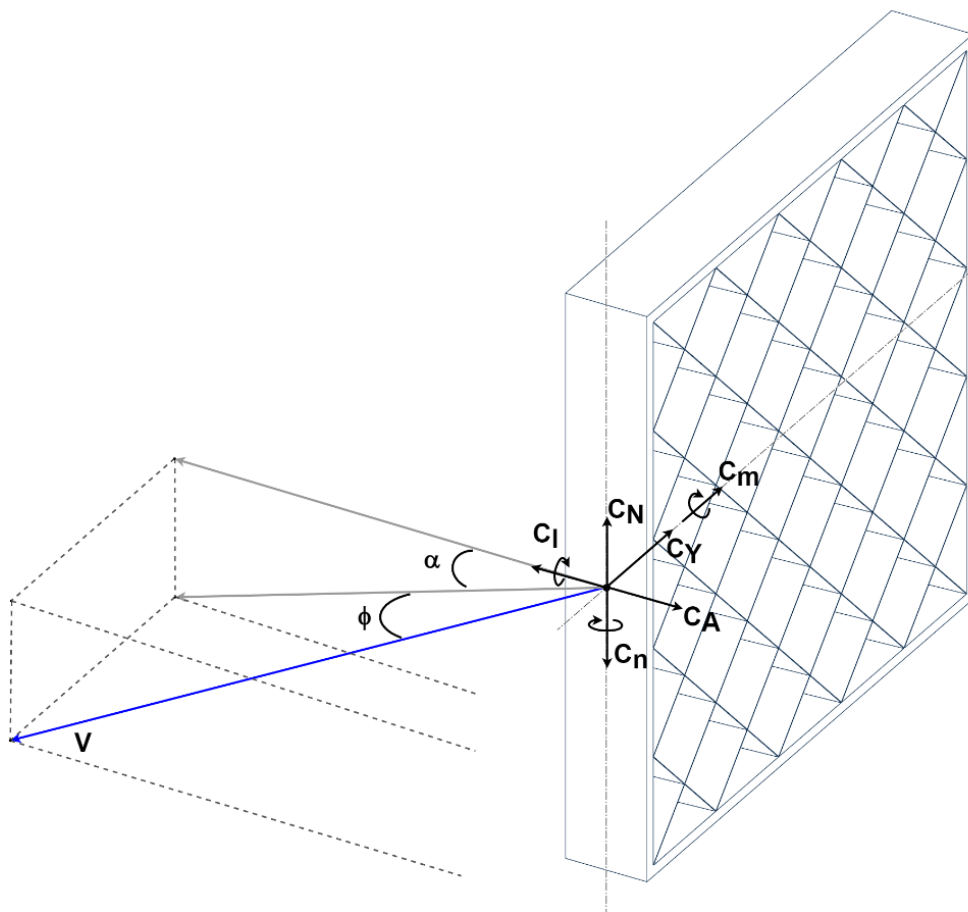
Figure 3.18. Sign Convention of Aerodynamic Coefficients in Grid Fin

Table 3.3 Non-Dimensionalization Parameters

Aerodynamic Coefficient	Non-Dimensionalization Parameter
C_A	$q_\infty \cdot S_{ref}$
C_Y	$q_\infty \cdot S_{ref}$
C_N	$q_\infty \cdot S_{ref}$
C_l	$q_\infty \cdot S_{ref} \cdot l_{ref}$
C_m	$q_\infty \cdot S_{ref} \cdot l_{ref}$
C_n	$q_\infty \cdot S_{ref} \cdot l_{ref}$

In CFD analyses of grid fin, solution mostly converged around 3500 iterations with the maximum CFL number of 12. Residuals are dropped to at least around 10^{-4} and a sample residual plot is given in Figure 3.19.
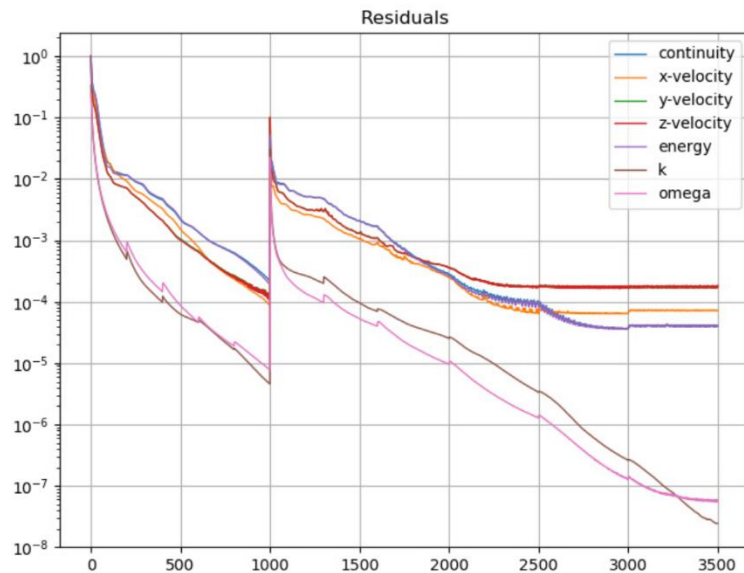
Figure 3.19. A Sample Residual History of Aerodynamic Coefficients in a Grid Fin CFD Analysis
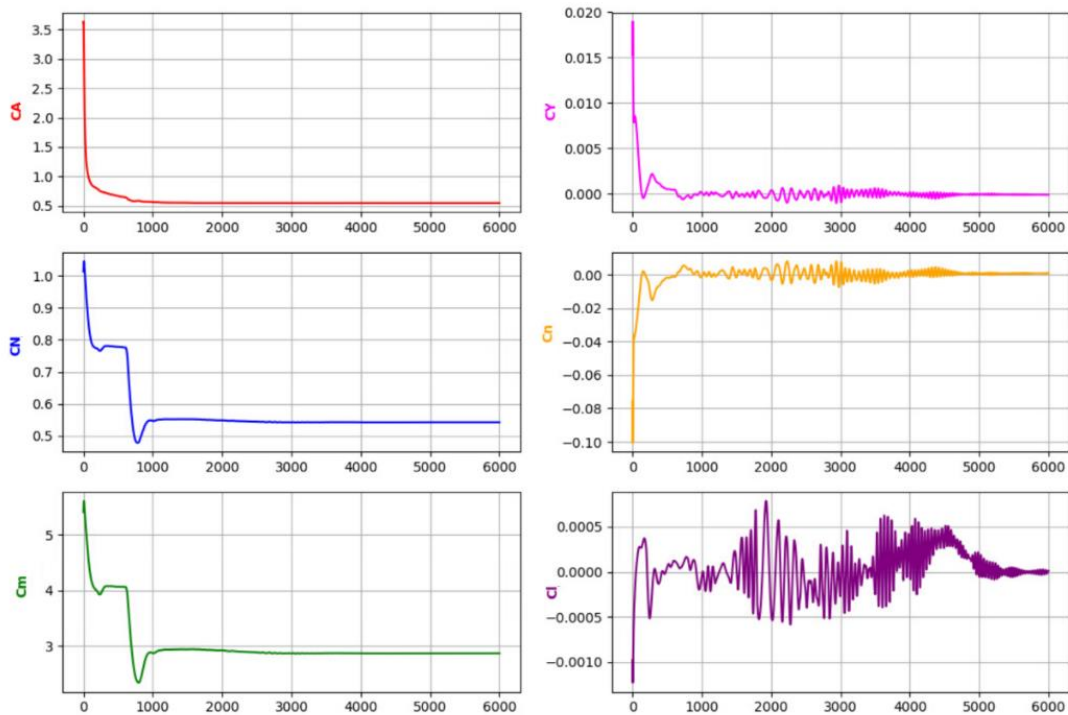
Figure 3.20. A Sample Convergence Plot of Aerodynamic Coefficients in a Grid Fin CFD Analysis

3.3 Design of Experiments Methodology

Design of Experiments (DOE) is a mathematical methodology for designing, performing, evaluating, and interpreting experiments. The purpose of DOE techniques is to gather as much information as possible from a small number of laboratory or computer experiments. It's a branch of applied statistics that's used to conduct scientific investigations of a system, process, or product in which input variables are changed to see how they affect the measured variable's responses. To put it another way, it's utilized to discover cause-and-effect relationships.

3.3.1   Parameter Screening

In the parameter screening, the responses, or aerodynamic coefficients in this case, are compared by looking at the p-values that are less than 0.1 and explained, respectively. The p-value measures statistical significance of a factor, with a lower p-value indicating a higher level of significance.

The parameters affecting the investigated aerodynamic coefficient are ordered in the JMP software according to their importance. There are different indicators in the screening report which is created by JMP software. Term shows the name of the factor. Contrast shows the estimate for the factor. This number is the same as the regression parameter estimate. There is a bar chart appears in this report and it shows the Lenth t-ratios that indicate a value that is significant at 0.1 level. Lenth t-ratios are computed by dividing the contrast by Lenth Pseudo Standard Error (PSE). PSE constructs an estimate of the residual standard error using inactive effects. The reference distribution of these t-ratios under the null hypothesis is not computationally tractable in Lenth t-ratio method. Therefore, it is obtained by Monte Carlo simulations in JMP software. Individual p-values are analogous to the standard p-values for a linear model. Small individual-p values indicate a significant effect. Simultaneous p-values shows a multiple-comparison adjusted p-value in these reports [51].

3.3.2   Constructing Designs

Several design construction methods are exist in platforms like JMP commercial statistical software. Factorial, fractional factorial, and space-filling designs, are being considered for the DOE analysis. Factorial designs requires huge amount of runs and is not practical unless the experiments are cheap. Fractional factorial designs are a reduced version of factorial designs. However, fractional factorial designs deprived from good quadratic impact estimation and can only be used for simple definitive purposes [51]. Space-filling designs, such as Latin Hypercube Sampling (LHS), are

effective for issues that require samples to be placed across the whole design space. Due to the changing homogeneity of the sample sets and the correlation among the sample data, space-filling designs are ill suited for response surface techniques [47]. In addition, methods such as Central Composite Design (CCD) and Box-Behnken (BB) designs are available design methodologies mostly used for response surface generation purposes. For the factors of design space, these methods use a center point placement strategy with a fractional factorial design.

In this thesis, BB design of experiment methodology is applied. In BB designs, upper and lower limits of factors are used for corner points and their mean values are used for middle points. This methodology is illustrated in Figure 3.21 for only three factors. Most of the time, in this design approach -1, 0, and +1 is used for the representation of lower, mean and upper values, respectively. After determination of the design points, lower, mean and upper values are normalized with actual parameter upper and lower values to create a physically meaningful design set.
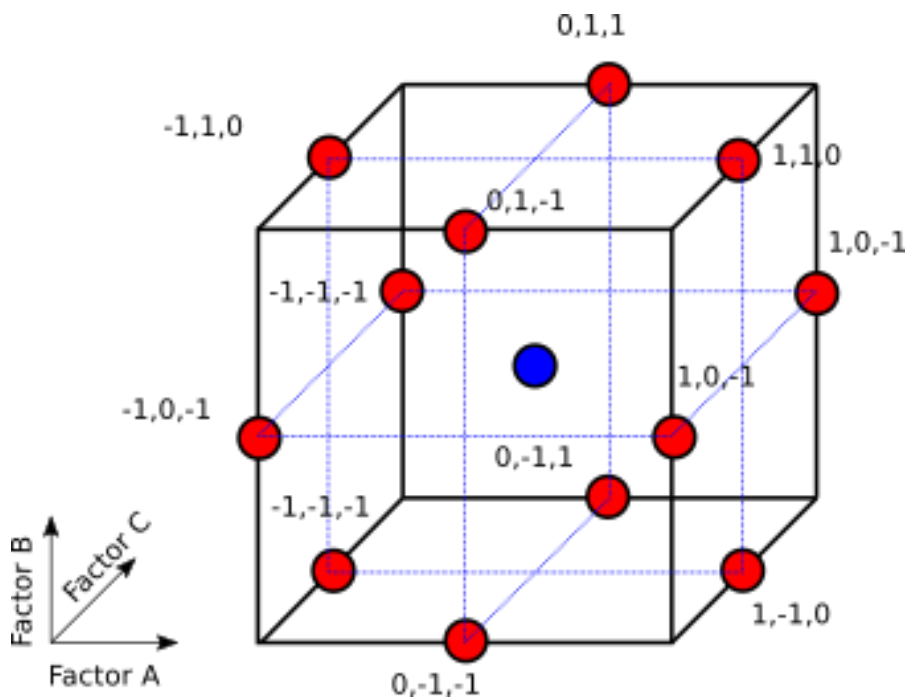
Figure 3.21. Box-Behnken Distibution of Design of Experiments

Considering the included parameters, the BB experiments are determined using commercial program JMP. In the software, upper, medium and lower points are represented with +, 0, and -, respectively. The upper and lower limits of grid fin parameters used in this thesis is presented in Table 3.4.

Table 3.4 Lower, Middle, and Upper Values of Parameters in Box-Behnken Design

Pattern	c / g	s / g	w / g	g	t_w / g	t_f / t_w
Min (−)	0.25	2	2	10	0.01	1.0
Base (0)	0.75	5	5	20	0.04	2.5
Max (+)	1.25	8	8	30	0.07	4.0

The designs are given in Table 3.5 and for each design point, parameter values are determined according to the pattern of that design. In total, 54 designs are evaluated. Designs 2, 16, 33, 37, 46 and 53 are the center points, therefore they are basically representing the same geometry and an asterisk appears next to the design number in Table 3.5. When CFD analyses are prepared, only Design-2 is considered and copied for the other marked designs for convenience.

Table 3.5 Box-Behnken Designs

Design ID	Pattern	c / g	s / g	w / g	g	t_w / g	t_f / t_w
1	−00−+0	0.25	5	5	10	0.07	2.5
2*	0	0.75	5	5	20	0.04	2.5
3	−00+−0	0.25	5	5	30	0.01	2.5
4	00+−0−	0.75	5	8	10	0.04	1
5	−−0+00	0.25	2	5	30	0.04	2.5
6	0++0−0	0.75	8	8	20	0.01	2.5
7	+0−00−	1.25	5	2	20	0.04	1
8	0−00+−	0.75	2	5	20	0.07	1
9	0+−0+0	0.75	8	2	20	0.07	2.5
10	0−00−−	0.75	2	5	20	0.01	1
11	+−0+00	1.25	2	5	30	0.04	2.5
12	0−00++	0.75	2	5	20	0.07	4
13	−0−00+	0.25	5	2	20	0.04	4
14	0+00−−	0.75	8	5	20	0.01	1
15	+00−−0	1.25	5	5	10	0.01	2.5
16*	0	0.75	5	5	20	0.04	2.5
17	+00−+0	1.25	5	5	10	0.07	2.5
18	00−−0−	0.75	5	2	10	0.04	1
19	+0−00+	1.25	5	2	20	0.04	4
20	+0+00+	1.25	5	8	20	0.04	4
21	+0+00−	1.25	5	8	20	0.04	1
22	−+0−00	0.25	8	5	10	0.04	2.5
23	−0−00−	0.25	5	2	20	0.04	1
24	+00+−0	1.25	5	5	30	0.01	2.5
25	0−−0−0	0.75	2	2	20	0.01	2.5
26	00−+0−	0.75	5	2	30	0.04	1

Table 3.5 Box-Behnken Designs (Continued)

27[*]	0	1.25	8	5	30	0.04	2.5
28	0−+0−0	0.75	2	8	20	0.01	2.5
29	−0+00−	0.25	5	8	20	0.04	1
30	0+00++	0.75	8	5	20	0.07	4
31	−0+00+	0.25	5	8	20	0.04	4
32	−00−−0	0.25	5	5	10	0.01	2.5
33[*]	0	0.75	5	5	20	0.04	2.5
34	0++0+0	0.75	8	8	20	0.07	2.5
35	0−00−+	0.75	2	5	20	0.01	4
36	00−+0+	0.75	5	2	30	0.04	4
37[*]	0	0.75	5	5	20	0.04	2.5
38	−−0−00	0.25	2	5	10	0.04	2.5
39	0−+0+0	0.75	2	8	20	0.07	2.5
40	0	1.25	5	5	30	0.07	2.5
41	0−−0+0	0.75	2	2	20	0.07	2.5
42	00+−0+	0.75	5	8	10	0.04	4
43	−+0+00	0.25	8	5	30	0.04	2.5
44	00−−0+	0.75	5	2	10	0.04	4
45	00++0−	0.75	5	8	30	0.04	1
46[*]	0	0.75	5	5	20	0.04	2.5
47	++0−00	1.25	8	5	10	0.04	2.5
48	00++0+	0.75	5	8	30	0.04	4
49	0+00−+	0.75	8	5	20	0.01	4
50	0+00+−	0.75	8	5	20	0.07	1
51	−00++0	0.25	5	5	30	0.07	2.5
52	0+−0−0	0.75	8	2	20	0.01	2.5
53[*]	0	0.75	5	5	20	0.04	2.5
54	+−0−00	1.25	2	5	10	0.04	2.5

3.4   Response Surface Methodology

Modeling a response surface, also known as surrogate, can be considered as determining a continuous function of design variables from a limited amount of available data. In this thesis, the surrogate models are created via importing the results to HEEDS software. In this process, the Radial Basis Function (RBF) is used for the surrogate model generation. The models are created providing 54 design points to the surrogate generation tool. Model creation is almost instantly occurs, and the results include the actual design point values, model prediction values, and cross-validation findings.

Radial basis functions have been developed for the interpolation of scattered multivariate data. In Equation 3.2 function f is approximated by function f' and ε is called as the error in this approximation. The approximation function is shown in Equation 3.3. The method uses linear combinations of N radially symmetric functions, based on Euclidean distance or other such metric to approximate response function given in equation. In this equation, w represents the linear combination coefficients and $h(x)$ is the radial basis functions.

$$f(x) = f'(x) + \varepsilon \tag{3.2}$$

$$f'(x) = w_0 + \sum_{i=1}^{N} w_i \, h_i(x) \tag{3.3}$$

Response surfaces should be validated since the performance of these functions highly depends on the number of data provided to create them. Depending on the nonlinearity of the responses investigated, the number of design points created via BB design approach may not be sufficient. For that purpose, Cross Validation (CV) approach is adopted in this thesis. Cross validation is a process that used for the test of the validity of the surrogate models. It uses the available data used for constructing the surrogates. In general, the data is divided into k subsets of approximately equal size. A surrogate model is created k times, each time leaving out one of the subsets from training and using the omitted subset to estimate errors. This process is called

k-fold cross-validation. If k equals the size of the training data, the subset became a single data, and this approach is called leave-one-out cross validation [47]. Validity of the models are tested through leave-one-out cross-validation results in this thesis. To measure the error in this process, Predicted Residual Sum of Squares (PRESS) is used which is formulated in Equation 3.4 [52].

$$PRESS = \sum_{i=1}^{N_{data}} \left(f(x_i) - f_s(x_i) \right)^2 \qquad (3.4)$$

In this thesis, to further testing the validity of the surrogates, a different set of designs are analyzed with CFD. These design points are created as having intermediate values to observe the response surface behavior in the intermediate design points. Validation design points are determined using LHS method.

CHAPTER 4

RESULTS AND DISCUSSION

In this chapter, the CFD results are examined in three parts. In the first part, DOE results are used for investigating response screening for grid fins using JMP statistical analysis software. In the second part, a response surface is created for each aerodynamic coefficient using HEEDS commercial software. Cross-validation and validation procedure and results are presented in this section. In the last part, flow field is investigated and the behavior of the flow around grid fin is visualized via Mach number and static pressure contours.

4.1   Parameter Sensitivity Analysis

In the JMP software, factors are created using BB method for further investigation. After CFD results are obtained, they are put in the JMP software to investigate which parameters influence which coefficient using statistical evaluation methods. This process is called sensitivity analysis or parameter screening process in the literature. It is a useful method which provides an insight to grid fin aerodynamics in this thesis. These results may be considered for further studies related to grid fins. For instance, some parameters can be excluded for aerodynamic optimization purposes to speed up the heavy optimization procedure. It may also contribute to the prediction methods designed for grid fins as well. The details of parameter screening methodology is explained in Section 3.3.1. The screening process are performed for each aerodynamic coefficient individually, hence, the values are not comparable. The angle of attack and roll angle is also included for this procedure to observe their effects on aerodynamic coefficients as well. Also, since the parameters are defined as the ratio of the gap (g), the gap parameter is anticipated as important for all aerodynamic coefficients.

4.1.1   Axial Force Coefficient

The parameter sensitivity analysis results for the axial force coefficient is given in Figure 4.1. These results show that all parameters have influence on axial force coefficient. Web thickness, frame thickness, span and width have stronger effects on axial force coefficient since they shape the grid fin in the perpendicular direction to the axial force coefficient direction. Gap has the most influence because changing gap parameter affect all other parameters and also as gap is changed, the exposed surface area is also changed accordingly. However, chord-to-gap ratio (c/g) has smaller effect on the axial force coefficient compared to other shape parameters because the changes in the chord are in the same direction of the axial force. Also, angle of attack and roll angle has the smallest effect in all of the parameters.

Term	Contrast		Lenth t-Ratio	Individual p-Value	Simultaneous p-Value
gap	0.101421		792.27	<.0001*	<.0001*
t_web_gap	0.084948		663.59	<.0001*	<.0001*
t_frame_t_web	0.051445		401.87	<.0001*	<.0001*
Span_gap	0.043505		339.85	<.0001*	<.0001*
Width_gap	0.040762		318.42	<.0001*	<.0001*
Chord_gap	-0.004481		-35.00	<.0001*	<.0001*
AoA	-0.002656		-20.75	<.0001*	<.0001*
Phi	0.000380		2.97	0.0025*	0.7077

Figure 4.1. Response Screening for Axial Force Coefficient (C_A)

4.1.2   Normal Force Coefficient

Results corresponding to the normal force coefficient are shown in Figure 4.2. Results show that the shape parameters except the frame thickness related parameter have effect on the normal force coefficient. The frame thickness parameter is expected to have no effect. However, the web thickness is considered as important parameter since increasing web thickness too much narrows down the space inside the grid fin cell and this may lead to normal force degradation due to flow chocking. Gap, chord, span and width parameters have positive influence on normal force coefficient and they all change the exposed area in the normal force direction. In other words, as chord, span, width or gap is increased, grid fin has more exposed

surface area and hence more normal force coefficient value. The angle of attack has the most influence as expected. Also, the roll angle has negative effect on normal force since basically, it reduces the velocity magnitude in the normal force direction.

Term	Contrast		Lenth t-Ratio	Individual p-Value	Simultaneous p-Value
AoA	0.157885		185.67	<.0001*	<.0001*
gap	0.125645		147.76	<.0001*	<.0001*
Span_gap	0.084762		99.68	<.0001*	<.0001*
Width_gap	0.077730		91.41	<.0001*	<.0001*
Chord_gap	0.066245		77.91	<.0001*	<.0001*
Phi	-0.035611		-41.88	<.0001*	<.0001*
t_web_gap	-0.004478		-5.27	<.0001*	0.0004*
t_frame_t_web	0.000484		0.57	0.5562	1.0000

Figure 4.2. Response Screening for Normal Force Coefficient (C_N)

4.1.3 Side Force Coefficient

Results corresponding to the side force coefficient are shown in Figure 4.3. It shows that the side force coefficient is mostly affected by the roll angle since the grid fin does not produce side force in zero roll flight conditions. Results show negative effect values because of the sign convention of the side force. In other words, positive roll angle creates negative side force. Similarly, the angle of attack affects the side force if there is non-zero roll angle since it creates a velocity component in the direction of the side force coefficient. The web and frame thickness have no influence on the side force coefficient. Other parameters affecting the side force coefficient are similar to the normal force coefficient. However, the width parameter has more affect than the span parameter on C_Y. It should be noted that, this force is balanced by the missile body when grid fin is integrated to it.

Term	Contrast		Lenth t-Ratio	Individual p-Value	Simultaneous p-Value
Phi	-0.089776		-59.61	<.0001*	<.0001*
AoA	-0.066084		-43.88	<.0001*	<.0001*
gap	-0.052506		-34.86	<.0001*	<.0001*
Width_gap	-0.035980		-23.89	<.0001*	<.0001*
Span_gap	-0.032067		-21.29	<.0001*	<.0001*
Chord_gap	-0.027882		-18.51	<.0001*	<.0001*
t_web_gap	0.001605		1.07	0.2878	1.0000
t_frame_t_web	-0.000398		-0.26	0.7819	1.0000

Figure 4.3. Response Screening for Side Force Coefficient (C_Y)

4.1.4 Roll Moment Coefficient

Results corresponding to the roll moment coefficient is shown in Figure 4.4. This coefficient is corresponding to the bending moment coefficient if the grid fin is placed on a missile body. Results show that the roll moment coefficient depends on the parameters similarly as in the normal force coefficient. It is expected because the roll moment is coupled with the normal force. In other words, the roll moment is resulted from the normal force coefficient. Hence, the inferred information about the normal force coefficient earlier is valid here too.

Term	Contrast		Lenth t-Ratio	Individual p-Value	Simultaneous p-Value
gap	-0.092774		-111.21	<.0001*	<.0001*
AoA	-0.088313		-105.86	<.0001*	<.0001*
Span_gap	-0.077709		-93.15	<.0001*	<.0001*
Width_gap	-0.040626		-48.70	<.0001*	<.0001*
Chord_gap	-0.040287		-48.29	<.0001*	<.0001*
Phi	0.019844		23.79	<.0001*	<.0001*
t_frame_t_web	-0.001993		-2.39	0.0192*	0.9939
t_web_gap	0.000530		0.63	0.5227	1.0000

Figure 4.4. Response Screening for Roll Moment Coefficient (C_l)

4.1.5 Pitch Moment Coefficient

The pitch moment coefficient is related with hinge moment coefficient if the grid fin is mounted on a missile body. It is created by the normal force and axial force coefficient together. It depends on all of the parameters because the hinge moment coefficient is susceptible to any change in the axial and normal forces. Also, any change in the point of application of these forces influences the pitching moment enourmously. The parameter screening result is shown in Figure 4.5.

Term	Contrast		Lenth t-Ratio	Individual p-Value	Simultaneous p-Value
gap	0.004616		56.42	<.0001*	<.0001*
AoA	0.004278		52.29	<.0001*	<.0001*
Chord_gap	0.004057		49.59	<.0001*	<.0001*
t_web_gap	0.002553		31.21	<.0001*	<.0001*
Span_gap	0.001636		20.00	<.0001*	<.0001*
Width_gap	0.001153		14.10	<.0001*	<.0001*
t_frame_t_web	0.001151		14.07	<.0001*	<.0001*
Phi	-0.000979		-11.96	<.0001*	<.0001*

Figure 4.5. Response Screening for Pitch Moment Coefficient (C_m)

4.1.6   Yaw Moment Coefficient

The yaw moment coefficient screening results are presented in Figure 4.6. The yaw moment coefficient is coupled with the axial force coefficient. Hence it depends on the parameters that the axial force coefficient is influenced by. The results shows that the roll angle has weak influence on the yaw moment coefficient. It should be noted that, this coefficient is important for the structural issues when grid fin is integrated to the missile body.

Term	Contrast		Lenth t-Ratio	Individual p-Value	Simultaneous p-Value
gap	0.053234		40.47	<.0001*	<.0001*
Span_gap	0.038251		29.08	<.0001*	<.0001*
t_web_gap	0.033483		25.45	<.0001*	<.0001*
AoA	0.029484		22.41	<.0001*	<.0001*
t_frame_t_web	0.019690		14.97	<.0001*	<.0001*
Width_gap	0.014268		10.85	<.0001*	<.0001*
Chord_gap	-0.003539		-2.69	0.0073*	0.9233
Phi	-0.001962		-1.49	0.1364	1.0000

Figure 4.6. Response Screening for Yaw Moment Coefficient (C_n)

4.2   Response Surface Generation

In this section, using the DOE results, response surfaces for each aerodynamic coefficient are created using the HEEDS MDO commercial software. This section covers the cross-validation results extracted from the HEEDS software and a validation of the response surfaces using a different test data set to show the accuracy of the response surfaces created.

Since 8-parameter repsonse surface is impossible to illustrate, for each aerodynamic coefficient response surfaces are plotted as 3-D graphs. In these graphs, two most important parameters are used for x and y axis and aerodynamic coefficient is placed in the z-axis while other parameters are kept at baseline (center) point. These graphs are valuable for visualization of response surfaces and the behavior of the corresponding aerodynamic coefficient.
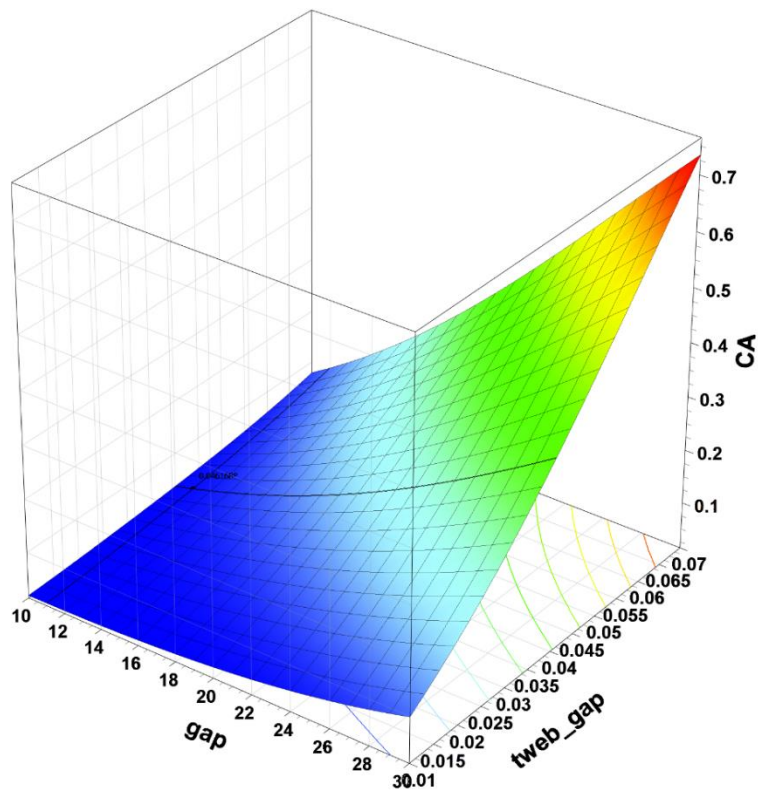
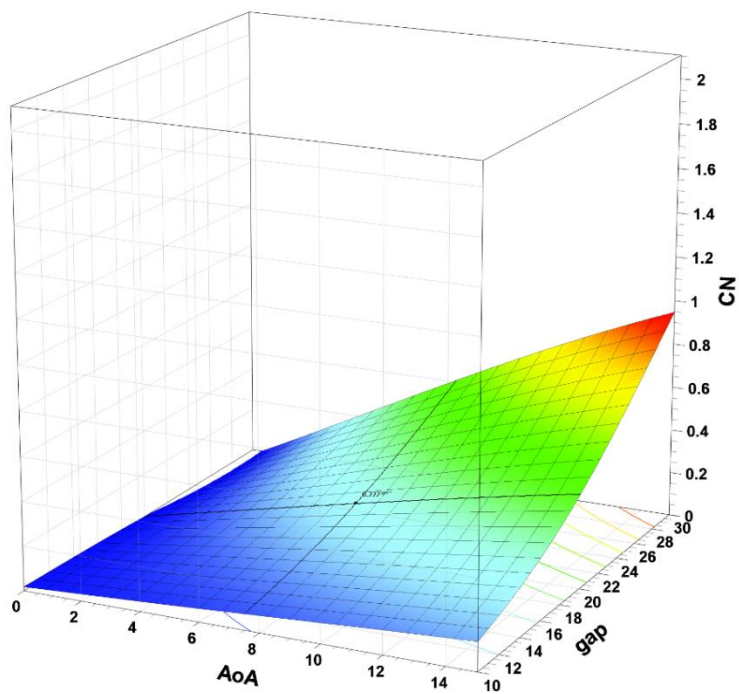Figure 4.7. Response Surface for Axial Force Coefficient (C_A) using g and t_w/g

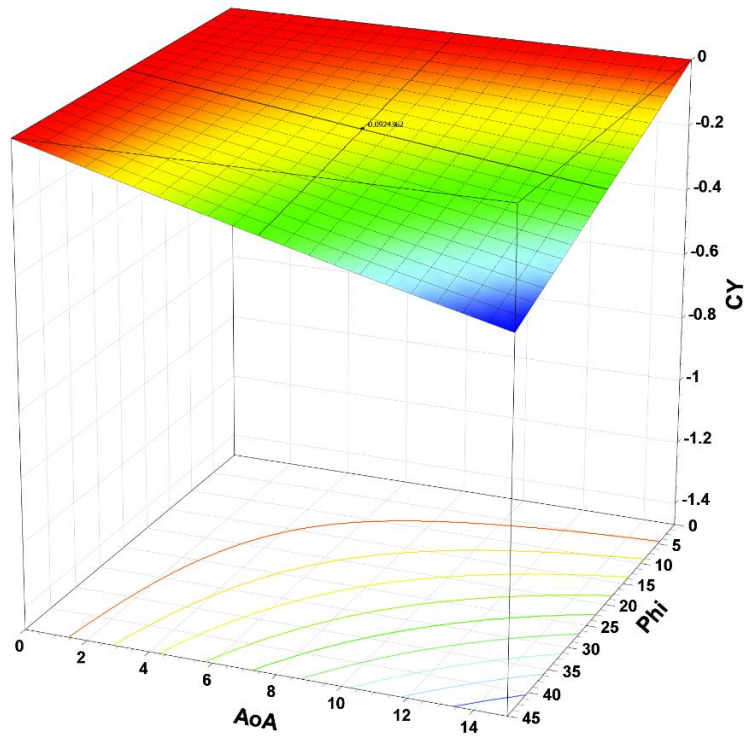Figure 4.8. Response Surface for Normal Force Coefficient (C_N) using g and α

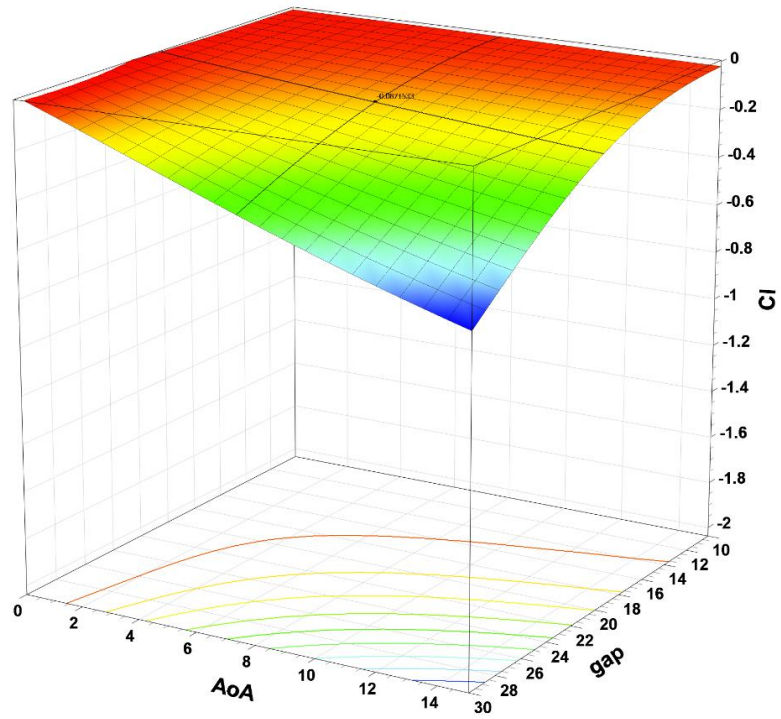Figure 4.9. Response Surface for Side Force Coefficient (C_Y) using ϕ and α

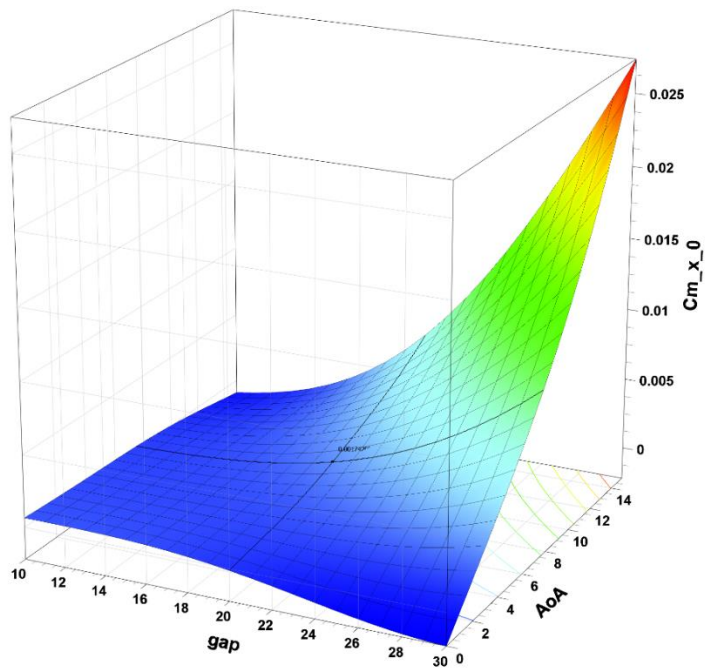Figure 4.10. Response Surface for Roll Moment Coefficient (C_l) using g and α

Figure 4.11. Response Surface for Pitch Moment Coefficient (C_m) using g and α
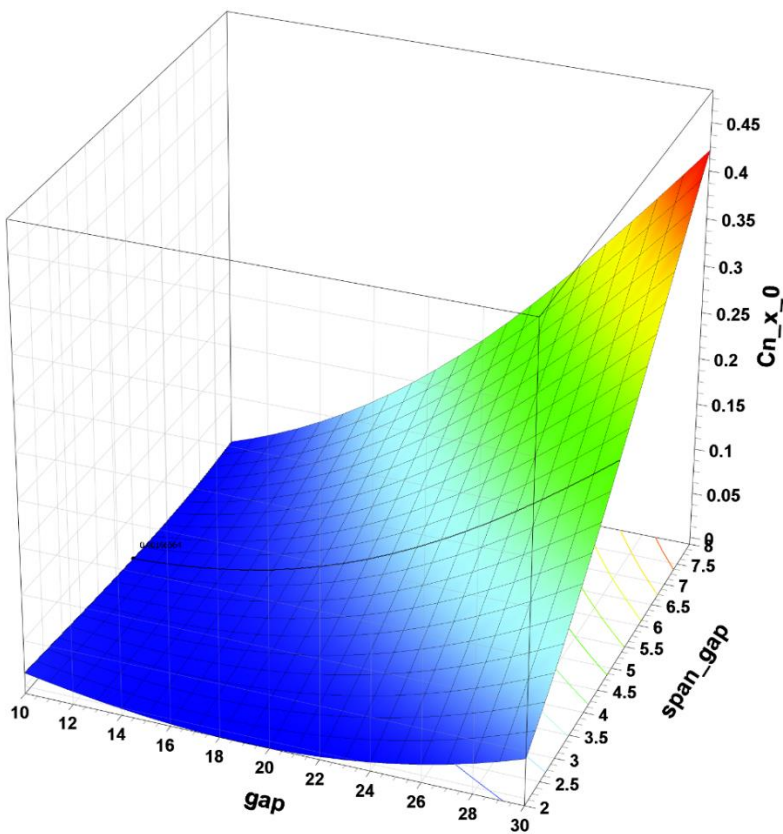

Figure 4.12. Response Surface for Yaw Moment Coefficient (C_n) using g and s/g

4.2.1　Leave-One-Out Cross-Validation

The cross-validation process is explained in section 3.4 Response Surface Methodology. CV results presented in Table 4.1 and the residuals are very small. It indicates perfect fit, and the actual-vs-predicted results are supporting this statement. The corresponding graphs for each aerodynamic coefficient are shown in Figure 4.13 - Figure 4.18. It should be noted that on some coefficients data are concentrated into some regions. It gives an idea about what is the order of magnitude of the aerodynamic coefficients in this thesis.

Table 4.1 Cross-Validation Residuals

| Performance Output	Method	Cross-Validation Residual
C_A	Radial Basis Function with Cubic Interpolation	0.00379
C_N	Radial Basis Function with Cubic Interpolation	0.0228
C_Y	Radial Basis Function with Cubic Interpolation	0.0250
C_l	Radial Basis Function with Cubic Interpolation	0.0209
$C_{m\_x\_0}$	Radial Basis Function with Cubic Interpolation	0.0019
$C_{n\_x\_0}$	Radial Basis Function with Cubic Interpolation	0.0034
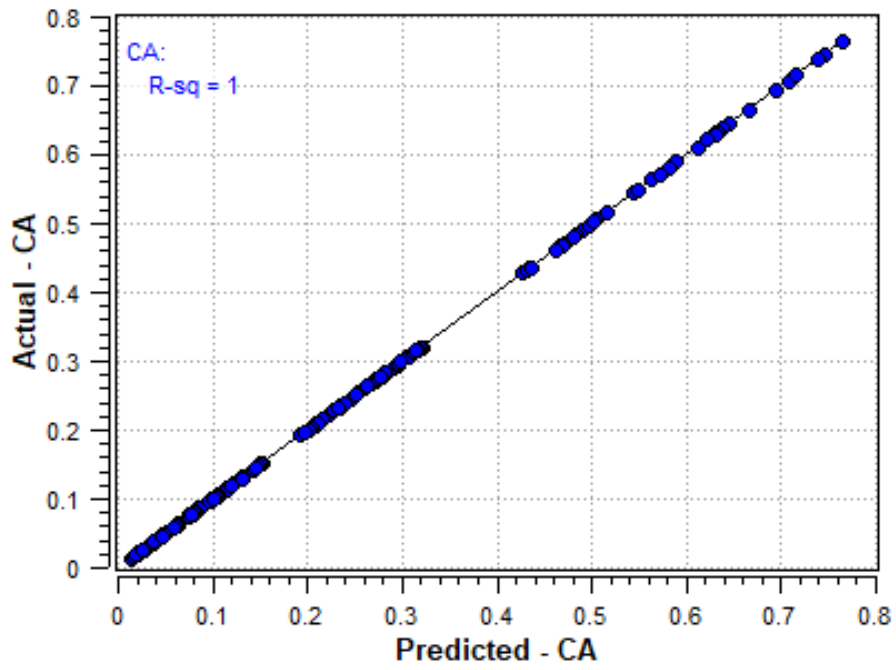
Figure 4.13. Surrogate Model for C_A Output
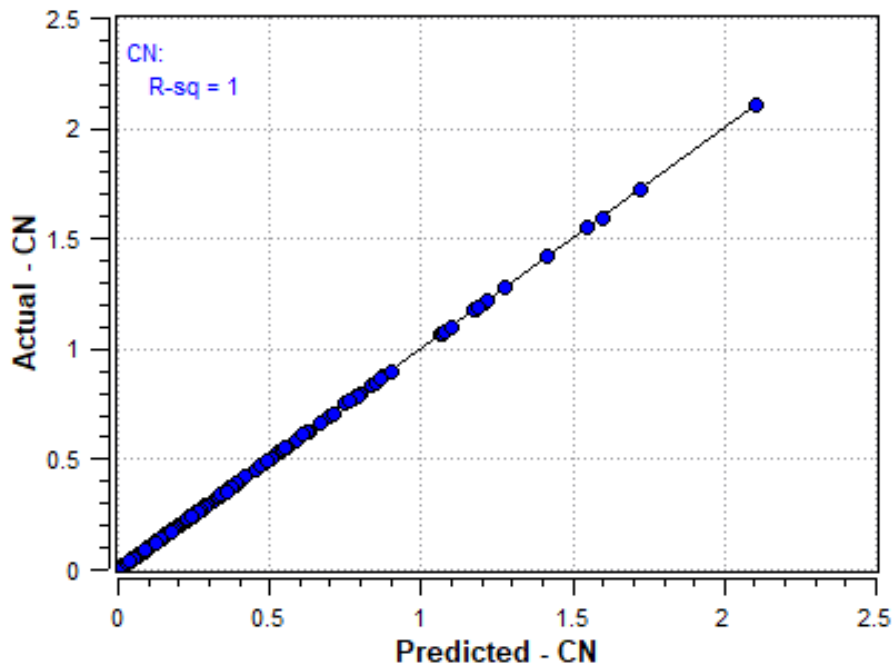

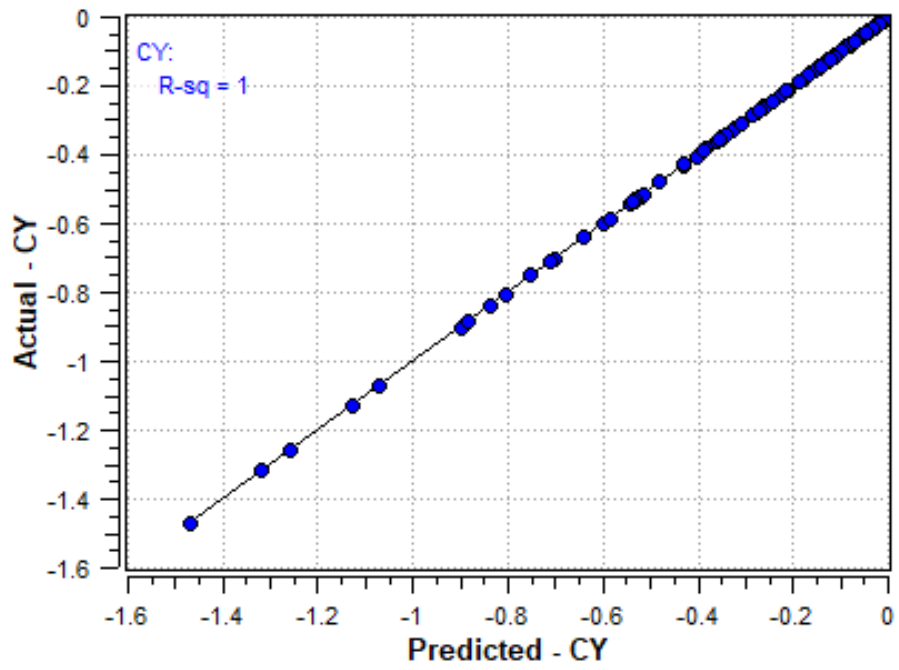Figure 4.14. Surrogate Model for C_N Output

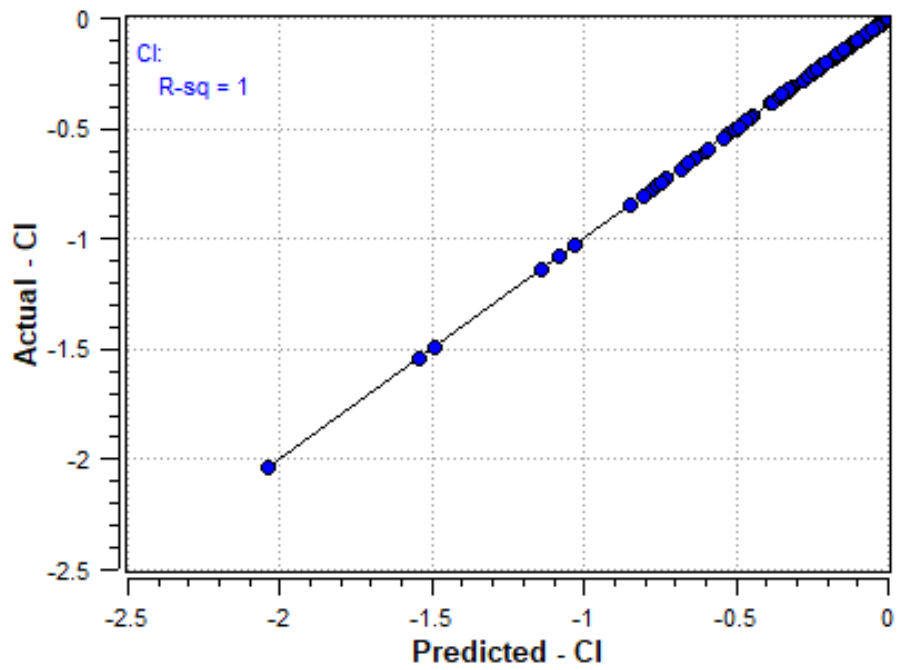Figure 4.15. Surrogate Model for C_Y Output

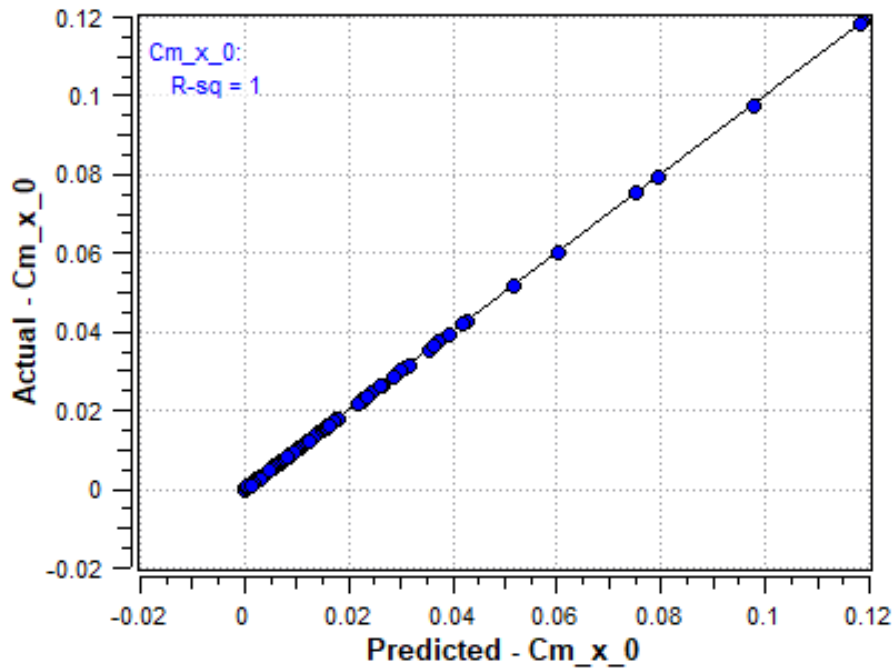Figure 4.16. Surrogate Model for C_l Output
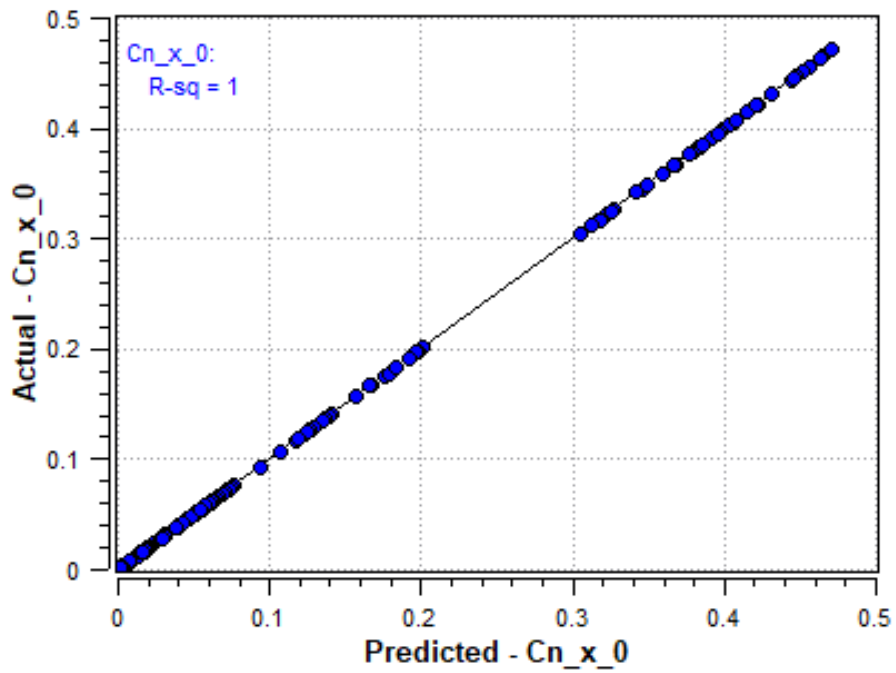
Figure 4.17. Surrogate Model for C_m Output

Figure 4.18. Surrogate Model for C_n Output

4.2.2   Validation

Although the cross-validation results showed good agreements for all aerodynamic coefficients, to further validate these response surfaces, another set of designs which are not included in the response surface generation process is used. For this purpose, 10 different design points are chosen using LHS meyod and parameters of these designs are presented in Table 4.2. For each design, 8 CFD analyses are performed which include angle of attack ranging from 0 to 15 degrees and roll angles of 0 and 45 degrees.

Table 4.2 Test Data Set

Design ID	gap	c/g	s/g	w/g	t_w/g	t_f/t_w
1	26	1.05	7	5	0.02	2.5
2	18	0.9	8	4	0.03	3.5
3	12	1.1	2	3	0.05	3
4	22	0.95	4	4	0.04	2
5	16	0.75	5	8	0.05	2.5
6	26	0.85	6	7	0.06	1.5
7	30	1.15	6	5	0.01	3.5
8	10	0.9	4	3	0.06	4
9	24	1.25	4	7	0.04	2
10	16	1.05	3	6	0.02	1

For each design in the test data, the aerodynamic coefficients are estimated using the response surfaces and they are plotted in actual-predicted graphs. These graphs are presented in figures. In these plots, the diagonal dashed line shows the perfect fit. Root Mean Square Error (RMSE) and Normalized Root Mean Square Error (NRMSE) values are also presented in these graphs.

$$RMSE = \sqrt{\sum_{i=1}^{N} \frac{\left(y_{i,test} - y_{i,RSM}\right)^2}{N}} \qquad (4.1)$$

$$NRMSE = \frac{\sqrt{\sum_{i=1}^{N} \frac{\left(y_{i,test} - y_{i,RSM}\right)^2}{N}}}{max(y_{test}) - min(y_{test})} \qquad (4.2)$$
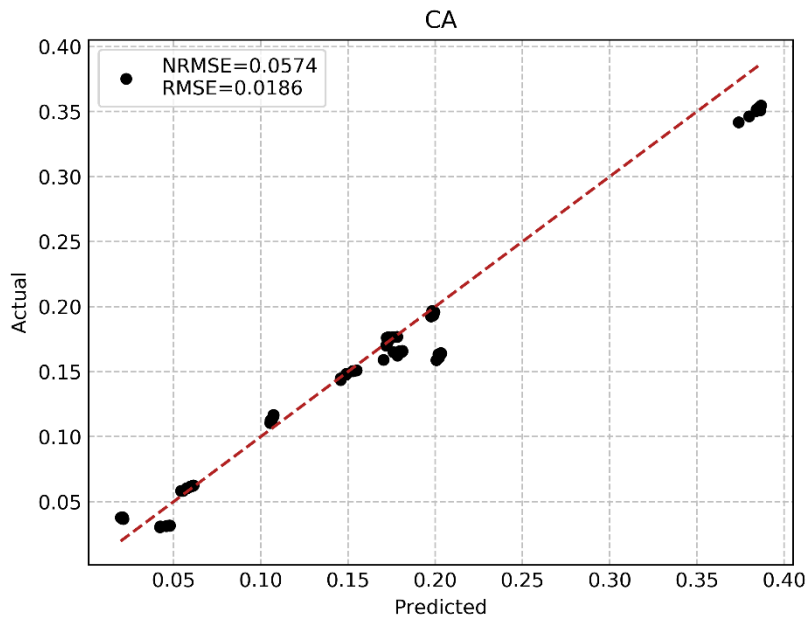

Figure 4.19. Validation Results for C_A Surrogate

In the axial force coefficient, distinctive data values are observed. Since each design having different axial force coefficient values and this coefficient is almost independent from the angle of attack and the roll angle, the results of each design concentrated on a specific value. The normal force and side force coefficients are distributed more uniformly than the axial force coefficient. The surrogates related to force coefficients have good agreement with the validation CFD data.
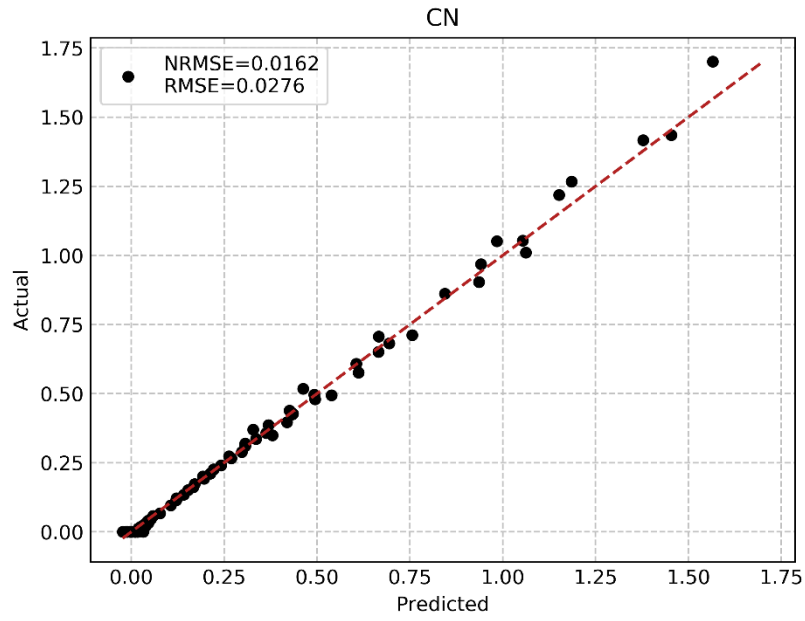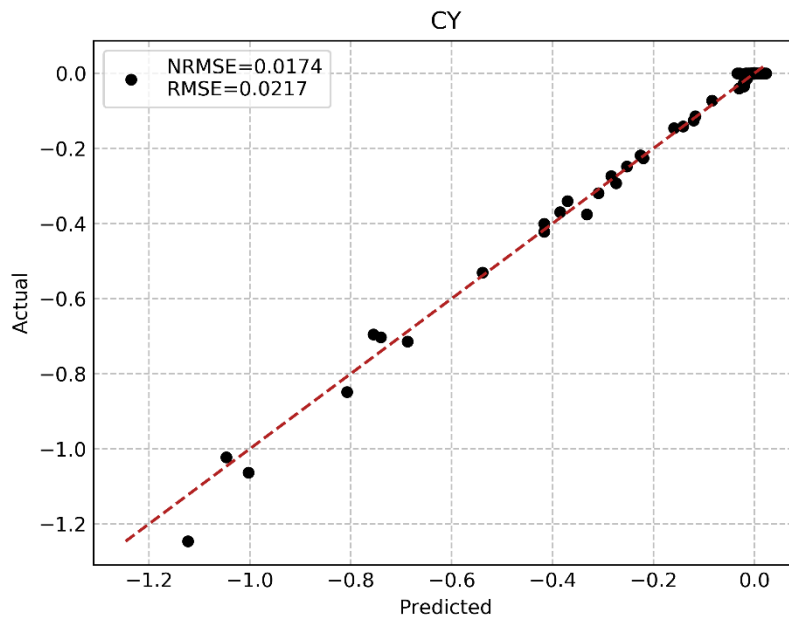
Figure 4.20. Validation Results for C_N Surrogate

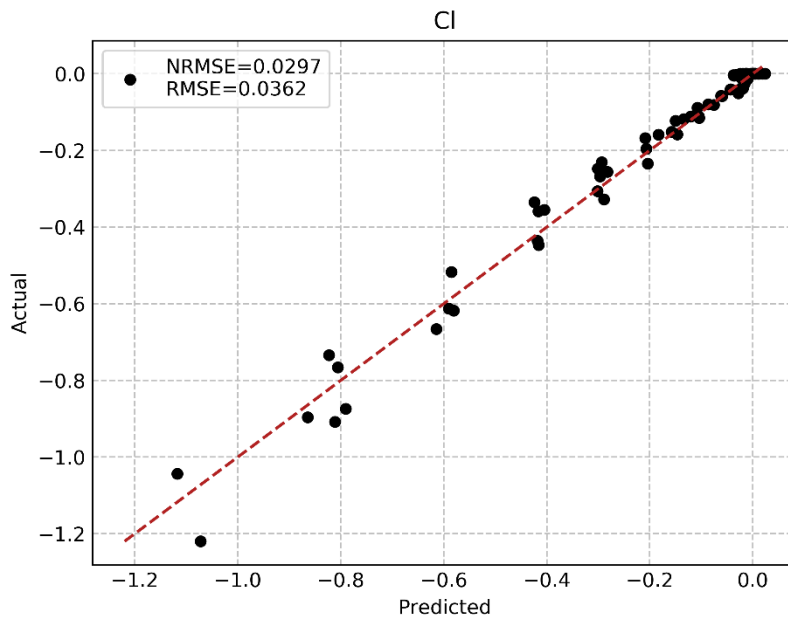Figure 4.21. Validation Results for C_Y Surrogate

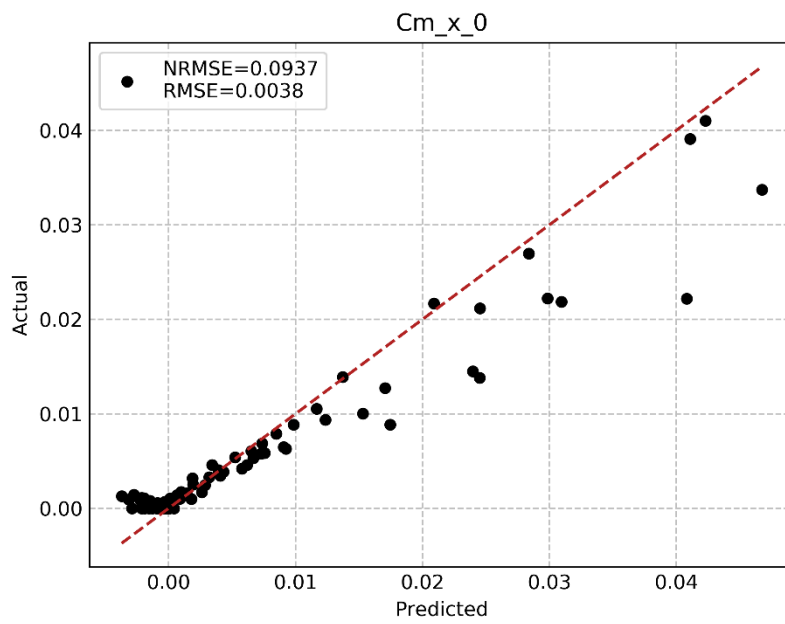Figure 4.22. Validation Results for C_l Surrogate

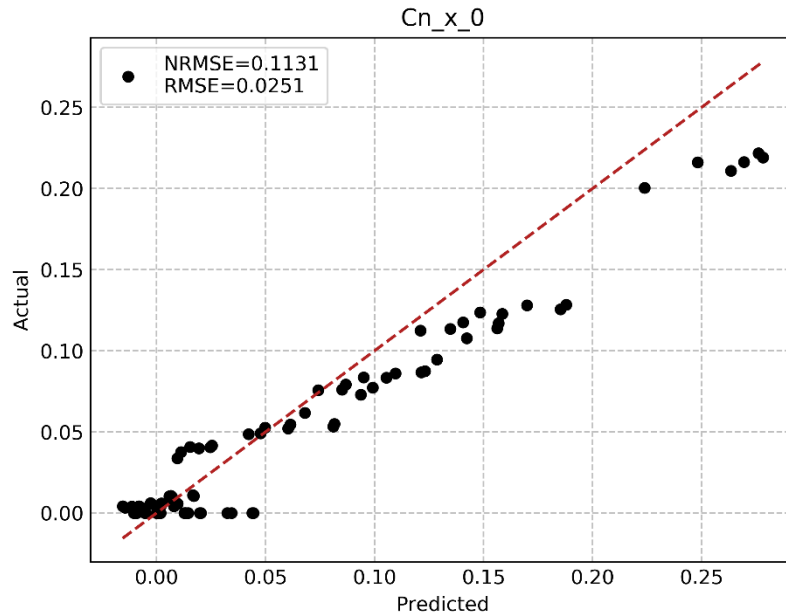Figure 4.23. Validation Results for C_m Surrogate

Figure 4.24. Validation Results for C_n Surrogate

The roll moment coefficients are distributed similar to the normal and side force coefficients. It is expected since the roll moment coefficient is coupled with the normal force coefficient. Therefore, a good agreement is achieved for the roll moment coefficient as well. The pitching moment coefficient is extremely difficult to model because it depends on both axial force and normal force coefficients. Moreover, it is susceptible to any changes in the center of pressure and due to complex flow structure inside the grid cells, the location of center of pressure may be misplaced due to numerical errors in CFD calculations. High deviations from the ideal actual-predicted line are observed for the pitch moment coefficient validation results. However, general behavior is modelled through the response surface, and it is considered to be useful in optimization processes since the values of pitch moment (hinge moment) coefficients are very small in grid fin and it is not necessary to further optimize this coefficient. The yaw moment coefficient has moderate agreement with CFD results. It is coupled with the axial force coefficient and therefore some discrepancies are observed here as well. The general behavior is estimated, and the response surfaces are valid for optimization purposes.

4.3   Flow Field Investigation

In this section, the DOE results are investigated in a different way. As stated in Section 1.1, grid fins have superior lifting characteristics, however, a poorly designed grid fin may not show this performance. In order to assess this issue, a post process is applied to DOE results to detect designs which have normal force performance loss and to determine what common features these designs have.

In a well-designed grid fin, the slope of the normal force coefficient is expected to be independent of angle of attack because decrease in the slope of the normal force in high angles of attack is associated with flow separation and stall. Therefore, a typical superior lifting device should have a straight normal force coefficient curve as illustrated in Figure 4.25. If the slope values of a design have high variations from the mean value, that means there are fluctuations in the slope values in certain angles of attack. This behavior is illustrated in Figure 4.26 and Figure 4.27.

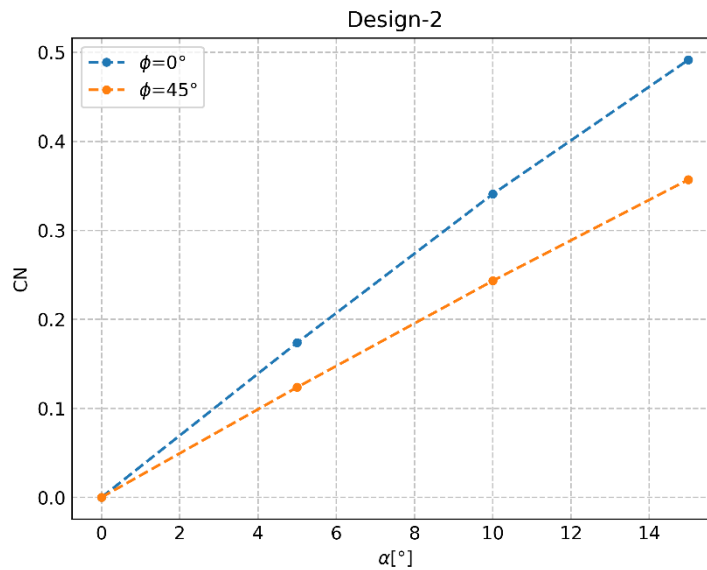

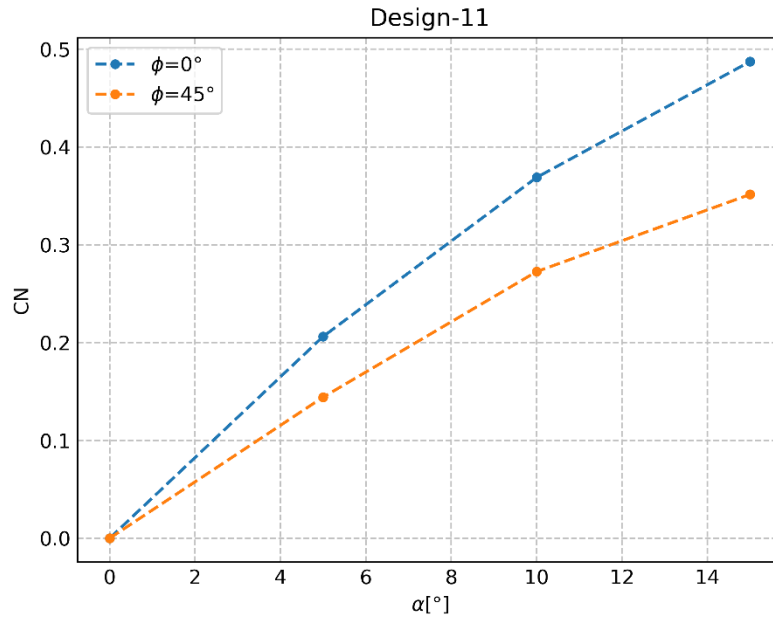Figure 4.25. Typical C_N Curve without a Sign of Stall (Design-2 / Baseline)

Figure 4.26. Performance Loss in Lifting Characteristics Example (Desing-11)
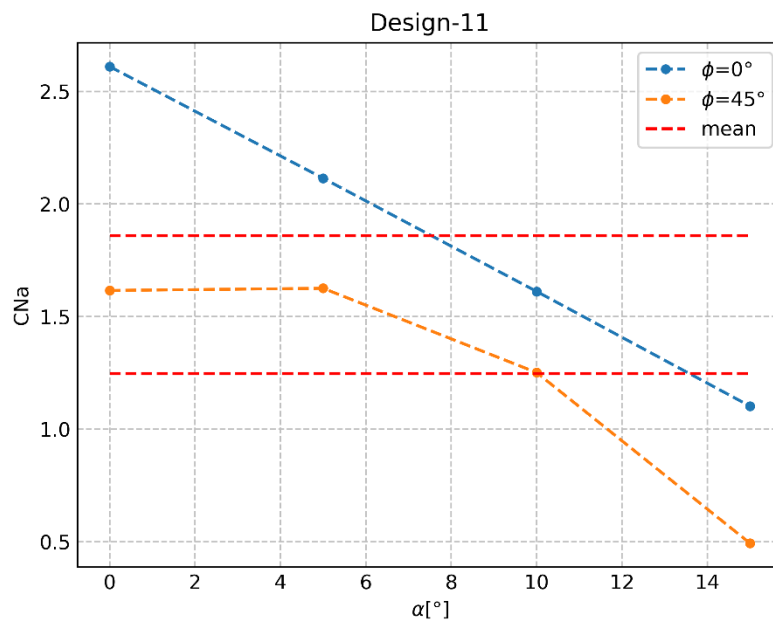
Figure 4.27. Deviations from the Mean Value of Normal Force Slope Example
(Desing-11)

In order to identify the designs having a performance loss in high angles of attack, the variation of the normal force coefficient is used. The coefficient of variation is expressed mostly as percentage value, and as a rule of thumb, beyond 30 percent considered as highly scattered data. The Coefficient of Variance (CoV) formula is given in Equation (4.3). In this formula x_i is representing C_{N_α} in this case. The coefficient of variation is plotted against the design number as it can be seen from Figure 4.28.

$$CoV = \frac{\sigma}{\mu} = \frac{\sqrt{\frac{\sum_{i=1}^{N}(x_i - \mu)^2}{N}}}{\frac{\sum_{i=1}^{N} x_i}{N}} \quad (4.3)$$

Figure 4.28. Detection of the Designs Having Performance Losses

To investigate the physical behavior of the selected results, Mach and pressure contours of corresponding designs are obtained. First the contours of the baseline design (Design-2) are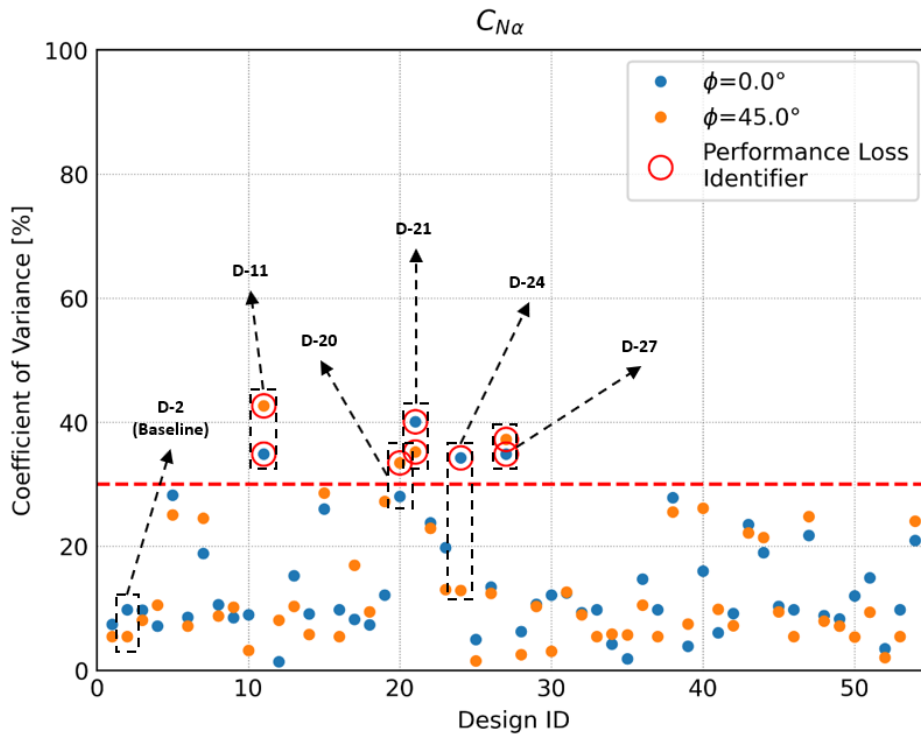 presented to observe the flow field. After that, Design-11 and Design-24 are investigated and presented here, for the sake of simplicity, since other designs have similar results with these two.

The Mach and pressure contours of the baseline design (Design-2) are presented in Figure 4.29 and Figure 4.30, respectively. The single plate regime, where all grid fin cells having similar flow pattern, is observed in the three angles of attack, namely, 0, 5, and 10 degrees. At 15° angle of attack, a separated flow is observed. In the baseline design the chord-gap ratio is 0.75, hence the gap is big enough and the expansion waves emanating from the leading edges does not hit the bottom surface of the adjacent upper cell surface, hence, the periodic plate regime is not observed here. It is an important output since the chord-gap ratio can be tailored to delay unwanted flow behaviors in certain flow conditions.
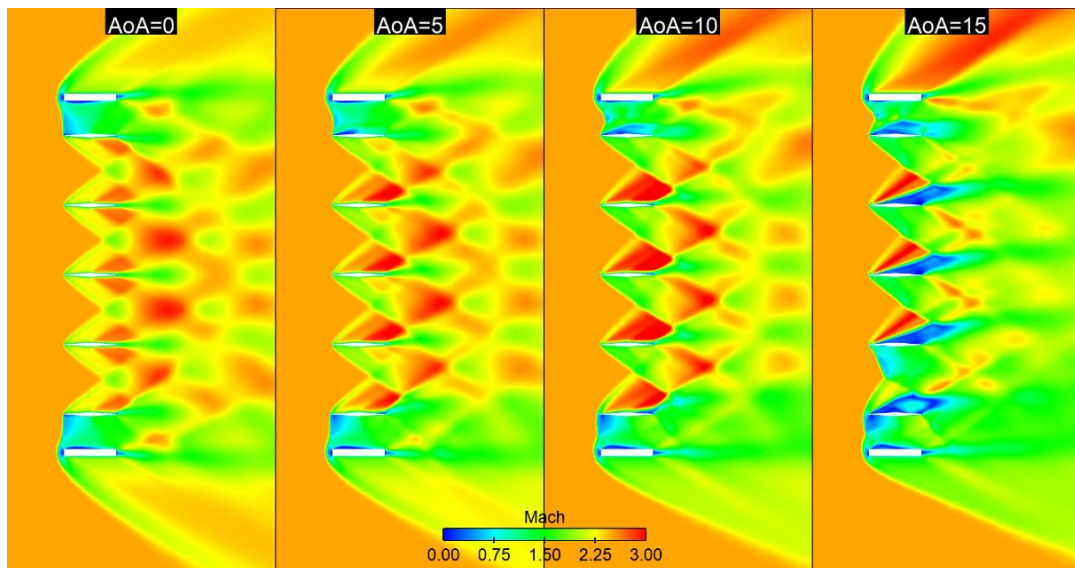
Figure 4.29. Mach Contours of Design-2 (Baseline) at 0° Roll Angle
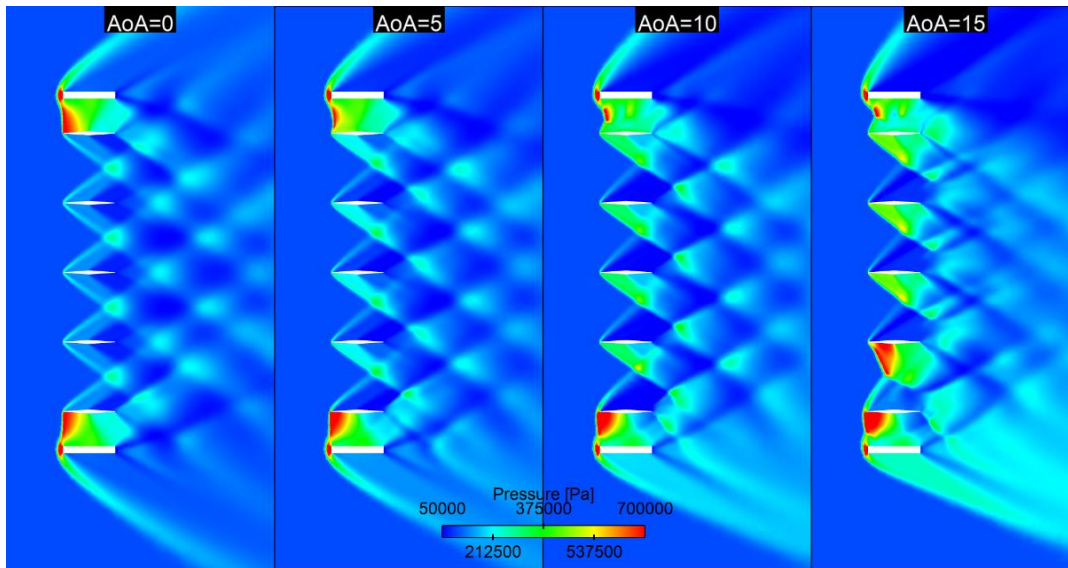
Figure 4.30. Pressure Contours of Design-2 (Baseline) at 0° Roll Angle

The common features of these inferior designs are tabulated in Table 4.3 and the corresponding geometries are illustrated in Figure 4.31. It is observed that, these designs have the same chord-gap ratio. It can be inferred that high chord-gap ratio promote separation in high angles of attack and degrade the normal force characteristics of the grid fin.

Table 4.3 Common Features of Inferior Designs

Design ID	g	c/g	s/g	w/g	t_w / g	t_f / t_w
11	30	**1.25**	2	5	0.04	2.5
20	20	**1.25**	5	8	0.04	4
21	20	**1.25**	5	8	0.04	1
24	30	**1.25**	5	5	0.01	2.5
27	30	**1.25**	8	5	0.04	2.5
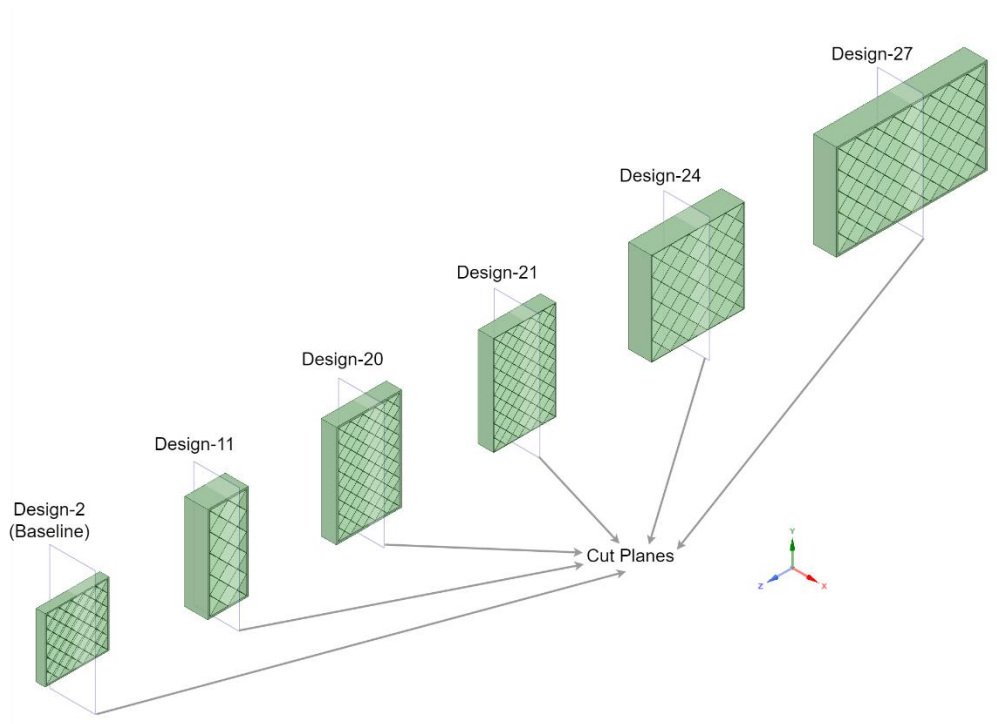
Figure 4.31. Geometries of Inferior Designs

The Mach and pressure contours of the Design-11 are presented in Figure 4.32 and Figure 4.33, respectively. As in the baseline design, the single plate regime is observed at small angles of attack, such as 0° and 5°. However, periodic plate regime behavior is observed at 10° angle of attack and the flow became prone to separation. Further increase in the angle of attack, a separated flow is observed at 15° angle of attack. The change of behavior in the flow causes the performance loss in this design and similarly others, namely, Design-21 and Design-27.

Figure 4.32. Mach Contours of Design-11 at 0° Roll Angle
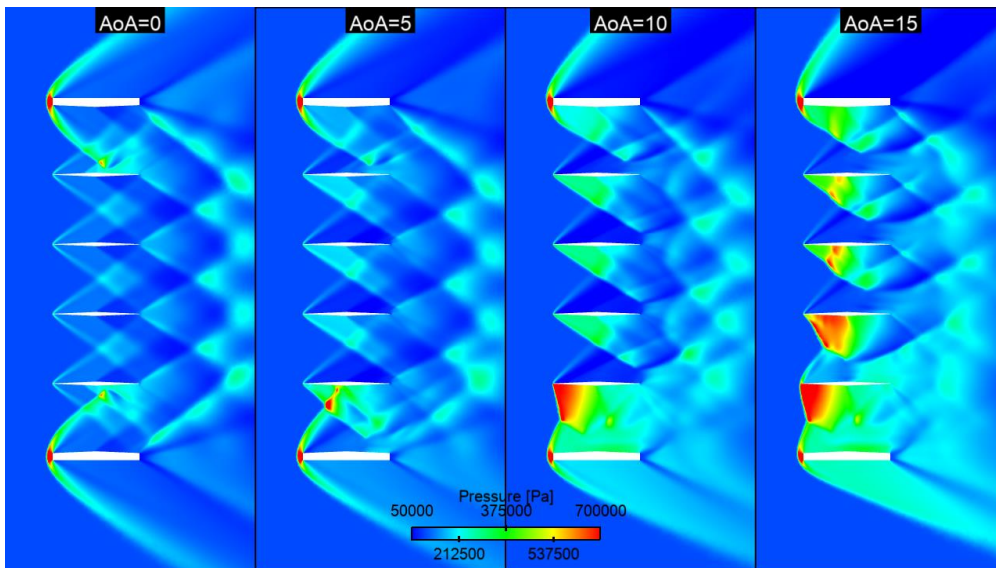
Figure 4.33. Pressure Contours of Design-11 at 0° Roll Angle

For Design-24 the Mach and pressure contours for zero roll angle flow condition are presented in Figure 4.34 and Figure 4.35, respectively. An interesting behavior is observed in Design-24. Similar flow behavior with Design-11 is detected in this design as well. However, when the 45-degree roll angle case examined, the performance degrading behavior is vanished. The corresponding Mach and pressure contours of this case is presented in Figure 4.36 and Figure 4.37, respectively.
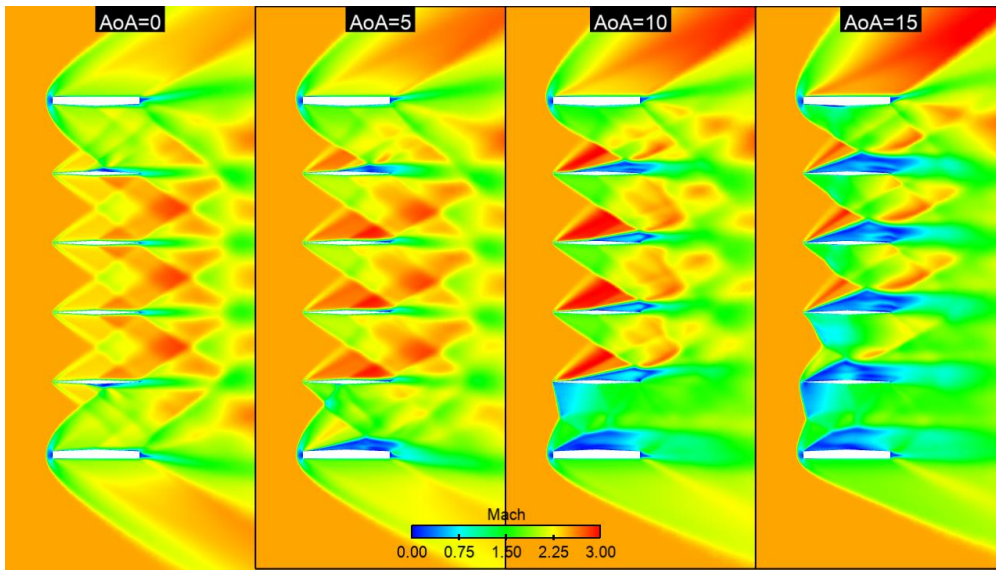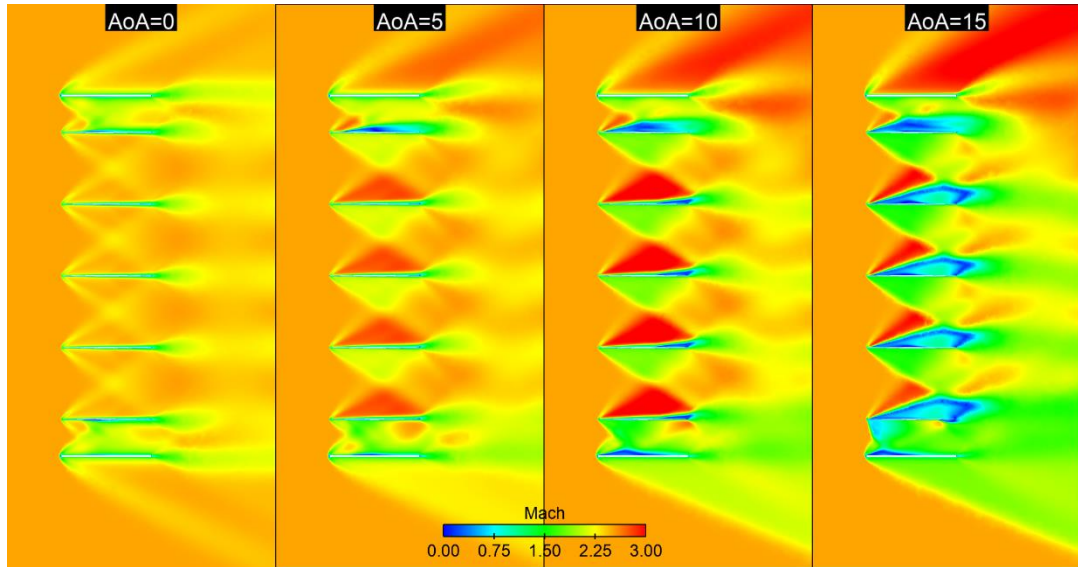

Figure 4.34. Mach Contours of Design-24 at 0° Roll Angle
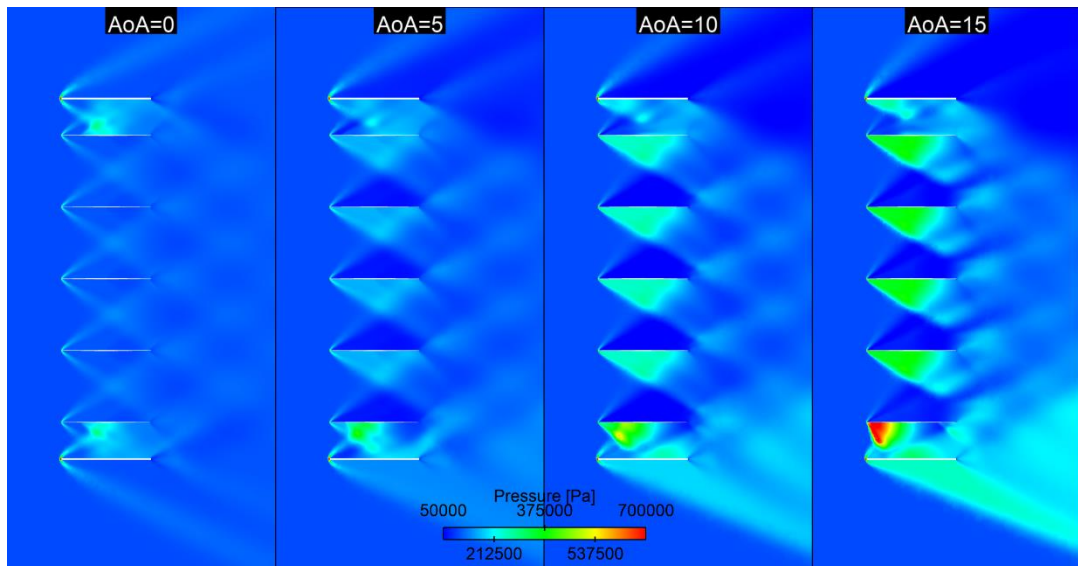
Figure 4.35. Pressure Contours of Design-24 at 0° Roll Angle
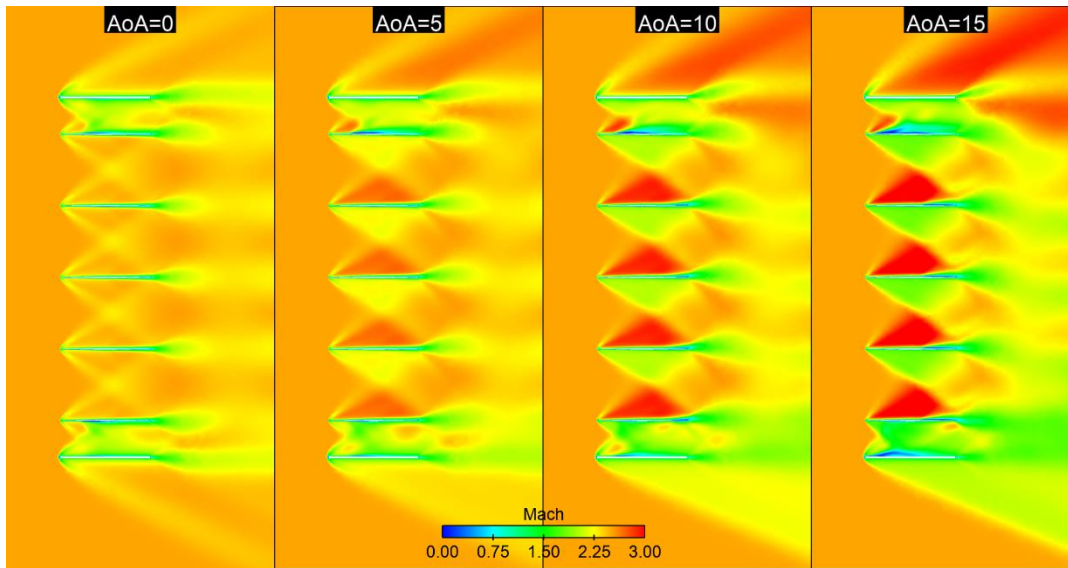
Figure 4.36. Mach Contours of Design-24 at 45° Roll Angle
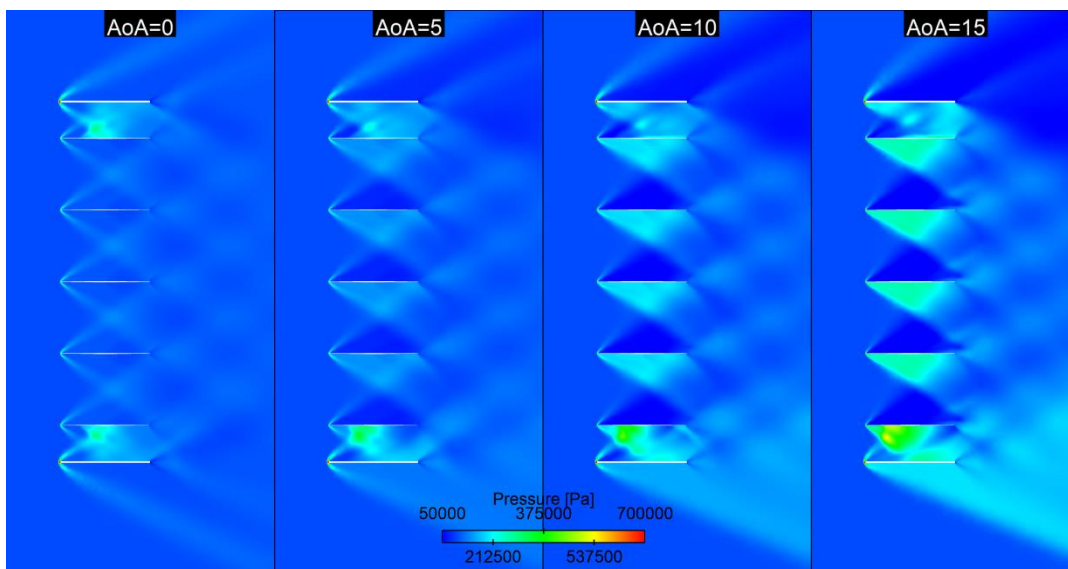
Figure 4.37 Pressure Contours of Design-24 at 45° Roll Angle

In order to investigate the difference in the flow field when the roll angle is changed, at 15° angle of attack the Mach and pressure contours are presented in Figure 4.38 and Figure 4.39, respectively. These contours are obtained from the cut-plane placed in the mid-chord location and extended in the span-wise and width-wise direction. Mach and pressure contours show that the incoming flow in zero-roll angle case, expansion waves created in the upper surfaces of web structures. In the corner points

where webs are crossed, the expansions are interact with each other and they create a shock structure in the interaction region. Since the flow angle is changed when 45° roll angle is applied, the opposing web plates create strong expansion waves, however, parallel web plates create weak expansion waves. Therefore, the weak interactions does not create shock structures and does not promote separated flow.
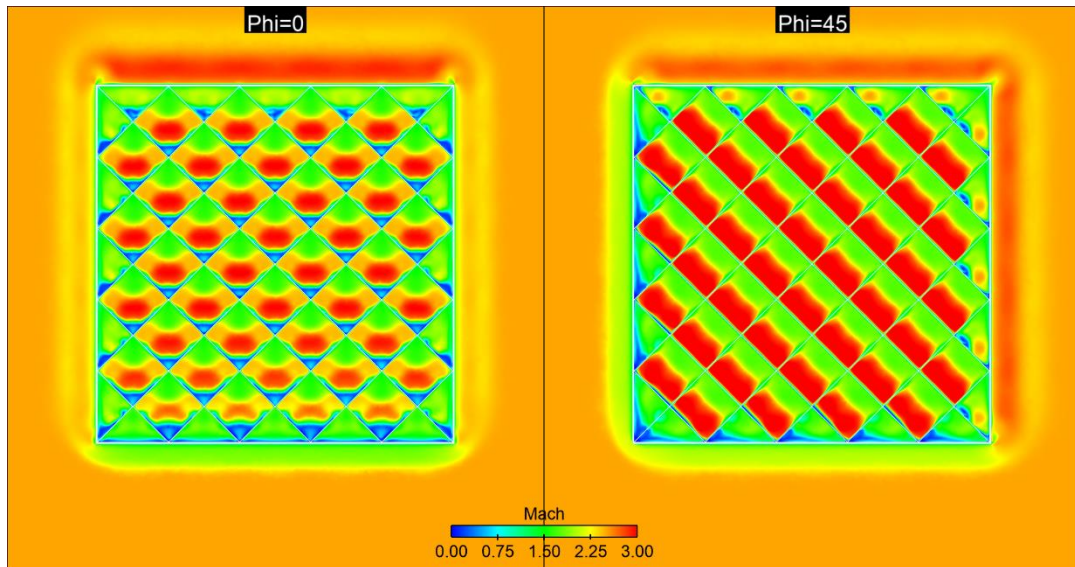
Figure 4.38. Mach Contours of Design-24 at 15° Angle of Attack
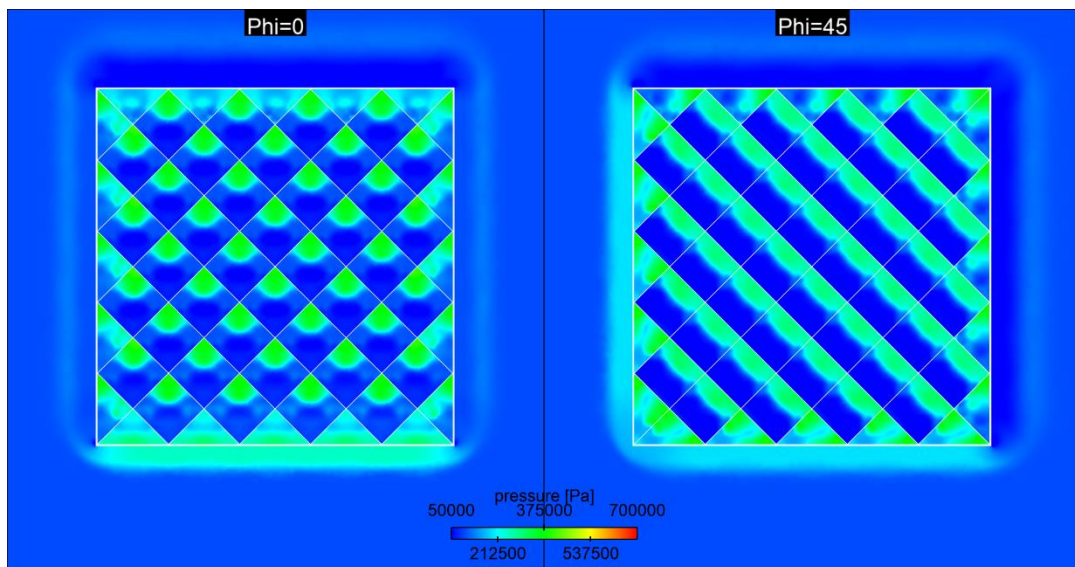
Figure 4.39. Pressure Contours of Design-24 at 15° Angle of Attack

The flow field investigations presented in this section shows that high chord-gap ratio can lead to degradation in the performance. Also, it should be noted that the CoV approach is valid for detecting the performance loss in terms of normal force characteristics in a design set. Moreover, the roll angle or the orientation of grid fins on a missile are important for the effectiveness of grid fin.

CHAPTER 5

CONCLUSION AND FUTURE WORK

In this thesis, a grid fin parametric design study is performed with the design methodology including DOE and CFD. Literature review and grid fin aerodynamic concepts are explained in the first part of the study to constitute background information on grid fins.

The grid fin design problem is handled with DOE methods to reduce the computationally expensive and time consuming CFD simulations. The design methodology utilized with RSM and surrogate models for each aerodynamic coefficient is constructed. Simulations of the design points are required to be done with high fidelity viscous CFD analyses for the complex flow field around the complex grid fin geometry. The methodology behind the parameterization of the grid fin geometry, and DOE and CFD analyses is explained in the second part of study.

For the CFD simulations of grid fins, a validation study is carried out together with mesh indpendence and turbulence model comparisons for the MICOM grid fin test case. After this validation study, a grid fin meshing approach is determined using polyhedral mesh, state of the art meshing technique, and k-ω-SST turbulence model is selected.

Considered geometric design parameters are the chord, the span, the width, the gap between members, the web profile angle and the web leading and trailing wedge lengths, the web thickness, and the frame thickness. Also, different airfoil geometries are simulated and compared in the parameter selection process. After the parameter selection process, design parameters are chosen as the chord, the span, the width, the gap between members, the web thickness, and the frame thickness and these parameters are used while performing design study. Grid fin geometries are

investigated at Mach number of 2.5 for different angles of attack between 0° and 15° for roll angles of 0° and 45° at sea level standard atmospheric conditions.

Conclusions drawn from this thesis study are listed below:

- The CFD results from the Box-Behnken DOE study are investigated and parameter screening is performed using JMP commercial software. It is shown that, the web and frame thickness related parameters have small effect on normal force and bending moment coefficients within the design space explored in this thesis. The parameter importance is also assessed for each aerodynamic coefficient as well. This is a procedure that can be applied for various design problems as well.

- Using the same CFD results, response surfaces for each aerodynamic coefficient is produced using the HEEDS commercial software with Radial Basis Function Cubic approximation. For the validation of these surrogates, validation using non-included CFD results and leave-one-out cross-validation studies are carried out. The RSM models created using Box-Behnken DOE method can predict aerodynamic coefficients of grid fin effectively in this flow regime.

- The flow field investigations are also performed for CFD results of the Box-Behnken designs to detect the anomalies in normal force coefficient curve indicating performance loss of grid fin. The common feature of these inferior designs is observed as the chord-gap ratio. According to Mach and pressure contours of these designs, high chord-gap ratio can lead to separation and therefore performance losses. Moreover, due to shock and expansion structure in the grid fin, the flow condition gain importance. Even at the same Mach number, the angle of attack and the roll angle can easily change the behavior of grid fin.

These conclusions bring up some future studies listed below:

- Grid fins can be modeled using RSM models, hence optimization and validation studies can be carried out using these surrogates.

- These RSM models and results of this thesis may be a source for prediction methods in the selected flow regime.

- The current study can be extended to other flow regimes, e.g., different Mach numbers and different angle of attacks, therefore design space can be extended according to the needs of flight envelope using the same design methodology as described in this study.

- Other grid fin shape parameters such as local sweep angle , global sweep angle, curvature, frame shaping can be implemented into the parametric model and an extended screening study can be performed.

- Studies related to interference between grid fin and other aerodynamic surfaces and protuberences attached to missile body can be performed.

REFERENCES

[1] Fleeman, E. L. (2006). Aerodynamic Considerations in Tactical Missile Design. In *Tactical Missile Design* (Ser. AIAA Education Series, pp. 37–38). essay, American Institute of Aeronautics and Astronautics.

[2] Tripathi, M., Sucheendran, M. M., & Misra, A. (2020). Experimental analysis of cell pattern on grid fin aerodynamics in subsonic flow. *Proceedings of the Institution of Mechanical Engineers, Part G: Journal of Aerospace Engineering*, *234*(3), 537–562. https://doi.org/10.1177/0954410019872349

[3] Wikimedia Foundation. (2021, September 26). *GBU-43/B moab*. Wikipedia. Retrieved December 9, 2021, from https://en.wikipedia.org/wiki/GBU-43/B_MOAB.

[4] Wikimedia Foundation. (2021, November 28). *R-77*. Wikipedia. Retrieved December 9, 2021, from https://en.wikipedia.org/wiki/R-77.

[5] 27, C. H. — J., & Henry, C. (2017, June 28). *SpaceX's final Falcon 9 design coming this year, two Falcon Heavy launches next year*. SpaceNews. Retrieved December 9, 2021, from https://spacenews.com/spacexs-final-falcon-9-design-coming-this-year-two-falcon-heavy-launches-next-year/.

[6] Theerthamalai, P., & Nagarathinam, M. (2006). Aerodynamic Analysis of Grid-Fin Configurations at Supersonic Speeds. *Journal of Spacecraft and Rockets*, *43*(4), 750–756.

[7] Sharma, N., & Kumar, R. (2019). Missile Grid Fins Analysis Using Computational Fluid Dynamics: A Systematic Review. *INCAS Bulletin*, *11*(1), 151–169. https://doi.org/10.13111/2066-8201.2019.11.1.12

[8] Washington, W., & Miller, M. (1993). Grid Fins - A New Concept for Missile Stability and Control. *31st Aerospace Sciences Meeting*. https://doi.org/10.2514/6.1993-35

[9] Fournier, E. Y. (2001). Wind Tunnel Investigation of Grid Fin and Conventional Planar Control Surfaces. *39th Aerospace Sciences Meeting and Exhibit*, *January*. https://doi.org/10.2514/6.2001-256

[10] Despirito, J., Ground, A. P., Washington, W. D., Aviation, U. S. A., Command, M., & Arsenal, R. (2002). CFD Investigation of Canard-Controlled Missile with Planar and Grid Fins in Supersonic Flow. *AIAA Atmospheric Flight Mechanics Conference, 2002*, *August*.

[11] Munawar, S. (2010). Analysis of Grid Fins as Efficient Control Surface in Comparison to Conventional Planar Fins. *27th Congress of the International Council of the Aeronautical Sciences 2010, ICAS 2010*, *3*, 1732–1737. https://doi.org/10.2514/6.2009-5845

[12] Burkhalter, J. E., & Frank, H. M. (1996). Grid fin aerodynamics for missile applications in subsonic flow. *Journal of Spacecraft and Rockets*, *33*(1), 38–44. https://doi.org/10.2514/3.55704

[13] Burkhalter, J. E., & Frank, H. M. (1995). Non-linear aerodynamic analysis of grid fin configurations. *13th Applied Aerodynamics Conference*, *32*(3), 1069–1083. https://doi.org/10.2514/6.1995-1894

[14] Burkhalter, J. E. (1996). Grid fins for missile applications in supersonic flow. *34th Aerospace Sciences Meeting and Exhibit*, *January*. https://doi.org/10.2514/6.1996-194

[15] Evvard, J. C. (1950). *Use of Source Distributions for Evaluating theoretical Aerodynamics of Thin Finite Wings at Supersonic Speeds, NACA-TR-951*.

[16] Theerthamalai, P., Manisekaran, S., & Nagarathinam, M. (2005). A prediction method for aerodynamic characterization of grid-fin configurations at

supersonic speeds. *Collection of Technical Papers - AIAA Applied Aerodynamics Conference*, *2*(June), 791–798. https://doi.org/10.2514/6.2005-4967

[17]   Theerthamalai, P. (2007). Aerodynamic characterization of grid fins at subsonic speeds. *Journal of Aircraft*, *44*(2), 694–698. https://doi.org/10.2514/1.27653

[18]   Ledlow, T. W., Burkhalter, J. E., & Hartfield, R. J. (2015). Integration of grid fins for the optimal design of missile systems. *AIAA Atmospheric Flight Mechanics Conference, 2015*, *January*, 1–31. https://doi.org/10.2514/6.2015-1017

[19]   Dikbaş, E. (2015). *Design of a Grid Fin Aerodynamic Control Device for Transonic Flight Regime* (Issue June).

[20]   Dikbaş, E., Baran, Ö. U., & Sert, C. (2018). Simplified numerical approach for the prediction of aerodynamic forces on grid fins. *Journal of Spacecraft and Rockets*, *55*(4), 887–898. https://doi.org/10.2514/1.A34062

[21]   Sun, Y., & Khalid, M. (1998). AIAA 98-3571 34th AIAA / ASME / SAE / ASEE Joint Propulsion Conference & Exhibit. *A CFD Investigation of Grid Fin Missiles*.

[22]   DeSpirito, J., Edge, H. L., Weinacht, P., Sahu, J., & Dinavhi, S. P. G. (2000). CFD Analysis of Grid Gins for Maneuvering Missiles. *38th Aerospace Sciences Meeting and Exhibit*, *January*. https://doi.org/10.2514/6.2000-391

[23]   DeSpirito, J., & Sahu, J. (2001). Viscous CFD calculations of grid fin missile aerodynamics in the supersonic flow regime. *39th Aerospace Sciences Meeting and Exhibit*. https://doi.org/10.2514/6.2001-257

[24]   Mingsheng, M., Youqi, D., Ming, Z., & Naichun, Z. (2005). Navier-Stokes Computations for a Grid Fin Missile. *23rd AIAA Applied Aerodynamics Conference*, *2*(June), 860–864. https://doi.org/10.2514/6.2005-4973

[25]   Deng, Y. Q., Ma, M. S., Zheng, M., & Zhou, N. C. (2006). Navier-Stokes Computation of Grid Fin Missile Using Hybrid Structured-Unstructured Grids. *Chinese Journal of Aeronautics*, *19*(4), 304–308. https://doi.org/10.1016/S1000-9361(11)60332-4

[26]   Reynier, P., Longo, J. M., & Schülein, E. (2006). Simulation of Missiles with Grid Fins Using an Actuator Disk. *Journal of Spacecraft and Rockets*, *43*(1), 84–91. https://doi.org/10.2514/1.7939

[27]   Hughson, M. C., Blades, E. L., Luke, E. A., & Abate, G. L. (2007). Analysis of Lattice Grid Tailfin Missiles in High-Speed Flow. *25th AIAA Applied Aerodynamics Conference*, *1*(June), 572–586. https://doi.org/10.2514/6.2007-3932

[28]   Ravindra, K., Shende, N. V., & Balakrishnan, N. (2013). CFD Simulation of the Grid Fin Flows. *31st AIAA Applied Aerodynamics Conference*, *June*, 24–27. https://doi.org/10.2514/6.2013-3023

[29]   Washington, W. D., Booth, P., & Miller, M. (1993). Curvature and Leading Edge Sweep Back Effects on Grid Fin Aerodynamic Characteristics. *AIAA Journal*, 659–667. https://doi.org/10.2514/6.1993-3480

[30]   Miller, M., & Washington, W. D. (1994). An Experimental Investigation of Grid Gin Drag Reduction Techniques. *AIAA 12th Applied Aerodynamics Conference, 1994*, 800–808. https://doi.org/10.2514/6.1994-1914

[31]   Chen, S., Khalid, M., Xu, H., & Lesage, F. (2000). An Investigation of the Grid Fins as Control Surface Devices for Missiles. *Aeronautical Journal*, *104*(1034), 183–190.

[32]   Hiroshima, F., & Tatsumi, K. (2004). Grid Pattern Effects on Aerodynamic Characteristics of Grid Fins. *24th International Congress of the Aeronautical Sciences, Yokohama, Japan, 29 August - 3 September 2004*, 1–8.

[33]   Wu, P., Ma, Y. G., & Chen, C. (2005). Research Analysis of Aerodynamic Numerical Simulation of Grid Fin. *Journal of Zhejiang University: Science*, *6 A*(7), 741–746. https://doi.org/10.1631/jzus.2005.A0741

[34]   Schülein, E.; Guyot, D. (2006) Novel High-Performance Grid Fins for Missile Control at High Speeds: Preliminary Numerical and Experimental Investigations. In Innovative Missile Systems (pp. 35-1 – 35-28). *Meeting Proceedings RTO-MP-AVT-135*, Paper 35. Neuilly-sur-Seine, France: RTO

[35]   Zeng, Y., Cai, J., Debiasi, M., & Chng, T. L. (2009). Numerical Study on Drag Reduction for Grid-Fin Configurations. *47th AIAA Aerospace Sciences Meeting Including the New Horizons Forum and Aerospace Exposition*, *January*, 1–10. https://doi.org/10.2514/6.2009-1105

[36]   Debiasi, M., Yan, Z., & Loon, C. T. (2010). Swept-Back Grid Fins for Transonic Drag Reduction. *28th AIAA Applied Aerodynamics Conference*, *1*(July), 1–17. https://doi.org/10.2514/6.2010-4244

[37]   Debiasi, M. (2012). Measurements of the Forces and Moments Generated by Swept-Back Grid Fins. *30th AIAA Applied Aerodynamics Conference 2012*, *June*, 1079–1089. https://doi.org/10.2514/6.2012-2909

[38]   Debiasi, M., & Zeng, Y. (2016). Forces and Moments Generated by Swept-Back Grid Fins with Sharp Leading Edges. *Journal of Aircraft*, *53*(6), 1962–1966. https://doi.org/10.2514/1.C033504

[39]   Faza, G. A., Fadillah, H., Silitonga, F. Y., & Moelyadi, M. A. (2018). Study of Swept Angle Effects on Grid Fins Aerodynamics Performance. *Journal of Physics: Conference Series*, *1005*(1). https://doi.org/10.1088/1742-6596/1005/1/012013

[40]   Yang, X., & Zhang, W. (2013). A Faster Optimization Method Based on Support Vector Regression for Aerodynamic Problems. *Advances in Space Research*, *52*(6), 1008–1017. https://doi.org/10.1016/j.asr.2013.05.030

[41] Despeyroux, A., Hickey, J. P., Desaulnier, R., Luciano, R., Piotrowski, M., & Hamel, N. (2015). Numerical Analysis of Static and Dynamic Performances of Grid Fin Controlled Missiles. *Journal of Spacecraft and Rockets*, *52*(4), 1236–1252. https://doi.org/10.2514/1.A33189

[42] Peng, K., Hu, F., Wang, D., Okolo, P. N., Xiang, M., Bennett, G. J., & Zhang, W. (2018). Grid Fins Shape Design of a Launch Vehicle Based on Sequential Approximation Optimization. *Advances in Space Research*, *62*(7), 1863–1878. https://doi.org/10.1016/j.asr.2018.06.001

[43] Anderson, D., Tannehill, J. C., & Pletcher, R. H. (2016). *Computational fluid mechanics and heat transfer.* Taylor & Francis.

[44] Ansys Inc., *ANSYS Fluent Theory Guide*. 2013.

[45] Rao, V. S., Viti, V., & Abanto, J. (2020). CFD Simulations of Super/Hypersonic Missiles: Validation, Sensitivity Analysis, and Improved Design. *AIAA Scitech 2020 Forum*, *1 PartF*(January), 1–22. https://doi.org/10.2514/6.2020-2123

[46] Celik, I. B., Ghia, U., Roache, P. J., Freitas, C. J., Coleman, H., & Raad, P. E. (2008). Procedure for estimation and reporting of uncertainty due to discretization in CFD applications. *Journal of Fluids Engineering, Transactions of the ASME*, *130*(7), 0780011–0780014. https://doi.org/10.1115/1.2960953

[47] N. V. Queipo, R. T. Haftka, W. Shyy, T. Goel, R. Vaidyanathan, and P. Kevin Tucker, "Surrogate-based analysis and optimization," *Prog. Aerosp. Sci.*, vol. 41, no. 1, pp. 1–28, 2005, doi: 10.1016/j.paerosci.2005.02.001.

[48] El-Gohary, M., & Ahmed, M. (2013). Investigating the Design Parameters of a Diamond-Shaped Supersonic Airfoil. *International Conference on Aerospace Sciences and Aviation Technology*, *15*(AEROSPACE SCIENCES), 1–18. https://doi.org/10.21608/asat.2013.22106

[49]   Aerospaceweb.org | ask   us   -   missile   grid   fins. http://www.aerospaceweb.org/question/weapons/q0261.shtml. (Visited on 22-March-2015).

[50]   Wikimedia Foundation. (2021, December 7). *Shock diamond*. Wikipedia. Retrieved January 13, 2022, from https://en.wikipedia.org/wiki/Shock_diamond

[51]   SAS Institute Inc., *JMP 14 Design of Experiments Guide*. Cary, NC, 2018.

[52]   Goel, T., & Stander, N. (2009). Comparing Three Error Criteria for Selecting Radial Basis Function Network Topology. *Computer Methods in Applied Mechanics and Engineering*, *198*(27–29), 2137–2150. https://doi.org/10.1016/j.cma.2009.02.016

[53]   Dinçer, E., & Sezer Uzol, N. (2021). Grid Fin Aerodynamic Analysis and Parametric Design Study in. *11th Ankara International Aerospace Conference*, *September*, 1–14.

[54]   John D. Anderson, J. (2010). *Fundamentals of Aerodynamics* (Third Edit). Tata McGraw-Hill Education